Ice-Induced Vibrations of Vertical Structures

Vom Promotionsausschuss der
Technischen Universität Hamburg

zur Erlangung des akademischen Grades

Doktor-Ingenieurin (Dr.-Ing.)

genehmigte Dissertation

von
Gesa Ziemer

aus
Hamburg

2021

1. Gutachter: Prof. Dr. rer. nat. habil. Norbert Hoffmann

2. Gutachter: Prof. D. Sc. (Tech.) Sören Ehlers

Tag der mündlichen Prüfung: 30.11.2021

DOI: https://doi.org/10.15480/882.4018

ORCID: https://orcid.org/0000-0001-6617-3658

Kurzfassung

Eis-erregte Schwingungen stellen ein erhebliches Risiko für fest gegründete, vertikale Offshore Strukturen in Bereichen mit Meereis-Vorkommen dar. Obwohl nach den ersten Beobachtungen solcher Schwingungen diesem Thema einige Jahrzehnte lang umfangreiche Forschung gewidmet wurde, konnte die Frage nach dem zugrunde liegenden Mechanismus bisher noch nicht abschließend geklärt werden. Es existieren mehrere theoretische Modelle, die zum Teil gute Übereinstimmung mit Beobachtungen zeigen. Dennoch konnten ihre physikalischen Grundlagen bisher nicht validiert werden.
Aktuelle Theorien besagen, dass die Entwicklung der Kontaktfläche zwischen Eis und Struktur eine entscheidende Rolle in der Entstehung Eis-erregter Schwingungen spielt. Bisher konnte die Kontaktfläche jedoch nicht mit ausreichender Genauigkeit gemessen werden. Daher wurden für die vorliegende Arbeit Modellversuche mit einem flexiblen Aufbau durchgeführt, bei denen für unterschiedliche Struktur- und Eisparameter die lokalen Drücke sowie die Kontaktfläche zwischen Eis und Struktur ermittelt werden konnten. Eine Analyse der erhobenen Daten zeigt einen klaren Zusammenhang zwischen der Entwicklung von lokalem Versagen sowie der Kontaktfläche und der Relativgeschwindigkeit zwischen Eis und Struktur. Mit den gewonnenen Erkenntnissen wurden die existierenden Theorien diskutiert. Basierend darauf wurde eine Vorhersagemethode abgeleitet, mit deren Hilfe der kritische Geschwindigkeitsbereich für Eis-erregte Schwingungen direkt berechnet werden kann.
Abschließend wurde die Skalierbarkeit von Eis-erregten Schwingungen anhand der Ergebnisse der physikalischen Versuche und der abgeleiteten theoretischen Zusammenhänge diskutiert. Da das verwendete Modelleis erhebliche Einschränkungen in der Darstellung von Druckversagen an vertikalen Strukturen zeigte, umfasst diese Arbeit auch erste Schritte zur Entwicklung einer neuen Herstellungsweise für Modelleis, das Druckversagen realistischer im physikalischen Modellversuch abbilden kann.

Abstract

Ice-induced vibrations are a serious risk for fixed vertical offshore structures located in areas with sea ice occurrence. Despite extensive research in the decades following the first full scale observation, the underlying mechanism is still not entirely understood to date. Theoretical models exist which show good consistency with observations; however, their physical validity could not be conclusively proven yet.
Recent theories consider the contact area between structure and ice to play a decisive role in the occurrence of ice-induced frequency lock-in vibrations. However, it has not been possible so far to measure the actual contact area during such vibrations at sufficient spatial resolution. For this thesis, model ice tests with a compliant physical test setup have been conducted which allowed measurement of local loads and contact area while varying several structural and ice parameters. Analysis of the measurements gives insight into the dependence of local failure and contact area development on relative velocity between ice and structure. With this novel insight, existing theories are evaluated and discussed. A prediction method is formulated to calculate critical velocities for the occurrence of frequency lock-in vibrations.
Finally, the experimental data base is used to discuss the scalability of dynamic ice-structure interaction, and the limitations of saline columnar model ice with respect to representation of crushing failure against vertical structures. An alternative ice preparation procedure is suggested and tested, which constitutes a sound basis for further development.

Acknowledgements

First of all, I would like to thank my supervisor Prof. Norbert Hoffmann for his support and encouragement. Thanks to Prof. Sören Ehlers for supporting me as second examiner, and to Prof. Huber for chairing the committee.

I would not have started this project without the motivation I received from Peter Jochmann, former Head of Arctic Technology Department at HSVA, who supported me with his knowledge, fruitful discussions, and trust in my skills.
Thanks also to all other colleagues from Arctic Technology section at HSVA who shared their knowledge and were always open for discussions. Sincere gratitude to the whole ice tank crew for professional execution of countless tests with challenging setups - you did a great job! Thanks to HSVA's CAD Designers Marc Walkenhorst and especially Michael Neumeier for realization of the setup design. Thanks to Andy Witt for rare but always enjoyable Fridays at the office.

The model test execution would not have been possible without the financial support from SAMCoT and the IVOS project. Special thanks to all industry and academia partners: NTNU, TU Delft, Total E&P Norge AS, Shell Technology Norway AS, Multiconsult AS, DNV GL, Engie AS, and Kvaerner AS. Especially Hayo Hendrikse, Torodd Nord, Robert Bridges and Kaj Riska have been a real support with interesting discussions and productive suggestions during the test campaigns.
The data analysis has been partly financed by the project CoPSIS funded by the Federal Ministry for Economic Affairs and Energy (BMWi, Project O3SX408A).

Several bachelor and master students have been helping out with the model tests. Thanks in particular to Jonas Bechthold, Clemens Deutsch, Cody Owen and Franziska Müller for their helpful work, and for sharing my enthusiasm about structures that start shaking in the basin. Thanks to my colleagues Philip Hinse and Timo Stange for professional continuation of my projects when I was on leave.

Finally, my family: Thanks to my parents Maike and Gerd Onken for their unwavering support, and for providing the basis I needed to grow up to the person I am today. My husband Tim for being my safe harbour, no matter what this life might bring. I would not have managed to complete this thesis without his unlimited support.
I am blessed with two adorable sons who make my life so much brighter. Seeing the world through their eyes puts things into the right perspective. Tapio and Miko - words cannot express how much I love you, and how grateful I am for the love you return.

Contents

List of Figures

List of Tables

List of Symbols

Latin Notation

a	exponent for aspect ratio
A	contact area
c	damping coefficient
CQ	column quantity
CW	column width
D	cylinder diameter
D/h	aspect ratio
E	Young's modulus
E_q	Qualitative elastic modulus
f_{load}	dominant frequency of ice load
f_n	natural frequency
F	general ice load
F_{CC}	mean crushing load
F_{DAC}	global ice load in ice drift direction measured with DAC system
F_{ice}	ice load acting in ice drift direction
F_{inertia}	inertia forces
F_s	sampling rate
F_{TAC}	global ice load in ice drift direction measured with TAC system
F_{visc}	viscous forces
F_{6comp}	load measured on 6-component scale
g	acceleration of gravity
h, h_{ice}	ice thickness
k	stiffness
L	reference length
l	event length
m	oscillating mass
N	number of samples or events
p	local ice pressure
p_{act}	actual global pressure
p_{max}	maximum local pressure
p_{nom}	nominal pressure
RQ	row quantity
RW	row width
R^2	coefficient of determination
t	time
T	period of oscillation
u	structure displacement
u_{CC}	mean deflection resulting from static mean crushing load
u_{stat}	deflection corresponding to a static load
v_{ice}	ice drift speed
v_{osc}	oscillation velocity
v_{ref}	reference velocity
v_{I}	lower transitional velocity
v_{II}	upper transitional velocity
W	projected width
x, y, z	axes of tank coordinate system

Greek Notation

α	factor for size effect and confinement
β	ratio of oscillation amplitude and ice drift speed
γ	parameter for steadiness of response during FLI
η	load magnification factor
λ	general scale factor
μ	friction coefficient
ξ	damping ratio as fraction of critical damping
ρ	ice density
σ_c	compressive strength
σ_f	flexural strength
σ_{SSSE}	ice peak stress during FLI
τ	delay for phase space reconstruction
χ	α-ratio
ω	oscillation frequency

List of Abbreviations

CC	continuous crushing
Ch	Cauchy number
DAC	digital-analogue-converter, referring to conventional measuring system
DAF	dynamic amplification factor
DMF	dynamic magnification factor
FLI	frequency lock-in
FIR	finite impulse response (filter)
Fr	Froude number
HPZ	high pressure zone
HSVA	Hamburgische Schiffbau-Versuchsanstalt (Hamburg ship model basin)
IC	intermittent crushing
ICMI	improved crushing model ice
ITTC	International Towing Tank Conference
ISO	International Standardization Organisation
IVOS	Research Project Ice-induced vibrations of Offshore Structures
LIMB	large ice model basin at HSVA
LOLEIF	Research project Validation of Low level Ice Forces on Offshore Structures
LVDT	linear variable differential transformer
MI	standard HSVA model ice
NSG	Norströmsgrund lighthouse
PSD	power spectral density
SCP	still cooling phase
SDOF	single degree of freedom
STRICE	Research project Structures in Ice
TAC	tactile, referring to tactile measurement system
WCP	wave cooling phase

1. Introduction

Ice-induced vibrations, particularly those exciting a structure in resonance, are a major threat to fixed offshore structures exposed to drifting sea ice. Safe, yet cost-efficient designs are required to utilize offshore areas, for example to expand use of renewable energy resources by building offshore wind farms in areas with potential ice occurrence. However, the design process is to date impeded by uncertainties about the occurrence and magnitude of ice-induced resonant vibrations, called frequency lock-in (FLI). FLI primarily occurs on vertical structures, because it is a special type of crushing failure. The current ISO guideline for design of Arctic offshore structures (ISO 19906:2019, [30]) states:

Frequency lock-in can cause resonant loading and can contribute significantly to fatigue accumulation in structures. This dynamic loading stage can cause low-cycle fatigue in steel and can also cause liquefaction in the soil foundation. Vibrations can also affect topside structures, such as flare booms.

Despite the indisputable relevance for offshore structure design, the underlying physical mechanism of lock-in has not been fully deciphered. Current research indicates that the key to the lock-in mechanism lies in the local contact area and contact pressure development [23, 56, 60, 63]. This hypothesis demands for full scale or laboratory test campaigns utilizing local pressure mapping techniques. However, full scale data is rare, and data from laboratory tests has to be treated cautiously when observations from the basin shall be transferred to full scale because of considerable uncertainties: Is the process in model ice the same as in nature? A fundamental issue with studying dynamic ice-structure interaction in the laboratory is the nature of common model ice and the state-of-the-art scaling approaches for ice model tests. While ice model tests are validated well for certain test types dominated by flexural failure, their applicability to tests with crushing failure has often been questioned. For example, Palmer and Dempsey [65] claim that tests in common model ice, customarily using Froude scaling law adapted from open water tests, will not deliver correct results for the crushing regime. They argue that the procedures weakening the ice, required to maintain Froude and Cauchy similarity [88], change the ice material behaviour in unrealistic, non-scalable manner. Hence, it needs to be assessed whether the interaction seen in the ice model basin is the same as that occurring between a full scale bottom-fixed offshore structure and sea ice. However, laboratory tests are a valuable tool to study lock-in vibrations under well-defined conditions, and are inevitable to increase our understanding of the interaction as long as no fully validated theoretical models exist.

To fill the knowledge gap, lock-in is investigated for the study at hand in a unique model test campaign with comprehensive parameter variation, and with application of a pressure mapping technique to get insight into contact area and pressure development at model scale, and in model ice. The data has been gathered within the IVOS research project [103].

In this thesis, the state of the art knowledge about ice actions on fixed cylindrical offshore structures is introduced with emphasis on ice-induced vibrations. Shortcomings of current theoretical models for the reliable prediction of critical velocities leading to frequency lock-in vibrations, which excite the structure in its natural frequency, are discussed, and an overview of existing full scale and model scale data is given. After concluding that additional laboratory test data is required to decipher the dynamic interaction between ice and structure, the experimental campaign carried out for the current study is presented. In this campaign, several influencing parameters are varied systematically, and the local pressure and contact area development is measured with high spatial and temporal resolution.
The experimental results are then systematically analysed in frequency and time domain. Emphasis is put on the development of pressure and size of the contact area. With the increased knowledge on global and local features, a simple mathematical model and corresponding prediction formulas for the occurrence of frequency lock-in are derived. Model identification is performed with the experimental data, and the model is validated against additional data sets.
Finally, the scalability of continuous crushing and events of ice-induced vibrations of vertical structures in an ice model basin is assessed. A scaling scheme is proposed for laboratory tests on ice-induced vibrations, and its limitations are discussed. The thesis concludes with introduction of a modified model ice type more suitable for crushing tests. Finally, conclusions and an outlook are given.

2. State of the art - Ice actions on fixed offshore structures

Ice is a quasi-brittle material, which creeps under very low stress levels, and fails in brittle crushing when stress or strain are high. Hence, its failure mechanism in compression depends on the loading rate and loading condition.
The interaction between drifting sea ice and offshore structures is manifold and can show various types of material failure and dynamic ice-structure interaction, depending on the shape of the structure at ice-structure interface, ice velocity v_{ice}, aspect ratio D/h, and ice properties such as ice thickness h and compressive as well as flexural strength (σ_c and σ_f) [89,90]. The following sections introduce types of ice failure and corresponding ice-induced vibrations with emphasis on resonant vibrations. For a comprehensive state-of-the-art overview the reader is referred to Palmer and Croasdale [64].

2.1. Ice failure modes

When ice fails against a fixed structure, two main cases are distinguished: Failure on a vertical structure (Fig. 1a), predominantly in crushing, and bending failure on a sloping structure (Fig. 1b). Additional classifications are generally defined in the ISO guideline [30] and briefly described below:

Bending
Bending means flexural failure of the ice due to a bending moment caused by vertical loads imposed on the ice sheet, typically occurring on structures with inclined side walls or due to accumulation of crushed ice below or on top of the ice sheet.

Buckling
Buckling refers to global flexural failure of the ice due to out-of-plane deformation of the ice sheet until bending capacity is reached. It occurs mainly on structures with high aspect ratio or in thin, typically rather strong ice, when the critical buckling load is smaller than the maximum in-plane load due to crushing or creep [51].

Creep
Creep occurs at very low ice speed and low aspect ratios. While the ice moves slowly towards the structure, full contact with rather uniform pressure distribution develops. The ice deforms plastically in front of the structure to mitigate the increasing load. Details for ice creep are given by Schulson and Duval [74].

Crushing
Ice failing against vertical structures in compression is called *crushing*. It primarily occurs with medium to high indentation speed and low aspect ratios. This failure mode is associated with the occurrence of severe ice-induced vibrations and is described in more detail in the following sections.

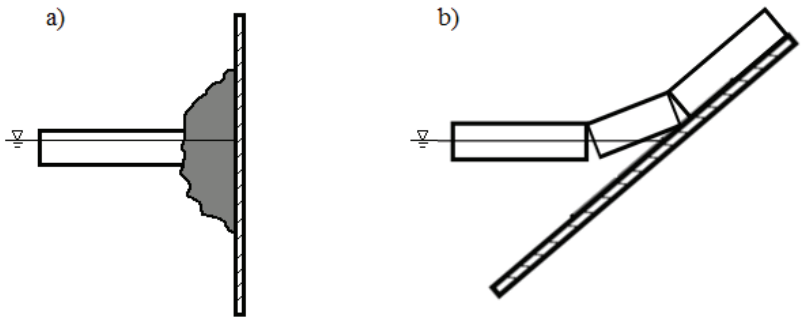

Figure 1: Illustration of crushing against vertical structures (a) and bending failure on sloping structures (b), after ISO 19906:2019 ([30], Fig. A.8-7)

2.2. Crushing regimes

The term *crushing* refers to the ice sheet failing against a structure in compression. However, the failure process can be quite different depending on the indentation velocity. Since the underlying physical processes have not been exactly known for decades, the terms and definitions have changed throughout the years, and literature is still not always consistent. In this thesis, the definition stipulated in the latest ISO code (ISO19906:2019 [30]), illustrated in Fig. 2, is followed. It distinguishes crushing in *intermittent crushing*, *frequency lock-in* and *continuous brittle crushing*.

2.2.1. Intermittent crushing

Intermittent crushing (IC) occurs on compliant structures facing ice with low indentation speed [32, 34, 44]. It is characterized by a load build-up and an unloading phase (Fig. 2a). While the structure is deflected, the ice surface smoothens due to ductile deformation and local crushing, and thereby the contact area increases and the pressure distribution becomes rather uniform. During deflection, elastic energy is stored in the structure until the local pressures reach the ice strength and local failure occurs eventually. After initial local failure, ice across the whole interaction area fails in a chain reaction, and the structure moves back. At the same time, the stored energy is converted into kinetic energy and dissipated mainly in crushing. As the ice typically fails faster than the structure swings back, contact is fully or partly lost during unloading phase, and the structure oscillates until all energy is dissipated. Typically, osciallations decay before the next load build-up starts. Ice and structure have approximately the same velocity, and the structural displacement is defined by the load magnitude and the structure's stiffness at water level. Therefore, intermittent crushing is also referred to as quasi-static interaction. Load and response time histories show the same sawtooth pattern and have identical dominant frequencies. These frequencies increase with increasing ice drift speed, and are usually lower than the structure's eigenfrequencies [81]. Due to the smoothened contact and thereby large contact area with uniform pressure distribution, high ice loads can develop. Kärnä and Muhonen [45] found peak loads

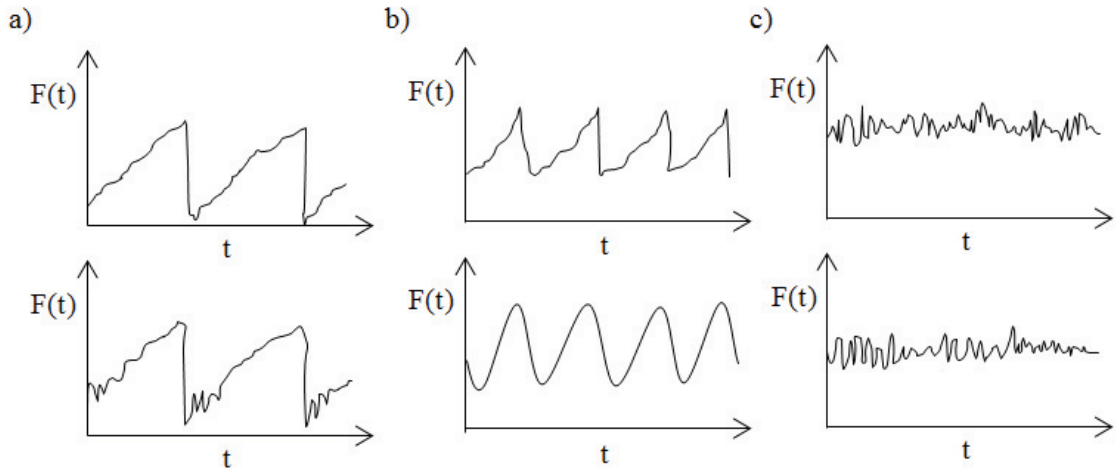

Figure 2: Illustration of crushing modes, generated after ISO 19906:2019 ([30], Figure A-8.30): Intermittent crushing (IC, a), Frequency lock-in (FLI, b), Continuous Crushing (CC, c). Therein, F denotes ice action, u structure displacement, and t time.

increasing by about factor two when failure changes from continuous crushing to intermittent crushing in laboratory tests. Jefferies and Wright [34] report on intermittent crushing occurring on the Molikpaq structure, resulting in severe ice-induced vibrations.

Full scale measurements of intermittent crushing including local pressures were performed during the JOIA experiments [72]. Määttänen et al. [56] conducted laboratory tests in model ice with a compliant cylindrical indenter equipped with a tactile sensor which measures local pressures across the ice-structure interaction zone with high resolution over ice thickness and contact width. Their records of intermittent crushing agree to the above described process of contact area growth and uniform pressure increase. However, the measurements were not detailed enough to quantify the contact area increase, maximum local pressures and size of interaction zones [24].

2.2.2. Frequency lock-in

Frequency lock-in (FLI) occurs on compliant structures with relatively low damping and low natural frequencies. ISO Standard [30] refers to eigenfrequencies below 10 Hz to be relevant for the occurrence of FLI on offshore structures. It describes an interaction case where the ice load becomes periodic in a frequency close to the structure's natural frequency. The response becomes nearly sinusoidal and severe vibrations can occur since resonant behaviour is triggered. [11, 28, 32, 45, 53, 55, 79, 81, 101]
In frequency lock-in, the relative velocity between structure and ice changes between close to zero and about two times ice velocity. Consequently, the failure mode is not uniform over the entire failure cycle. Literature often refers to ductile loading and brittle unloading. However, details of these phases are not well-understood yet. Due to the

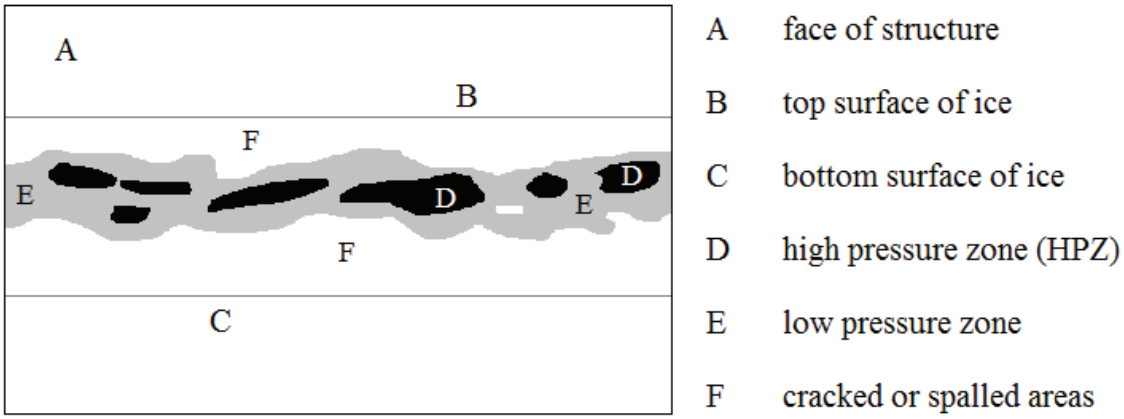

Figure 3: Illustration of contact during continuous brittle crushing with formation of high pressure zones (after ISO 19906:2019 [30], Fig. A-8.11)

resonant behaviour, frequency lock-in causes the most severe ice-induced vibrations. Full scale vibration events that can be attributed to frequency lock-in have been measured for example on lighthouse Norströmsgrund in the Gulf of Bothnia [11], a finnish channel marker [55], and JZ-20 platform in Bohai Bay [101].
Frequency lock-in will be discussed in more detail in Section 2.3.

2.2.3. Continuous brittle crushing

Continuous crushing (CC) occurs on rigid as well as compliant structures when the indentation speed is high. Without change of ice parameters, continuous brittle crushing results in random, stationary load oscillations around a mean value which is mainly defined by structural diameter, ice thickness and ice strength. During crushing, the load is transferred from the ice to the structure through *high pressure zones* (HPZ) forming across the ice-structure interaction area [37, 81]. Spalling and flaking creates a line-like contact with HPZ at center height of the ice as illustrated in Fig. 3, as fractures tend to propagate to the nearest free surface [9]. The average pressure is almost normally distributed over ice thickness. These HPZ are typically arranged in an irregular, discontinuous line. According to laboratory crushing tests with sea ice and tactile sensor measurements, HPZ carry about 80% of the total ice load [70] but cover only 10% of the nominal contact area [15, 86]. Continuous brittle crushing and connected local processes in the ice-structure contact are today reasonably well understood, amongst others because of comprehensive field tests utilizing tactile sensors (JOIA measurements [72]).

2.3. Ice-induced vibrations

Previous sections summarized different failure modes that can occur when drifting level ice fails against a fixed offshore structure. All of these cause structural movement with different peculiarity. When the ice is very slow and fails in creep, the structure is virtually at rest. Flexural failure involves discrete load peaks, which can reach significant load magnitudes, and hence deflect the structure considerably. After failure, structure and ice typically lose contact and the structure oscillates freely until the oscillation either decays or new ice contact establishes. The failure occurs in some distance to the contact since in flexural failure a circular floe breaks off the ice. Therefore, the time span until new contact is established can be quite large, depending on the breaking length of the ice sheet. The load peaks can be rather periodic if the ice parameters remain the same, but normally occur at frequencies clearly below the structure's natural frequency. Such forced vibrations due to discrete load peaks can also arise on sloping structures, although ice-induced vibrations are typically associated with vertically sided structures. A prominent example for severe vibrations caused by flexural failure are vibrations of the JZ20-2 jacket platform in Bohai Bay [100].

Vibrations in intermittent crushing show basically similar characteristics as vibrations due to load peaks preceeding flexural failure, as the structure is deflected by growing ice load and then suddenly released. But intermittent crushing is – without change of ice parameters – virtually periodic, and the oscillation amplitudes can become quite large due to the high ice loads. Since the fracture depth is much smaller in intermittent crushing than the breaking length in flexural failure, there is less time without contact between structure and ice. Periodicity of the process is more pronounced. Recent research by Popko [68] indicates that vibrations due to intermittent crushing are of high relevance for fatigue of offshore wind turbine support structures.

Continuous brittle crushing excites the structure in a broad spectrum. Oscillations in the structure's natural frequencies occur, but are rather small due to the random nature of the load. The ice-induced vibrations occurring in continuous crushing can become significant if the structure is very flexible and the ice load is high. The structural response can be calculated in the frequency domain using power spectral density for random ice action as stipulated in current regulations [30].

The most severe ice-induced vibrations occur during frequency lock-in. Therefore, the term *ice-induced vibration* is often used for the special case of frequency lock-in in literature. Ice-induced vibrations arising in frequency lock-in are subject to further description in the following sections.

2.3.1. Definition of frequency lock-in (FLI)

Frequency lock-in is also referred to as *steady-state vibration* or *(self-excited) ice-induced vibration* in literature, e.g. in [69, 99]. The terms are typically used synonymously, but

sometimes contain relevant information or assumptions, e.g. relating to the physical mechanism that causes the vibration. In this study, the term *frequency lock-in* is used, which can also be found in the latest ISO standard [30].
Similar to the naming issue, there is also no consistent definition of lock-in in literature [57]. For this study, available criteria are collected and FLI is defined as follows[1]:

Frequency similitude
According to ISO 19906:2019 [30], load and response time histories in FLI are periodic with a frequency close to one of the natural frequencies of the structure. This frequency should be smaller than 10 Hz. Literature review reveals that the ratio between dominant loading frequency f_{load} and natural frequency of the structure f_n is typically between 0.95 and 0.98 [28,39]. Kärnä [39] reports on even lower values down to 0.85, but these are rare. Higher values have been found in earlier model tests [58]. Therefore, the condition is set to $f_{load}/f_n = 0.95$ to 1.05 for the present study.[2]
Nord et al. [57] additionally use prominence of the natural frequency in the response spectrum as sufficient condition for FLI. They show that the energy of the response is spread over several frequencies in other interaction regimes, and become a narrow band in the spectrum around the natural frequency during FLI. The judgement on frequency dominance is made by visual inspection. This approach is abandoned for the present study to create an unbiased, automated detection algorithm.

β-ratio
Toyama et al. [92] found a fairly linear relationship between the maximum oscillation velocity of the structure $\hat{u}$ and the velocity of the ice sheet v_{ice}:

$$\hat{u} = \beta v_{ice} \tag{1}$$

Later studies confirmed that such relation exists, and β varies between 0.9 and 1.5 in different full scale and model scale data sets [28,31,32,91]. However, there is no conclusive physical explanation for this relation, and slightly higher values have been reported from experimental test campaigns [24].

γ-ratio
Yap and Palmer [98] quantify the steadiness of response by the ratio of standard deviation of amplitudes $\sigma_{\hat{u}}$ and their mean $\bar{\hat{u}}$:

$$\gamma = \frac{\sigma_{\hat{u}}}{\bar{\hat{u}}} \tag{2}$$

FLI requires γ lower than 0.2.

[1] These criteria have been established at the beginning of the IVOS project [102].
[2] The criterion is set to the limits which are typically found in basin tests. The similitude of load and response frequency is more decisive than the ratio of actual and natural oscillation frequency. The lower boundary could be lowered to 0.85 if the analysis (Sec. 4) shows that FLI actually develops at such low frequency ratio. However, this was not the case for the presented tests.

Dynamic amplification
In FLI, the structural response is amplified by dynamic ice-structure interaction, and thus should be larger than the response to a static load of the same magnitude.[3] This is expressed by a *Dynamic Amplification Factor* (DAF):

$$\mathrm{DAF} = \frac{\bar{\hat{u}}k}{\hat{F}_{ice}} \tag{3}$$

DAF above 1.05 is required for FLI. This limitation is based on literature review and earlier studies, including full scale as well as model scale data analysis [58, 108]. DAF equals *Dynamic Magnification Factor* DMF used in some references, e.g. by Toyama et al. [92].

2.3.2. Full scale data

Full scale data with measurement of FLI is rare. Only few fixed offshore structures have been equipped with load measuring systems due to high costs and effort. Furthermore, FLI is a typically infrequent and to date hardly predictable loading state, meaning that a huge amount of data collected over several months with ice-occurrence is normally required to obtain evaluable FLI vibration events. In recent years, the limited occurrence of sea ice in moderate climate regions further hampered collection of suitable full scale data.
Next to the general problem of full scale data availability, these data sets often additionally suffer from high uncertainty about ice conditions, imperfect measuring systems, incomplete coverage of the ice-structure interaction area with force measuring equipment, and low (or no) resolution of the interaction area.
Probably the most complete data set from a fixed full scale structure is the load measured in the STRICE campaigns on Lighthouse Norströmsgrund [4], shown in Fig. 4. The STRICE data contains load measurements from 9 panels of 1.2 m × 1.6 m size, one of them subdivided into 8 smaller panels. The panels cover 167° of the structure's circumference. The lighthouse was manned during the test campaign; ice samples were frequently tested, and a large research consortium was involved to gather as much data and knowledge as possible. Basic review of the STRICE data used for this thesis has been presented in [58]; some selected information on FLI events is given in App. C.2.
Further full scale measurements of FLI include earlier measurements on the same lighthouse during the LOLEIF project [11, 12, 77], a Finnish Channel Marker [46], JZ-20 3-legged jacket structure in Bohai Bay [101], and the Molikpaq caisson [34]. Most full scale data is not fully open to the research community.

2.3.3. Model scale data

Since the availability and quality of full scale data is insufficient to study FLI systematically, numerous model tests have been conducted throughout the past decades. An

[3] $u_{stat} = F_{ice}/k$; k being translational stiffness of the structure in the direction of ice load.

Figure 4: Photograph of Norströmsgrund Lighthouse with rubble accumulation after crushing failure of drifting level ice (Photo by Kari Kolari, VTT)

overview is given in Tab. 1. Therein, test campaigns which utilized tactile sensors for local load measurement are marked with an x. In the last column, the occurrence of FLI according to the definition stipulated in Section 2.3.1 is checked. It should be noted that this statement is not necessarily in line with the respective author's perception.

Table 1 shows three main shortcomings of the available model test data: Most important, there has been no successful creation of FLI in the frequency range of interest (<10 Hz) under laboratory conditions whith local load measuring system applied except for earlier studies by the author [58]. Additionally, the majority of tests has been performed with small diameter indenters ($D < 0.1$ m) and low aspect ratio. Observations from such tests may not be transferable to full scale structures which typically have larger aspect ratios. Finally, structure and ice parameters have not been varied systematically in reasonable ranges during single test campaigns. Parameter study across all data sets is difficult and prone to adulteration because of different, often poorly reported, setup and test site specifications.

It should be noted that except for tests performed on danish wind turbines [1], a model of the JZ-20 structure [91], and tests based on Lighthouse Norströmsgrund [58,59], most model tests on ice-induced vibrations are considered fundamental research and do not include any scaling of a prototype structure or full scale ice conditions. This circumstance can be mainly attributed to the lack of a validated scaling law for dynamic ice-structure interaction scenarios in ice crushing events. Although research on scalability of ice crushing [65] and dynamic interaction [52,66,97] has been done, there is no consensus on a feasible procedure yet. Further information on this topic is given in Section 6.1.

Year	Reference	Model diameter	Frequency	Local load measurement	FLI
1983	Toyama et al. [92]	0.076 m	1.27 Hz	-	x
1985	Tsuchiya et al. [93]	0.076 m	2.9 Hz 4.7 Hz	-	x
1990	Kärnä and Muhonen [45]	0.1 m	4.1 Hz	-	x
1990	Singh et al. [79]	0.06 m	10.7 Hz 17.6 Hz	-	-
1991	Sodhi [82]	0.05 m	10 Hz	-	-
1992	Timco et al. [91]	0.065 m	7.4 Hz	-	x
1993	Finn et al. [14]	0.08 m 0.1 m 0.12 m	63 Hz	-	x
1994	Izumiyama et al. [31]	0.17 m	5.9 Hz	-	x
1996	Kamesaki et al. [38]	0.8 m	10.9 Hz	-	-
1997	Izumiyama and Uto [32]	0.1 m	5.7 Hz 3.9 Hz	-	x
2003	Kärnä et al. [44]	0.11 m	6.7 Hz	-	x
2005	Barker et al. [1, 19]	0.192 m	9.2 Hz	-	-
2007	Huang et al. [28]	0.076 m	4.3 Hz 6.3 Hz 12.5 Hz	-	x
2012	Määtäänen et al. [56]	0.22 m	7.8 to 12.2 Hz	x	-
2012	Onken [58]	0.83 m	2.65 Hz 5.5 Hz	x	x
2015	Start of IVOS project	0.1 m 0.2 m 0.5 m	2.65 to 7.6 Hz	x	x
2016	O'Rourke et al. [60]	0.02 m	34 Hz 205 Hz	x	-

Table 1: Model tests studying dynamic ice-structure interaction in chronological order. Most recent tests by Hendrikse at al. [21] (2021) are not included since no detailed information is available to date.

2.3.4. Theories on the physical mechanism of FLI

Since the first measurements of durable, resonant vibrations in ice on offshore structures at the Cook Inlet [67], considerable effort has been made to understand and predict FLI. However, it is difficult to really see what happens inside the ice and at the ice-structure interface. Therefore, theory validation is challenging, and no generally acknowledged physical mechanism has been found yet.
Two main theories exist in literature: Self-excitation by some source of negative damping[4] on the one hand, forced vibration by a characteristic failure length on the other.
The idea of a forced vibration resulting from a characteristic failure length of the ice is the oldest approach, first introduced by Peyton [67] and implemented in a model by Matlock and others [48]. The Matlock-model, illustrated in Fig. 5, has been used and modified frequently throughout the past decades (e.g. [7, 49, 96]). Due to its simple implementation, the Matlock model is still widely used to create ice load and response time histories for FLI.

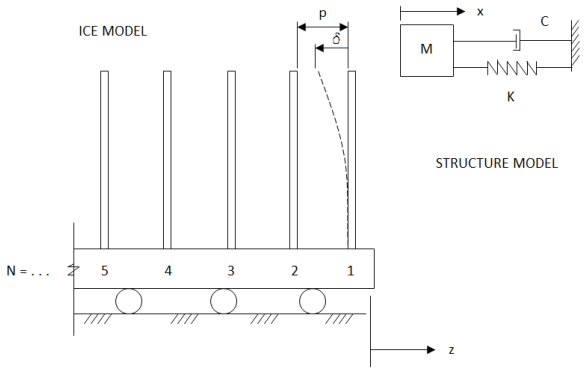

Figure 5: Schematic illustration of the Matlock model, after [48]

The core assumption of a characteristic failure length has been adopted by several researchers and is still subject to ongoing research, i.e. by Palmer et al. [63] and Gagnon [18]. These researchers explain FLI to occur either as a resonance condition between ice which coincidentally fails in the natural frequency of the structure under certain conditions, or as a synchronization of two oscillators (structure with its natural frequency and ice with its characteristic breaking length) [80]. Gagnon [17] substantiated the existence of a characteristic failure length in spalling and flaking events during crushing for a certain data set. However, the laboratory tests from his research group further confirming this theory use high frequency structures up to 900 Hz [18] which do not show the same characteristic load time histories as typical FLI observed at frequencies below 10 Hz. Therefore, this evidence may not be conferable to general FLI with frequencies in a critical range for offshore structures.

[4]The term *negative damping* refers to additional excitation which is dependent on the structure's velocity, thus adding to the damping term in the equation of motion.

Palmer and Bjerkås [63] interpret FLI as a synchronization of oscillators and show evidence for such synchronization in full scale data measured at Lighthouse Norströmsgrund. However, the low resolution of local load measurement systems mentioned above may hide some details contradicting this theory, as claimed by Hendrikse [24] who found several non-periodic local failure events per cycle. However, Hendrikse bases his criticism on measurements of intermittent crushing and forced vibration experiments, not on actual FLI measurements [24, 56].
Although the majority of researchers nowadays refrains from the idea of FLI being a forced vibration caused by characteristic breaking length of the ice, the early Matlock model is still in use to create FLI response time series (e.g. [7]). Recent models combine the basic ideas of a characteristic failure length of the ice with a negative damping mechanism, e.g. [35,36].

The hypothesis of negative damping dates back to 1970 when Blenkarn first introduced a theory about FLI occuring as a result of global load increase with increasing ice velocity [6]. Later models based on the theory of negative damping were developed by Kärnä et al. [43], Määttänen [54], Huang and Liu [27] and Hendrikse [24]. Amongst these, the majority explains the load increase required for sufficient energy flow from the ice to the structure to maintain FLI by a velocity (or strain rate) dependent increase of local strength at the transition velocity between ductile and brittle failure. Schulson [73] and others show such curves, often based on uni-axial compressive strength measurements of ice specimens from sea ice and ice grown in the laboratory.
However, there is no evidence that such increase of strength generally exists. Schwarz [75] did not find a dependence of ice strength on loading rate in tests on warm sea ice. On the other hand, full scale events measured at NSG lighthouse primarily occur when the ice is warmer [5]. However, it should be noted that testing ice samples for strain-rate dependent strength is difficult, and the absence of such trend in one experimental campaign ice does not disproof its existence. Hendrikse [24] postulates that the global ice load increases because the contact area and mean contact pressure grow at low relative speed. Again, there is no compelling evidence that this is the right (and exclusive) source for negative damping.
Models based on a self-excitation mechanism arising from some source of negative damping show reasonable performance in validation against selected full scale data. However, a large group of experts tested the applicability of the most common models to a full scale test case in 2013 [40]. Instead of the developers, non-biased users were asked to perform the calculations. They were given sets of structure and ice parameters known from full scale data. It was found that none of the tested models captured the actual load and response time series sufficiently well, meaning that the predicted failure type often disagreed with the measured one, and in case of the correct failure mode prediction, load and/or response amplitude were not estimated correctly. However, the performance typically improves significantly if the user is allowed to tune the input parameters slightly. Given the uncertainty of several full scale data parameters, including natural scatter of all ice properties and limited accuracy of load measuring systems, such tuning is generally admissible, but disqualifies the respective model for validation of firm assessment

of interaction scenarios. The PSII model developed by Kärnä [44] was chosen as most promising model in the cited study. It should be noted though that models have been optimized or newly developed since the study was conducted, and not all models available at that time were actually investigated. Newer models have not been impartially evaluated since then.
While the study from 2013 highlights the need for further research, it also points out that model validation is difficult due to a limited amount of available full scale and model scale data with sufficient quality and certainty about structure and ice parameters.

2.3.5. Prediction of frequency lock-in

Industry practice to determine the possibility of FLI occurrence for a specific design follows current ISO specifications [30] and includes estimation of ice parameters, generation of a sawtooth-shaped loading function (compare Fig. 6), and time domain simulations. It should be noted that this approach is design oriented and aims at provision of a conservative design load. Since uncoupled simulations are done, the response is not expected to be entirely realistic [78]. Recently, the numerical model developed by Hendrikse has been integrated as a fully coupled model in an offshore wind turbine simulation software, and was certified for the use in design [95].
Next to various numerical models, including (but not limited to) the ones mentioned in the previous section, analytical approaches and simplified mathematical models exist (e.g. [20, 28, 41, 78, 92]). Yap [97] introduced and discussed a dimensionless group – composed of ice drift speed v, structure stiffness at water level k, natural frequency f_n, ice thickness h, projected structure width W and ice peak stress during lock-in σ_{SSSE} – as characteristic feature for lock-in, which can also be used to roughly estimate critical velocities:

$$\frac{vk}{f_n h^{1+a} W^{1-a} \sigma_{SSSE}} \tag{4}$$

Therein, a is an exponent for the aspect ratio accounting for confinement effects. Yap's work shows that the dimensionless parameter generally follows the trend of full scale FLI observations over aspect ratio and nominal contact area, but the distribution of observations around the representing curve for the suggested group shows broad scatter.[5] Interestingly, Yap's dimensionless parameter fits significantly better if model scale data is excluded from the consideration.
A comparative study by Hendrikse et al. [25] compares estimates for critical velocities based on four analytical formulas. They conclude that none of the applied formulas predicts the occurrence of FLI sufficiently well.

2.4. Conclusion - Current knowledge gaps

Above sections briefly summarize several decades of research on dynamic ice-structure interaction. Our understanding has increased significantly since the first full scale ob-

[5] Comp. Fig. 95 in [97].

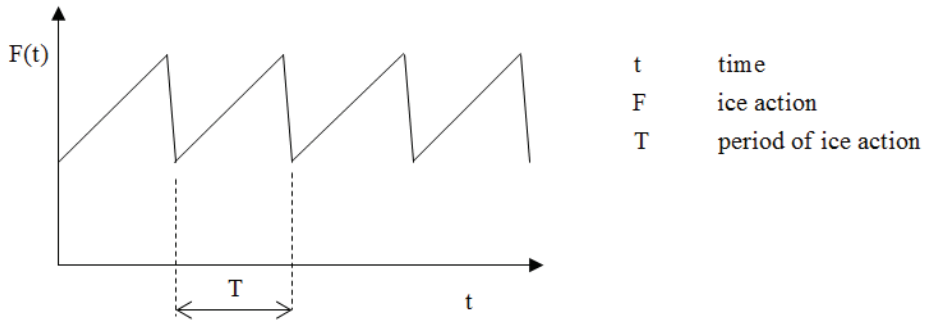

Figure 6: Forcing function suggested by current ISO guidelines to calculate dynamic ice actions (after [30], Fig. A.8-32)

servations and tests. Methods and theoretical models exist that help to predict the occurrence of FLI for prototype structures. However, the interaction process is not fully understood to date, as there is no evidence for the validity of today's most prominent theories. Although it can be assumed that the transfer of higher and periodic ice load from the ice to the structure relates to a velocity-dependence of the local ice action in a broader sense, such mechanism has not been actually observed and physically been proven so far. It remains unclear whether an increase in local strength, increase in contact area, or phase synchronisation of local loads is the decisive factor for onset of FLI vibrations. Consequently, high uncertainty about scalability of the problem, e.g. for investigations in an ice basin, exists, and no fully validated straight-forward method to predict critical velocities leading to FLI is available for design of offshore structures.

3. Experimental investigation of ice-induced vibrations

It has been shown that new model tests are required to increase our understanding of ice-induced vibrations and the possibilities to reliably predict their occurrence without extensive calculation effort.
Gaining insight into dynamic ice-structure interaction by means of model tests requires a suitable setup with clearly defined mechanical properties, and the possibility to vary and monitor several influencing parameters systematically. These parameters include both, structural and ice related parameters. It is inevitable to conduct all tests with a similar setup, and as many tests as possible within one ice sheet, to minimize effects from environmental condition variation on the results.
This study bases on tests executed for the IVOS research project [103]. This data is novel in two aspects: First, it is to date the largest existing model test data set with systematically varied ice and structure parameters for the study of dynamic ice-structure interaction, and second, it contains unique insight into the local contact area and pressure development during frequency lock-in at low natural frequencies, thanks to local pressure mapping. Both aspects are crucial to widen our understanding of frequency lock-in on fixed structures in ice.
The following sections introduce the developed setup and the corresponding test phases.

3.1. Design of experiments

A single-degree of freedom (SDOF) setup is designed for the model tests. The simplification to investigate SDOF systems only is justified by the conservatism of the approach: In MDOF systems, additional modes can interfere with the interaction of the fundamental model and the ice, and may make FLI less likely [78]. In order to gain insight into FLI interactions, the system should be kept as simple as possible to limit unknown parameters and effects.
The experimental campaign was subdivided into three main test phases. Phase 1 was conducted with a test setup previously designed for an earlier project, utilizing a structure mounted to the floor of the basin (passive loading scenario, [58,59], see Fig. 7). The structure's dynamic properties were modelled by a compliant basis (yellow) holding the rigid model (red). The connection of compliant basis and rigid support structure (green) by springs and linear bearings established the required translational stiffness in ice-drift direction and crosswise. Additional weight elements were placed inside the model to achieve the desired natural frequency. Details of this setup and main observations of IVOS Phase 1 are given in Appendix A.2. Due to several imperfections of the setup, it was completely reconstructed for the later test phases, and the results were mostly disregarded for comparative study. The main reason for this decision is the overestimation of flexural ice sheet deformation due to the large aspect ratio, which resulted in frequent flexural failure of the ice, interrupting or even hindering ice-structure interaction in crushing to develop. Additionally, the damping ratio was high due to the large

underwater construction and significant hydrodynamic added mass, and the submerged bearings had a considerable breakaway torque which required large ice loads to start the aspired movement of the compliant basis. Therefore, tests with smaller structures with the same compliant basis would not have been possible due to insufficient ice load.
The improved setup used for all later test phases bases on the same approach of having a rigid model and a compliant basis. However, active loading instead of passive loading is applied for practical matters. The setup and further design considerations are described in detail in Section 3.1.3. Prior to the setup description, the test facility and model ice type are introduced in the following subsections.

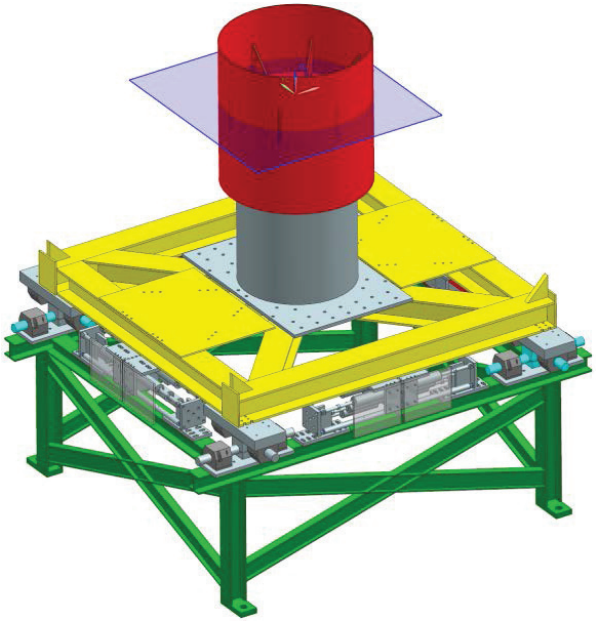

Figure 7: Sketch of physical test setup designed for Phase 1, provided by HSVA's CAD office

3.1.1. Test facility

Ice model tests have been conducted at HSVA's Large Ice Model Basin (LIMB). Details of the basin are given in Fig. 8 and Tab. 2.

The basin dimensions prescribe the maximum available testing length. The properties of the main carriage limit the feasible test speeds and maximum ice load that may occur during the tests, to ensure that the towing carriage's movement is not impeded by the ice load.

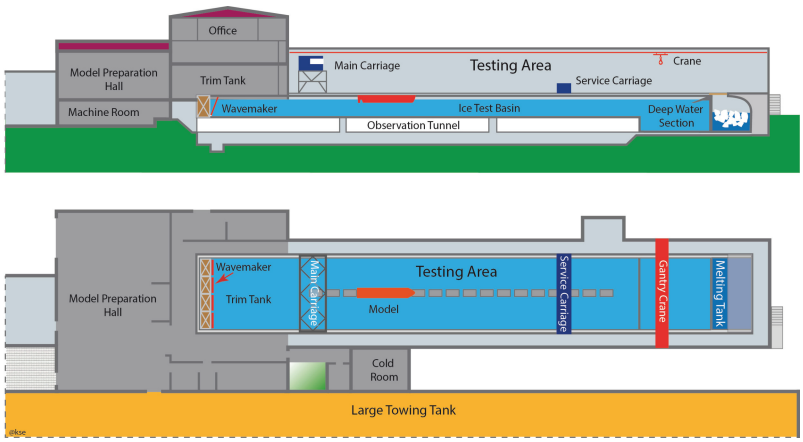

Figure 8: Illustration of HSVA's Large Ice Model Basin LIMB (from https://www.hsva.de/our-facilities/ice-tank.html, visited 2020-12-21)

Tank length	78.0 m
Tank breadth	10.0 m
Tank depth	2.5 m
Ice freezing rate	2 mm/hour
Towing carriage	
Speed range	1 mm/s to 3000 mm/s
Towing capacity	50 kN

Table 2: Details of HSVA's LIMB

3.1.2. Model ice

Tests are conducted in HSVA's standard model ice, which was in the current condition developed in the 1990s [13][6]. The model ice is frozen from a 0.7% sodium chloride solution. This dopant is required to scale the flexural strength of the ice according to Froude and Cauchy similarity, which is state-of-the-art scaling law for ice model tests. The use of dopant and requirement of Froude and Cauchy similarity is comprehensively discussed by Schwarz [76] and Timco [88]. They argue that Froude and Cauchy similitude are required for tests with ships in level ice, as the resistance and propulsion are influenced by ice failing after flexural deformation, and by the size, submergence and transport of broken floes along the hull and into the propeller and wake. Hence, physical model ice was required that provides scaled thickness h, flexural strength σ_f, E/σ_f ratio, and density ratio of ice and basin water.
Effort was made to increase the E/σ_f ratio of model ice, because early ice types suffered from too low model ice stiffness. However, too low ice stiffness is still a debated issue, especially when it comes to application of the model ice for other purposes than testing ice-breaking ships [65, 94].

[6] Note that the scrapping procedure described in the provided reference is no longer applied.

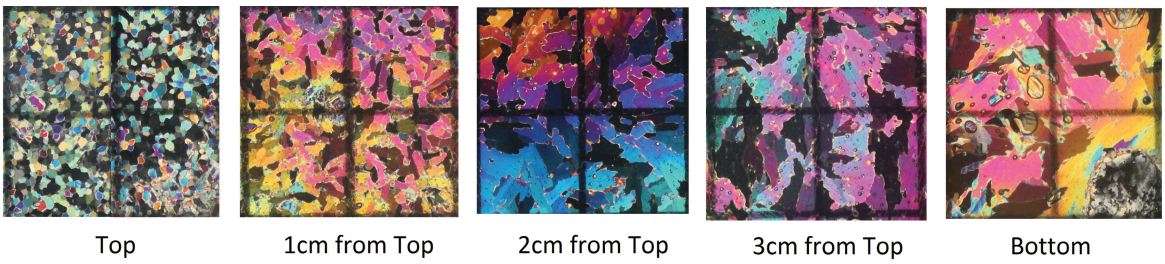

Figure 9: Vertical thin sections of HSVA's standard model ice, taken from the ice sheet grown for Series 25000. Indicated grid size is 1 cm x 1 cm.

Growth of the model ice in doped basin water is initiated by a seeding procedure. Seeding means spraying fresh water into the cold ($-20°$C) air of the ice tank. Fresh water droplets freeze in the air and form tiny ice crystals which settle on the water surface. These crystals initiate growth of fine-grained ice of primarily columnar structure. While the ice sheet is growing, tank water pressure-saturated with air is uniformly discharged from pipes running along the bottom of the basin during the entire freezing process. After release from the pipes, the surplus air segregates from the water. The emerging air bubbles have a size of 200 to 500 μm and rise to the ice sheet, where they are embedded into the growing ice crystals. These air bubbles make the model ice more brittle, decrease its density to maintain a correct ratio of ice and water density ß($\rho_{\text{water}} = 1005$ kg/m^3), and give the ice a white appearance.
When the target ice thickness has almost been reached, the cooling system is switched off and the room temperature rises to $+4°$C. While the temperature rises, the ice continues growing for a few millimetres. When the air gets warmer, dopant comes out of the frozen solution and forms brine pockets in the ice. As the tempering proceeds, these brine pockets drain and thus weaken the ice sheet. When the target flexural strength is reached, the heat transfer into the ice tank is stopped. Although no additional heat is added, the ice strength continues to decrease, but at a smaller rate.
Exemplary thin sections illustrating the crystal size at different heights over the ice thickness are shown in Fig. 9. The standard ice preparation procedure results in a model ice well validated for ship tests, which is more ductile than sea ice, and whose structure over height is inhomogeneous due to the harder fresh water crystal top layer, and the columnar structured ice below.

3.1.3. Test setup

The core idea for the optimized test setup design was to develop a model which can be towed through the ice sheet (active loading) and whose structural parameters, such as geometry, size, natural frequency and stiffness, can be altered between tests in short time.
The new setup is shown in Fig. 10 and Fig. 11. Similar to the initial design illustrated in Fig. 7, the setup contains a rigid model (red), a compliant basis (yellow) and a rigid

support (brown). Here, the rigid support is the main carriage, and the compliant basis is connected via bending rods. By adjusting the number, diameter and length of the bending rods, the translational stiffness in ice drift direction (x-direction) and crosswise (y-direction) can be adjusted. Weight elements placed on the compliant basis serve to tune the setup's natural frequency. The setup was designed in close cooperation with HSVA's CAD office, where all construction drawings have been prepared.

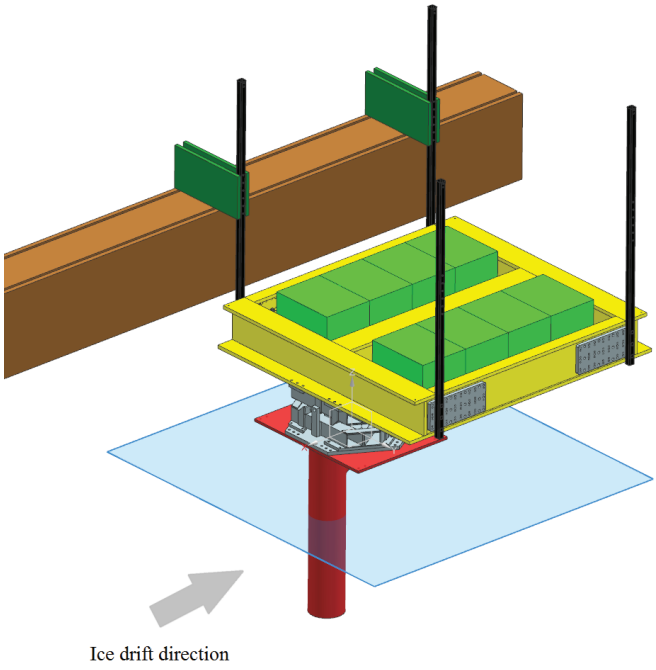

Figure 10: Sketch of the test setup designed for Phase 2 and 3

Linearity of the force-deflection relation and absence of additional dominant frequencies in the response spectrum of the structure in open water condition were proven by pullout and release tests (Fig. 12; details in App. A.1). These were repeated each testing day, and for each new configuration. The setup principle is similar to the *compliance simulator* designed at the National Research Council of Canada (NRC) [1] and also used in tests by Yue and Guo [99], but its dimensions are much larger.

The setup was instrumented with a 6-component load scale connecting the model and the compliant basis, accelerometers on the rigid support structure, the compliant basis and the top plate of the model (connection plate to the load scale), and a laser transducer for movement in x-direction fairly at water level[7]. Additionally, the position and velocity of the main carriage were registered. All above signals plus a synchronization signal

[7] Water level + abt. 8 cm, depending on current water level in the basin which varies a few centimetres between test series.

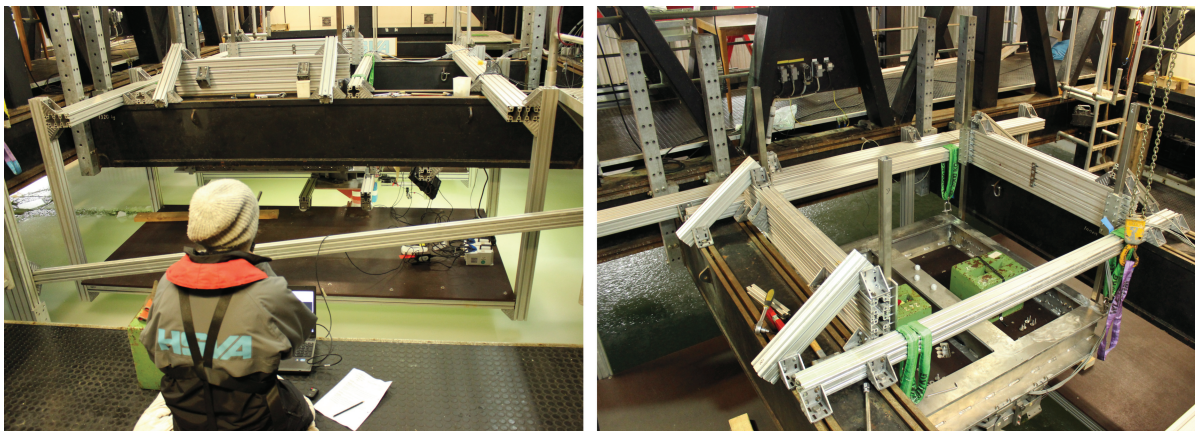

Figure 11: Photographs of the setup installed in the moonpool of the main carriage serving the LIMB

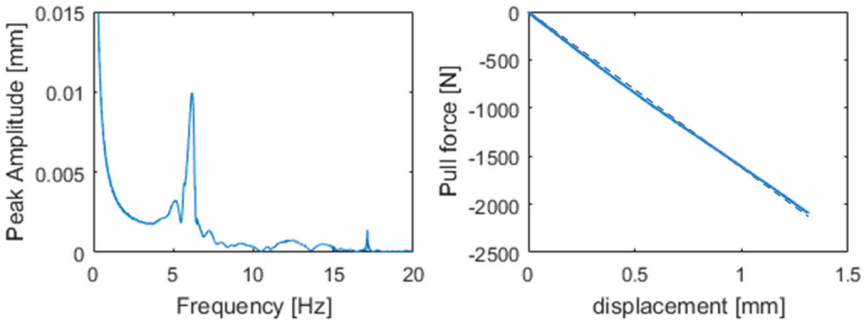

Figure 12: Left: FFT of response time history obtained from plucking test 32001, right: load-deflection curve from pullout test (ideal linear behaviour indicated by dashed line)

were amplified and recorded by the same digital analogue converter (DAC) operated by HSVA's measuring engineers, hereafter referred to as DAC system. DAC system sampled with 600 Hz. In-built low pass Bessel filter (300 Hz) was applied to the data during recording.
The model was further instrumented with tactile sensors from the TekScan system I-Scan with VersaTek high-speed data acquisition electronics. Tactile sensors consist of ultra-thin flexible printed circuits. Each circuit consists of conductive silver electrodes and a layer of pressure-sensitive ink. Sensor elements, called *sensels*, are located at each intersection of two circuits, which are running in rows and columns. When pressure is applied, the electrical resistance between the circuits decreases. This decrease is recorded and interpreted as a raw pressure value.
The VersaTek system cannot be directly included in the DAC measurement. Therefore, a second measuring system – referred to as TAC system – is established for the tests. TAC system recorded at 300.03 Hz. Higher sampling rates were not possible with the

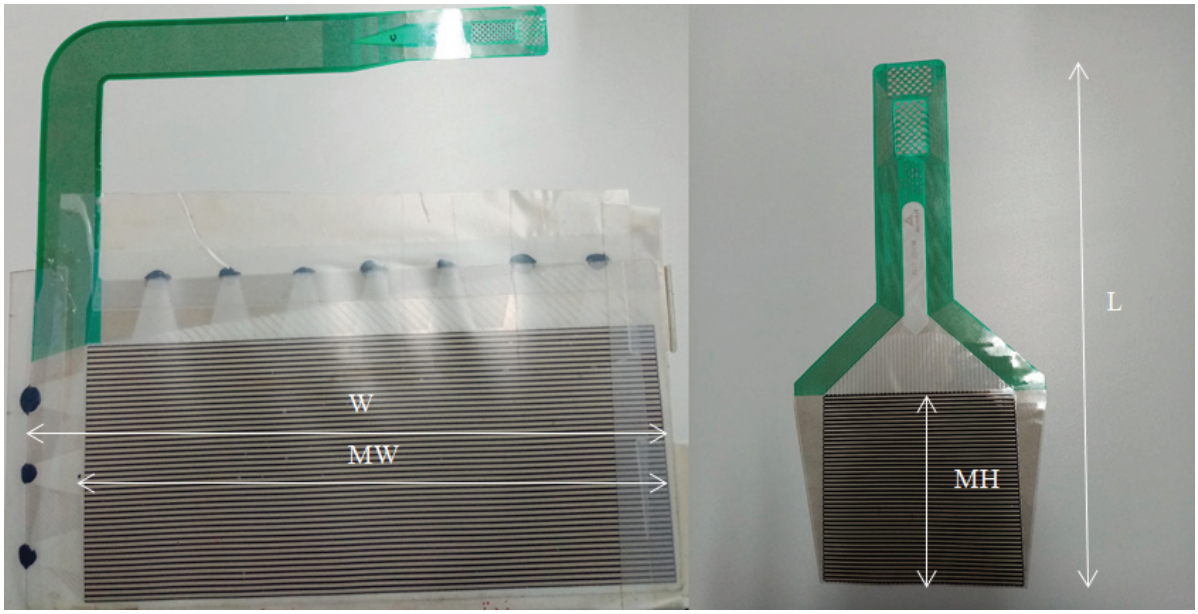

Figure 13: Photographs of Sensor L (Type 5260, left) and Sensor D (Type 5101, right). Sensor L is already prepared for basin tests by sealing of ventilation holes and application of cover foil.

available hardware. The small deviance from 300 Hz results from restrictions in the TekScan software and cannot be changed.
Two sensor types 5101 and 5260, depicted in Fig. 13, were utilized. Sensors type L ("large") cover the entire ice-structure interaction area, while sensor type D ("detailed") is placed at center line of the model to capture detailed pressures.[8] Sensor details are summarized in Tab. 3. A comprehensive description of tactile sensor application in ice model tests is given in App. B and in [105].
Video recordings by two cameras above water and two cameras below water, in both cases one filming from the front and one from starboard side, captured the failure and interaction process visually.

Sensor type	L [mm]	W [mm]	MW [mm]	MH [mm]	Total No of sensels [-]	Resolution [sensel / cm^2]
5260	508.0	536.6	482.1	206.8	2288	2.3
5101	340.0	149.0	111.8	111.8	1936	15.6

Table 3: Details of utilized tactile sensors. See Fig. 13 for explanation of abbreviations.

[8] Sensor D was not operated in all test runs, and Sensor L was not installed during the third test pase.

Conf.	No of tested settings	f_n [Hz]	k [N/mm]	Variation
C1	8	5.5 (0.21)	1935 (276)	Diameter, shape, ice thickness, ice drift speed, ice strength
C2	1	2.65 (0)	490 (0)	ice drift speed, ice strength
C3	2	7.2 (0.40)	3660 (640)	ice drift speed, ice type

Table 4: Basic test cases with mean natural frequency and stiffness, plus their standard deviation between the different test setups in brackets

3.1.4. Test procedure and test matrix

Different structural configurations were tested in varying ice conditions. The majority of tests was performed with base case C1, which was defined based on full scale data from Lighthouse Norströmsgrund [58] and used for successful earlier experiments [107]. Since it proved to reliably lead to lock-in in the laboratory, this condition was kept for most tests. Deviations from C1 were tested to investigate the influence of natural frequency (C2) and to limit the deflection in high load cases (C3). Furthermore, it was seeked to shift the critical velocity range between conditions to validate the prediction formula (see Section 5) and a numerical model [26]. Within C1, structure diameter, shape, ice thickness, simulated ice drift velocity and ice strength have been varied. An overview is given in Tab. 4. The full test matrix is given in App. A.2. Due to different model weight, varying water level and wear of system components, the actual values for stiffness and frequency typically slightly deviated from the target. Standard deviation is given in Tab. 4, actual values in App. A.2. Information on tested models (characterized by shape and diameter, respectively width) is collected in Tab. 5, the models are illustrated in Fig. 14.

Each configuration was tested using stepped velocity profiles for the towing carriage.

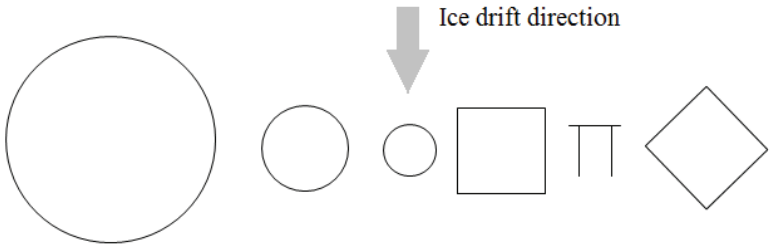

Figure 14: Waterline sections of tested models, from left to right: 500 mm, 200 mm and 120 mm cylinder, 200 mm and 120 mm flat indenter (side-first), 200 mm flat indenter (corner-first)

Series	Run	Shape	Width [mm]	Aspect ratio	Conf.	observed failure mode
21000	21010	cylinder	500	16	C1	IC, FLI, mixed
	21011	cylinder	500	16	C1	IC, CC, mixed
	21020	cylinder	500	16	C3	IC, FLI, CC, mixed
22000	22010	cylinder	200	3	C1	IC
	22110	cylinder	200	2	C1	IC
	22120	cylinder	200	2	C1	IC, mixed
23000	23010	cylinder	200	5	C1	IC, FLI, CC, mixed
	23020	cylinder	500	12	C1	IC, FLI, CC, mixed
24000	24010	cylinder	120	3	C1	IC, FLI, CC
25000	25010	flat, side-first	200	4	C1	IC, FLI
	25011	flat, side-first	200	4	C1	FLI, CC
	25012	flat, side-first	200	4	C1	FLI, mixed
26000	26010	flat, corner-first	283	4	C1	IC, FLI, CC, mixed
	26020	flat, side-first	200	4	C1	IC, FLI, CC
31000	31010	cylinder	120	2	C3	IC, FLI, CC
	31020	cylinder	120	2	C2	IC, FLI, CC
	31030	cylinder	120	2	C1	IC, FLI, CC
32000	32020	flat, side-first	120	2	C1	IC, FLI, CC
	32030	flat, side-first	120	2	C1	IC, FLI, CC
	32040	flat, side-first	120	2	C1	IC, FLI, CC

Table 5: Short test matrix. Full table is given in App. A.2

Times for velocity changes were typically decided spontaneously based on the observed interaction. Some tests were based on pre-defined velocity steps. Whenever possible, the full interaction range was tested in the same test run, thus simulated ice drift speed was varied from 5 mm/s (IC) to 100 mm/s (CC). Exemplary time histories of a typical test run are shown in Fig. 15.

Next to the measurements on the setup, ice properties were recorded. Following measurements were performed:

- Ice thickness: measured at 10 locations on center line before start of tests and in 2 m steps along the broken channel after the tests.
- Ice strength: flexural strength measured at four locations by cantilever beam tests several times during the test day. Compressive strength tested by uni-axial specimen testing in the cold lab close to the point in time when test runs were conducted.
- Ice density and salinity: measured once each testing day, based on three samples.
- Young's modulus: measured once in the morning by plate deflection method (not for each series).

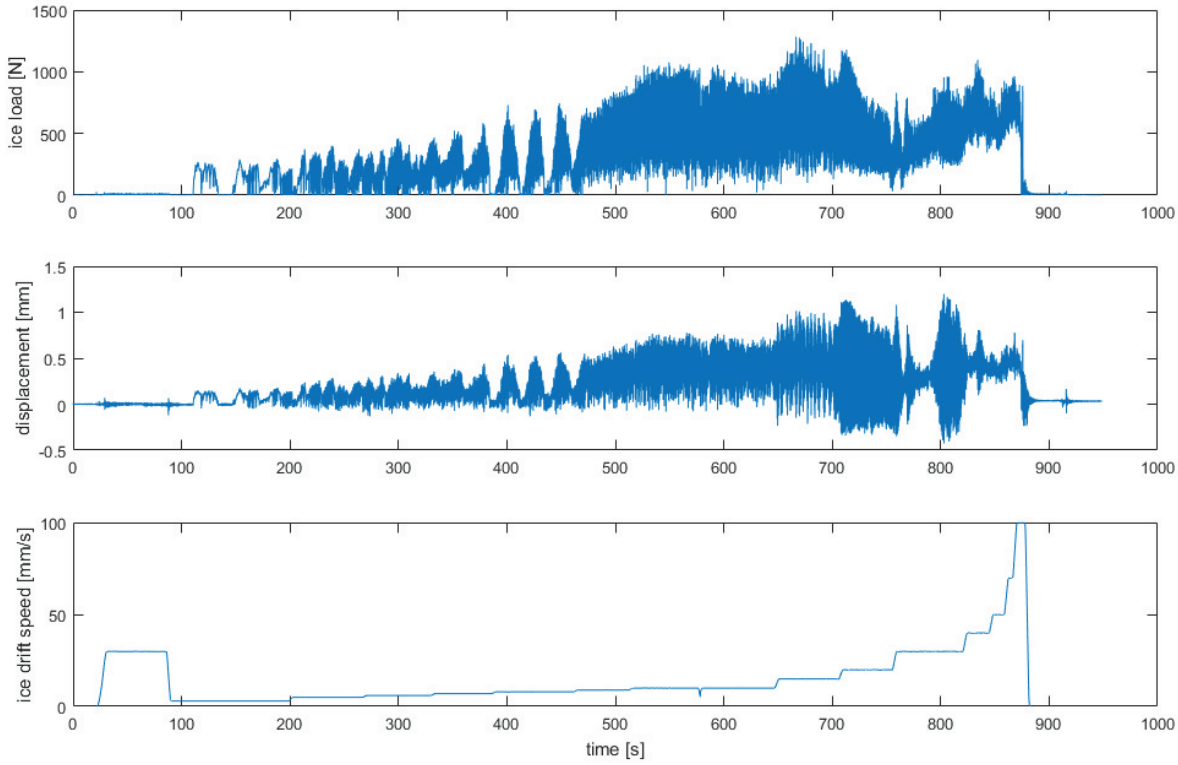

Figure 15: Time histories of total load measured in x-direction (top), corresponding acceleration of the model (center) and stepped velocity profile (bottom) of Run 21020

- Qualitative elastic modulus: Indicative value calculated from cantilever beam tests.
- Crystalline structure: Thin sections taken from the test ice sheet and photographed under polarized light (not for each series).

A description of the standard measuring procedures and summarized properties for each run are given in App. A.

3.2. Main test observations

Model tests successfully delivered data for all types of dynamic ice-structure interaction. Frequency lock-in has been observed for all investigated structural configurations. Some impressions from the model tests are given in Figures 16 and 17.

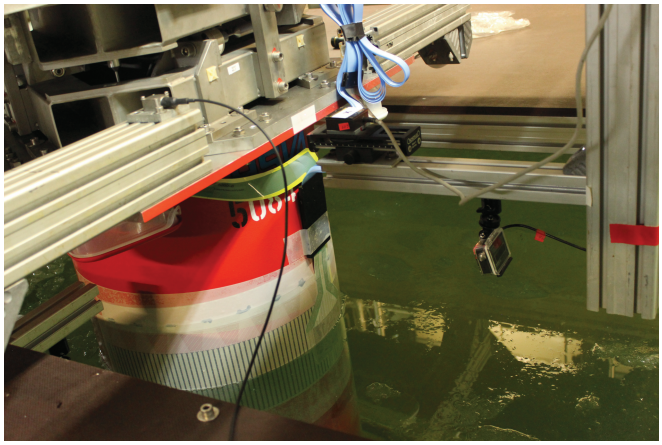

Figure 16: 500 mm diameter cylinder prior to test; Series 21000

Figure 17: 120 mm side-first indenter seen from above and below water, Run 31030

Stationary frequency lock-in could be established under laboratory conditions for almost all tested configurations. It was possible to reproduce the same behaviour in repeated test runs. It was found that configurations with high aspect ratio ($D/h \geq 5$) tend to be affected by superimposed flexural failure next to the desired crushing. Crushing events are frequently interrupted by global buckling or local bending failure of the ice sheet. Furthermore, the ice sheet tends to bend downwards during crushing. Again, this issue is attributed to high aspect ratios. The ice sheet typically crushes against the structure in submerged condition, except for tests in very thick ice (70-80 mm). Therefore, the upward extrusion of crushed ice due to spalling and flaking processes as described in Sec. 2.2.3 is not represented correctly in thin ice.
Some general observations are presented in the following. The observed failure and ice-structure interaction modes are discussed in more detail in Section 4.

Intermittent crushing (IC)
Intermittent crushing has been observed on all models except for the 500 mm cylinder. An exemplary time history of ice load measured by the 6-component scale (raw data) and the structural displacement at water level is shown in Fig. 19. In thin ice, intermittent crushing typically lasts for few cycles only, as it is superimposed by bending of the ice sheet. This additional bending also reduces the maximum ice load exerted at the peaks. An example is shown in Fig. 18. Here, intermittent crushing transforms to continuous crushing and the load level decreases. Videos give evidence that this force reduction and failure type transition coincides with flexural deformation of the ice sheet, causing the ice to bend and finally fail. Intermittent crushing persists for longer durations in thicker level ice, and for increasing aspect ratios of the model. Due to the bending issue, intermittent crushing signals are best for the flat indenters and the smallest cylinders (Series 22000, 25000, 31000, 32000).

Frequency lock-in (FLI)
An exemplary time history of ice load (raw data) and corresponding response during frequency lock-in is given in Fig. 20. As for IC, some FLI events were superimposed by bending of the ice sheet especially for high aspect ratios, which limited the event duration (see Fig. 18). Evaluable events were recorded in all test series except Series 22000; best signals originate from Series 31000.

Continuous crushing (CC)
Continuous crushing is illustrated in Fig. 21. Due to the flexural deformation of the ice sheet, continuous crushing was in most tested scenarios only short-lived. Several tested configurations did not enter proper crushing regime, but instead started ice failure in a mixed mode with global and local bending failure superimposed to short local crushing events.

The observed failure modes are compared regarding their characteristics in Sec. 4.1.

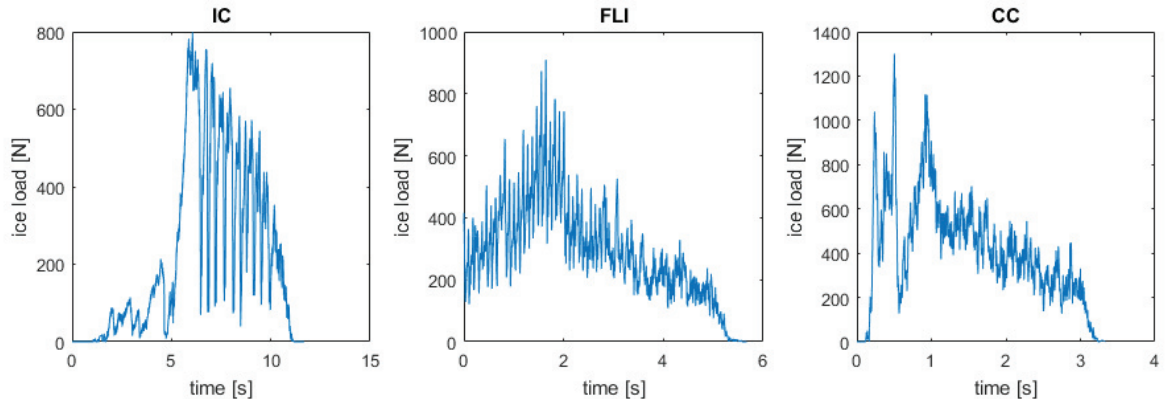

Figure 18: Time history of registered load in x-direction during IC, FLI and CC, all with superimposed global flexural failure (Run 21010)

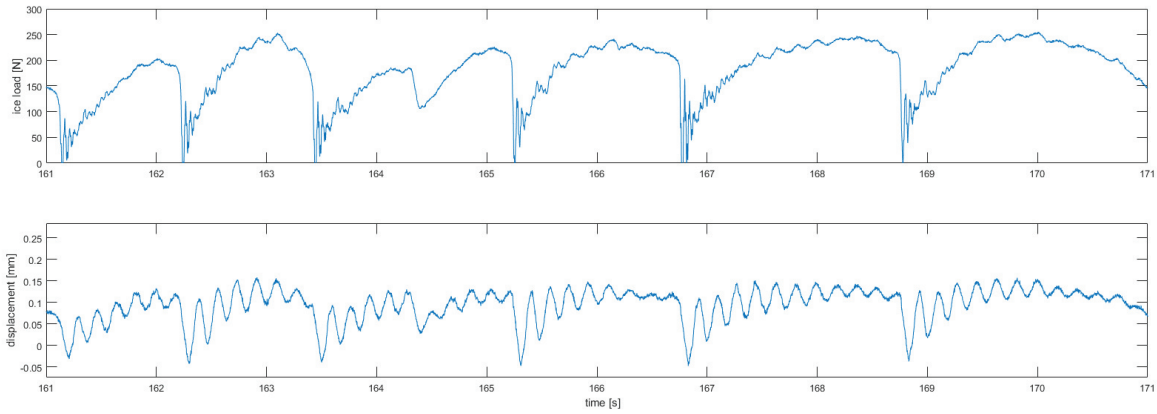

Figure 19: Time history of registered load in x-direction and corresponding deflection of the model during intermittent crushing; from Run 25010 shown in Fig. 15

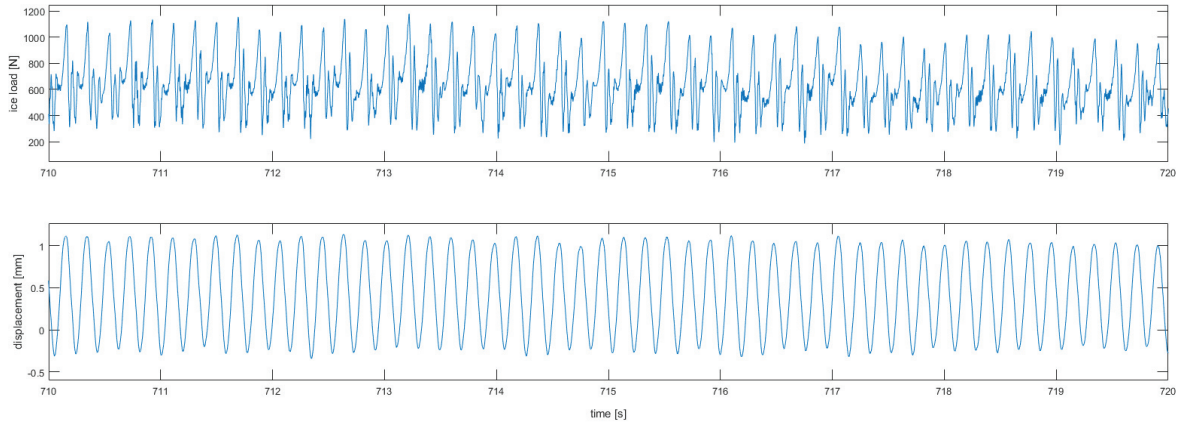

Figure 20: Time history of registered load in x-direction and corresponding deflection of the model during frequency lock-in; from Run 25010 shown in Fig. 15

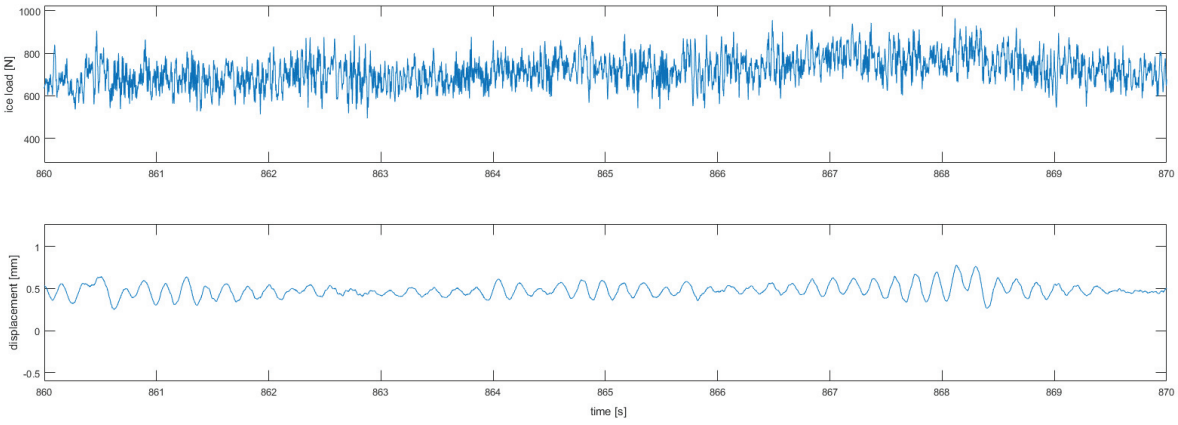

Figure 21: Time history of registered load in x-direction and corresponding deflection of the model during continuous crushing; from Run 25010 shown in Fig. 15

3.3. Data post-processing

Post-processing is applied to several recorded channels. The displacement of the model $u(t)$ and the sum of loads acting on the 6-component scale in x, y- and z-direction are offset corrected by subtracting the mean of the first 100 data points of the respective channels, when all motors were running but the main carriage had not started moving. Structure velocity close to the water level $v_{\mathrm{osc}}(t)$ is calculated by time derivation of the laser signal $u(t)$.
Ice load measured by the 6-component scale and the tactile sensors requires some further post-processing described below.

3.3.1. Load scale data

The 6-component scale connecting the model and the compliant basis is HSVA standard equipment and has an experimentally proven accuracy of 0.25% based on the maximum load of the transducers in the scale (maximum of 5 kN in Phase 2, 20 kN in Phase 3). It should be noted though that the recorded loads $F_{6\mathrm{comp}}(t)$ are not pure ice load F_{ice}, but also viscous (F_{visc}) and inertia (F_{inertia}) force experienced by the oscillating model:

$$F_{6\mathrm{comp}}(t) = F_{\mathrm{ice}}(t) + F_{\mathrm{inertia}}(t) + F_{\mathrm{visc}}(t) \tag{5}$$

In Eq. 5, F_{visc} is negligible for the sake of the study as its contribution to the total recorded load is minor. Inertia loads from the oscillating model below the scale F_{inertia} can be subtracted from $F_{6\mathrm{comp}}$ by calculating their time history from the measured model acceleration a and the oscillating mass M_{osc}, which can be derived from plucking tests in open water. A similar approach has been used by Timco [91] for a comparable setup. It should be noted that this approach is not fully valid, because the model actually oscillates in more than one mode, and the contributions of each mode differ between the different interaction scenarios. Furthermore, the recorded acceleration is a combination of actual model acceleration, and oscillation of the accelerometer in its foundation. Therefore, inertia load correction is only applied to tests with heavy models (all tests from Phase 1; tests with 500 mm cylinder in Phase 2, Series 21000 and 23000). Without correction, characteristic artefacts occur during lock-in which are shown in Fig. 22. Comparison to TAC data which is independent from inertia loads gives evidence for the actual load time characteristic.

3.3.2. Pressure sensor data

Local pressures have been recorded with tactile sensors from Tekscan. Application of these sensors in ice experiments is a controversial issue. After several pre-tests and earlier test campaigns, a solid procedure how to prepare and install the sensors to receive valid pressure recordings has been found. Details are summarized in [105] and described in App. B. The sensors record uncalibrated raw data, and as stated above, the pressure is sampled at a different rate than all other measurements. Furthermore, tactile sensors only record normal pressure, which is not directly comparable to the load registered

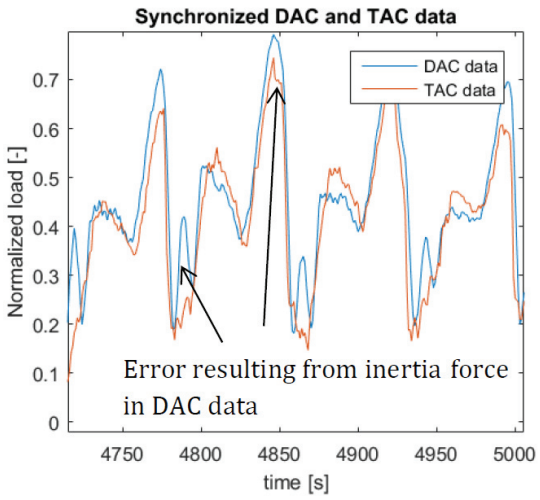

Figure 22: Comparison of DAC and TAC measurement during FLI, indicating artefacts from inertia loads registered by the 6-component-scale.

by the 6-component-scale in case of cylinder or corner-first indenter tests. Therefore, post-processing has to be applied.
For post-processing, the test runs are subdivided into time histories with constant velocities, such that each velocity step is treated individually. This is important because ice failure type and impact of shear forces change with changing velocity, and so does the calibration coefficient. Additionally, time histories with constant velocity are more suitable for further analysis.
The actual calibration contains eight steps:

1. **Choice of active area**
   The relevant area in contact with the ice is manually chosen based on an illustration of the maximum recorded raw pressure in each sensel for the current velocity. This step is needed to limit the amount of data and speed up the calculations, but also to exclude parts of the noise which can occur on the sensor above the ice contact due to current noise and internal stress. Fig. 23 illustrates this step.

2. **Threshold application**
   A threshold value is set individually for each test run, based on visual inspection of the recorded maximum pressures for each sensel. This threshold is meant to exclude noise and low rubble load from the data. The noise load level can be seen in Fig. 23. It varies between the tests because the sensor sensitivity was not always set to the same level, depending on the maximum load expected for the respective test run. All recorded sensel pressures below the threshold value are set to zero.

3. **Noise reduction**
   Noise is further reduced by zeroing isolated sensels which show a load (above threshold) but are not connected to the ice interaction zone. The effect of steps

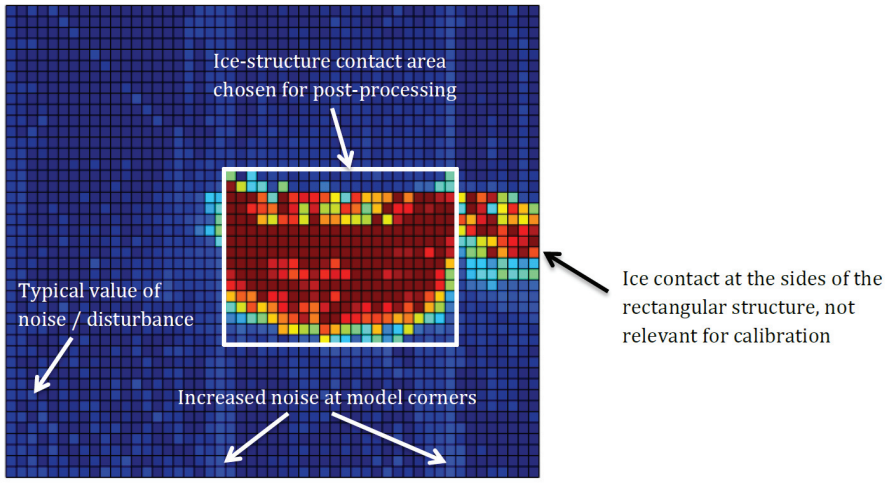

Figure 23: Maximum raw pressure on each sensel during Run 25010 (flat indenter, side-first)

1 to 3 is shown in frequency and time domain in Figures 24 and 25. It confirms that the noise is reduced while the characteristics in the lower frequency range are preserved.

4. **Global load calculation**
   The global ice load in x-direction (moving direction of the carriage) F_{TAC} is calculated from the sensel loads:

$$F_{\mathrm{TAC}} = \sum_{i=1}^{CQ} \sum_{j=1}^{RQ} p_{i,j} CW RW \left(\cos \frac{2CW\,(i-1)}{D} + \mu \sin \frac{2CW\,(i-1)}{D} \right) \tag{6}$$

   In Eq. 6, i and j are the column and row position of the referred sensel in the tactile sensor matrix. Column quantity CQ and row quantity RQ differ between the tests depending on the model size, and on the size of selected active area. The raw pressure $p_{i,j}$ is recorded on each single sensel. Row width RW and column width CW define the area of the sensel. The diameter of the cylinder D can also refer to the projected indenter width W in case of a flat model. The wet ice-structure friction coefficient μ is 0.1 and was found in friction tests previously performed at HSVA with a model ice sample and an aluminium plate, painted with the same paint as the models, and covered with the same protection foil as used to preserve the tactile sensors.[9]

5. **Resampling**
   F_{TAC} and F_{DAC} are downsampled to 100 Hz to unify the sampling rates of both time histories and to limit the amount of data points used for the calibration. Matlab built-in resampling function based on an FIR anti-aliasing low pass filter with Kaiser window method is utilized.

[9] A short description of the friction test procedure is given in App. A.1.

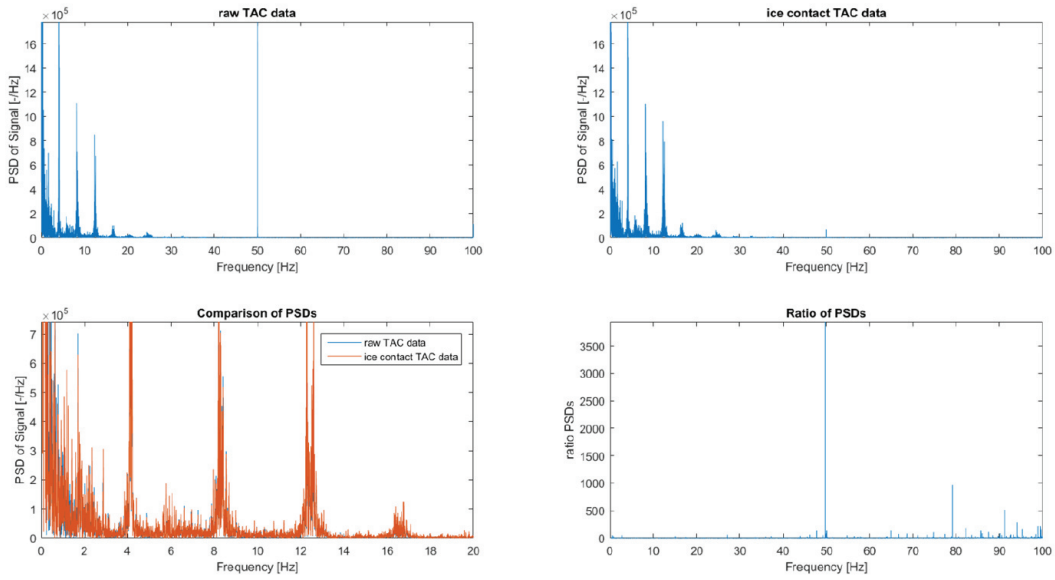

Figure 24: Power Spectral Density (PSD) of raw and noise-attenuated TAC data

6. **Time history synchronization**
   TAC and DAC data are recorded on different measuring systems. Their start and end times are not aligned. Therefore, the resampled time histories need to be synchronized. This is done automatically by cross-correlation of the two time series and shifting the TAC data by the number of samples found by identification of the maximum cross-correlation factor. TAC and DAC data are then cut to the same length.

7. **Linear regression analysis**
   In the downsampled and aligned time series of DAC and TAC data, each data pair for each time frame can be used for calibration. All data pairs are taken into account by a linear regression analysis. Tests have shown that the utilized sensors

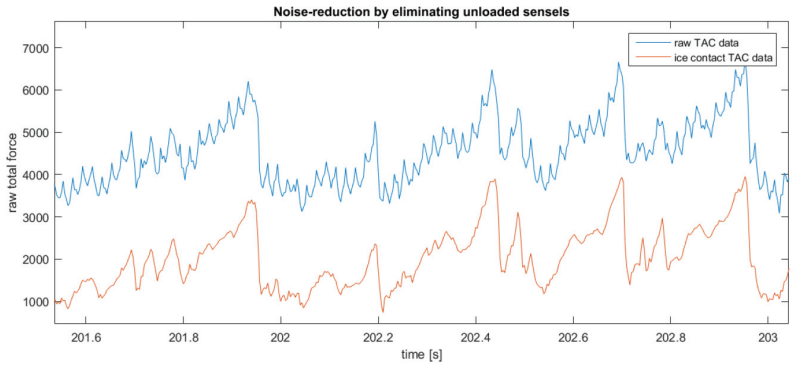

Figure 25: Time histories of raw and noise-attenuated TAC data

behave fairly linear in the considered pressure range. The linear regression provides linear calibration factors for each velocity interval. In a few cases, a constant offset is added to the linear calibration factor to better match the data. However, adding an offset results in unrealistic pressures on marginally loaded sensels. When calibrated pressures become negative, they are set to zero to maintain correct physical behaviour.
Two examples of calibrated TAC load data compared to DAC measurement are shown in Fig. 26. Histogram plots indicate a fair match over the entire load range.

8. **Application to high frequent TAC measurement**
The linear calibration factors are applied to the noise-attenuated TAC time histories (steps 1 to 3, no normalization nor downsampling) to keep the original high sampling frequency for the analysis. The measured model displacement u is resampled to 300.03 Hz using the above mentioned function to obtain a model position value for each time frame of the pressure measurement. No error is anticipated by resampling the displacement time history as the model oscillates in frequencies clearly below 20 Hz, and no physical movement at higher rates is expected.

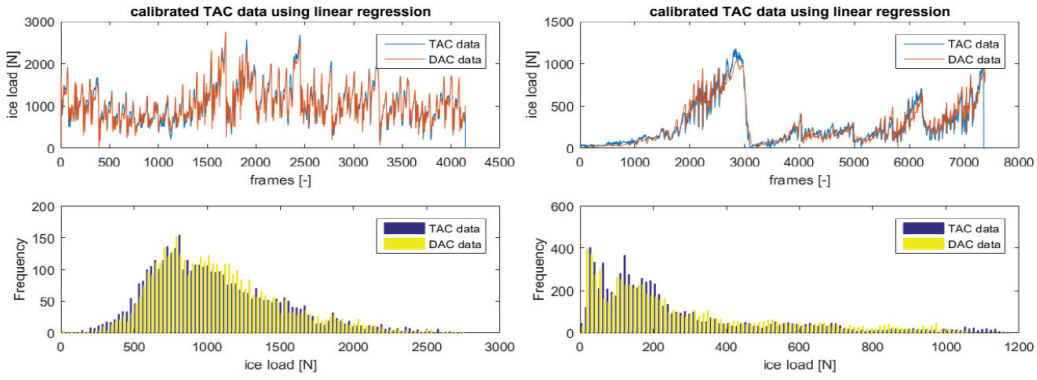

Figure 26: Exemplary time histories and corresponding histograms for events measured with 19 mm/s (left) and 5 mm/s (right) ice drift speed (Flat indenter, Run 25010)

The coefficient of determination R^2 is calculated for all calibration factors to judge their quality. It indicates how much of the data variance can be explained by the linear regression, assuming a Gaussian distribution around the best-fit line. Exemplary calibration factors and corresponding R^2 values for a single test run are given in App. B (Tab. 18). With R^2 typically above 0.9[10], most calibration factors match the time series reasonably well, given the considerable uncertainties introduced by the experimental setup itself, and the simplifications applied to post-process the measurements.
After post-processing of the pressure data, measurements can be used to assess the local

[10]Mean of all calibrated test runs: 0.93; Minimum R^2 0.75, Maximum R^2 0.98, Standard deviation 0.03.

contact development between structure and ice and the process of pressure transfer. Based on the nature of the sensors and the simplifications applied during the calibration process, the results have to be analysed keeping in mind some basic limitations:
Only normal loads are recorded correctly. Shear forces can only be estimated based on the normal forces. Furthermore, the constant load offset occurring in some test runs cannot be subtracted correctly for small loads. Therefore, small loads can be unreliable and have to be inspected carefully during analysis.
It is impossible to distinguish between actual, but low-pressure contact and rubble load. Time histories of a single sensel on the sensor do not reflect physical processes in the ice, as the ice sheet is moving up and down during interaction. Therefore, the position of contact changes. A sensel with decreasing load hence does not necessarily indicate a reduction of actual pressure, but could also stem from a change of contact position.
Due to a certain rise-time of the registered load in the sensels, the calibration factors differ depending on the interaction type due to a low pass filter effect. Calibration factors are lower for intermittent crushing than for continuous crushing. This behaviour is illustrated by plotting the calculated linear calibration factors over the corresponding ice drift speed for one exemplary test run in Fig. 27. Overview over all calibration factors and their velocity dependence for the different test runs is given in App. B (Fig. 79).

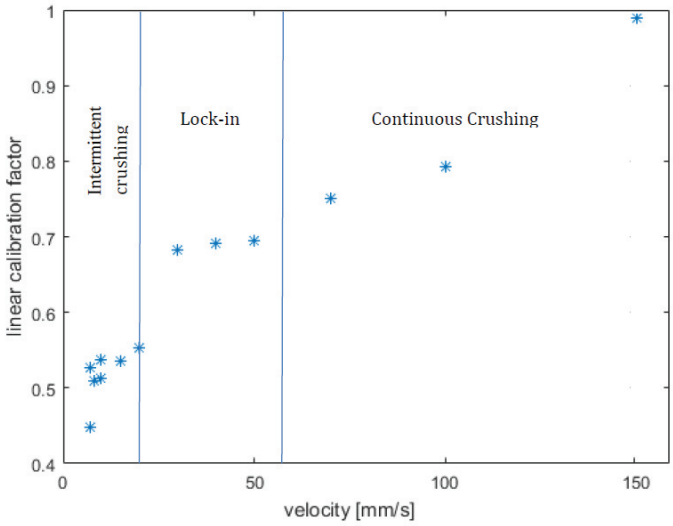

Figure 27: Calibration factors for different tested ice drift speeds (Run 25010)

4. Analysis of experimental data

The experimental data is analysed with emphasis on the differences between the different crushing regimes of intermittent crushing (IC), frequency lock-in (FLI) and continuous crushing (CC). As a first step, FLI events are identified based on clear criteria. IC regime is then defined as the velocity interval up to the lowest FLI velocity, and CC starts above the highest velocity where FLI has been identified.
The three regimes are compared in time and frequency domain regarding local and global ice loads, and the development of contact area during the different interaction types. This analysis demonstrates unique characteristics of FLI, which are then further investigated. Based on the analysis of high pressure zone behaviour during FLI, the interaction process can be described in detail, providing novel insight into the physical process allowing FLI to develop. Finally, the experimental observations and derived explanations for FLI development are briefly compared to full scale observations, and findings are discussed with respect to state-of-the-art theories.

4.1. Comparative investigation of crushing regimes

Comparative analysis of the different crushing regimes requires identification of the regimes. The automatic identification of frequency lock-in events is described below.

4.1.1. Identification of frequency lock-in

A Matlab routine is written to automatically detect FLI events following the criteria defined in Section 2.3.1. The time series for each tested velocity are subdivided into segments with a number of data points defined by the event length l:

$$l = 5\frac{1}{f_n}F_s \tag{7}$$

Herein, F_s is the sampling rate after post-processing, f_n refers to the eigenfrequency of the structure in open water, and the factor of 10 is chosen to ensure a reasonable number of cycles to be evaluated for the event identification. The segments have an overlap of $9T_n$ to enable precise identification of the onset cycle. For each part, all amplitudes of structure velocity v_{osc} and structure displacement u are registered, and three values to check for lock-in are calculated from their arithmetic means (marked with an overbar):

$$\beta = \frac{\overline{v}_{\mathrm{osc}}}{v_{\mathrm{ice}}} \tag{8}$$

$$\gamma = \frac{\sigma_{\hat{u}}}{\overline{u}} \tag{9}$$

$$\mathrm{DAF} = \frac{\hat{u}k}{\hat{F}_{TAC}} \tag{10}$$

Eq. 8 calculates the relation β between structure and ice velocity. If β is between 0.8 and 1.4, this condition for lock-in is met.[11] γ reveals the variation of oscillation amplitudes, which should be lower than 0.2 in lock-in. The dynamic amplification factor DAF indicates how much the actual displacement (mean of 10 amplitudes, $\bar{u}$) is amplified compared to a static load scenario with average maximum load $\hat{F}_{TAC}$ and structure stiffness k. Minimum DAF is set to 1.1.
Finally, fast Fourier transformation (FFT) is applied to part time histories of structural oscillation and global ice load. The frequency similitude criterion is met if the peaks identified in the respective spectra do not differ by more than 5% in frequency. In the automatic peak identification, the highest peak corresponding to a frequency higher than 1 Hz is considered, as lower peaks refer to the slowly varying load components and not to the dynamic part which is decisive for lock-in.
After checking all segments for these criteria, the longest time span meeting all requirements is chosen, such that each test velocity leading to lock-in gets one evaluable lock-in event. The γ-criterion is calculated again for the entire event. If the criterion is not met, the event is shortened in steps of $\frac{F_s}{f_n}$ until γ is 0.2 or lower. The finally identified lock-in event can last for some fraction of the event duration only, or span the entire measurement. In addition, the ratio of checked time frames meeting the different lock-in conditions is recorded. Fig. 28 (top) displays time series of global ice load and structural displacement for 38 s of constant ice speed. The test run starts with a high load peak, probably the first contact of structure and ice which often results in flexural failure. Therefore, there is no ice load after the initial peak, but some oscillations of the structure. When the contact establishes and the ice load increases, load and response become periodic and show the typical saw-tooth load and sine response of FLI. The script identifies the onset well according to the described criteria. Fig. 28 also demonstrates how transition velocities with interrupted FLI events are recognized.
In total, 48 lock-in events were found in 309 tested combinations of ice velocity, structural stiffness, oscillating mass, ice strength and thickness.

The systematic FLI identification proposed above clearly distinguishes FLI and transition stages towards FLI (both from IC and towards CC) from other interaction modes. *Transition* is defined as an interaction which fulfils two or more of the FLI criteria for at least parts of the test. IC and CC regimes are simply defined as lower and higher ice drift velocity ranges, assuming that the lowest tested ice drift speed was always well above creep velocity. Decision about clear or mixed failure mode in CC and IC is based on visual inspection. If global bending failure frequently interrupts the interaction, the particular test case is registered as a *mixed mode* interaction. Criteria for the clarity of modes are set to a minimum of 5 consecutive saw-tooth shaped loading cycles in IC, and 2 s duration of continuous crushing with constant mean load level for CC, to ensure a sufficient number of cycles and sufficient amount of data points for comparison with the

[11] The lower boundary for β was set here to 0.8 instead of 0.9 because there is no physical explanation for the lower limit, but events have been found in the analysed data which show clear FLI characteristics at $\beta \approx 0.8$.

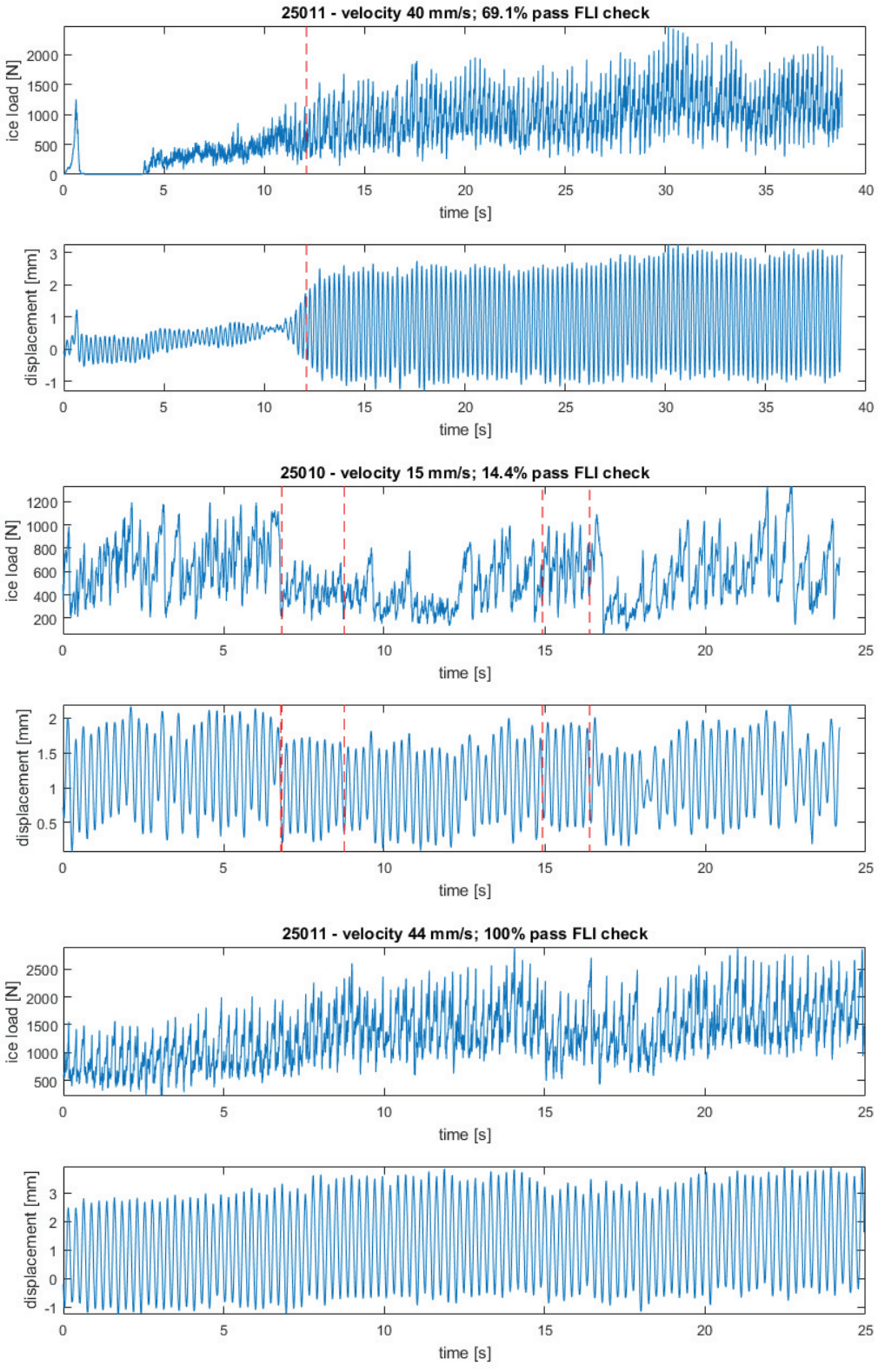

Figure 28: Examples of identified lock-in events in Run 25010 and 25011.

shortest possible FLI event with length l.
Table 6 lists all velocities resulting in clear IC, FLI or CC for the respective test runs. This table provides information on the number of evaluated events for each test run for later analysis. Clear FLI occurred in nine test runs, four out of these have more than three FLI velocities. Despite the extensiveness of the test campaign, the number of tests utilisable for the following analysis is small when it comes to statistic analysis. Only five test runs contain measurements of all crushing regimes of interest. The number of IC and CC events is typically lower than the number of FLI events from the same run. Hence, mean values from FLI are statistically more profound than the values from IC and CC regime they are compared with. The time series of all evaluated clear events are shown in App. C.1.

Run	Ice drift velocities [mm/s]		
	IC	FLI	CC
21010	6, 7, 8	20	80, 90, 100
23020	9, 10	21	-
24010	3, 4	28, 29, 30, 31, 32, 33, 34, 35, 36, 37	99, 105, 128, 148, 159, 192
25010	-	13, 15, 20	-
25011	-	40, 41, 42, 43, 44, 50, 55, 60, 64, 70, 75, 80	110, 120, 130, 139, 150
26010	5, 6, 7, 8, 9, 10	15, 20	50
26020	-	27, 28, 29, 30, 31, 32, 33, 34	69, 80, 100, 150
31030	5	24, 50, 55	201
32030	5, 10, 15	45, 50, 55, 60, 70, 75, 85, 100	150

Table 6: Velocities for IC, FLI, CC based on FLI identification (no transition modes)

Clear CC mode has rarely been measured, as the interaction often remained in a transition mode from FLI towards CC in increasing ice drift speeds when velocity increments were small, and global buckling occurred when the velocity was increased by larger steps. In the low indentation speed range, the failure was also often disturbed by global flexural failure, and clear IC primarily developed in thick ice and interaction scenarios with low aspect ratio.
An example for buckling load time series is shown in Fig. 29 for Run 23020 with 500 mm diameter cylinder. At model center line, the 41 mm thick ice sheet submerges up to 70 mm.[12] Considering the model to be representative for NSG lighthouse at a

[12] Value indicative; based on image analysis of videos and tactile sensor grid dimensions.

geometric scale of 1:15, this would indicate a submergence of an about 600 mm thick level ice sheet by about 1 m. No comparable observations have been made in full scale. The high impact of flexural ice sheet deformation in tests with saline columnar model ice is further addressed in Sec. 6.2.1. Analysis of local pressures shows that especially in thin ice and with high aspect ratios, the load is mainly transferred from the ice to the structure by the model ice' top layer, which does not reflect sea ice crushing as introduced in Sec. 2.2.3. Therefore, the following analysis mainly concentrates on Phase 3 tests (Series 31000 and 32000) with high model ice thickness and low aspect ratio low, where contact correctly established at center height of the level ice sheet.

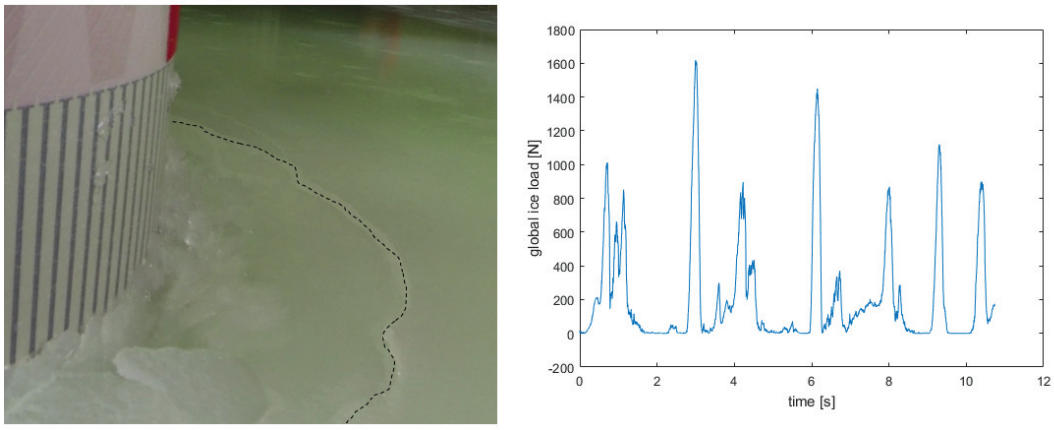

Figure 29: Left: Snapshot of video taken during Run 23020 with indication of circumferential crack resulting from flexural deformation of the ice sheet; right: corresponding load time history, v=70 mm/s (above FLI range; CC expected).

Tab. 7 gives an overview of identified interaction types for all tested structure and ice configurations. Therein, general boundaries for the different regimes are given, while single exceptions are neglected (e.g., there are several transition cases in the FLI regime marked for Run 25010 / 25011, but minimum and maximum velocity where clear FLI occurred are chosen as limiting cases for representation). The coloured boxes indicating FLI and transition regimes (Tab. 7) show that no ultimate critical velocity exists for model ice which always leads to FLI. However, an ice drift speed of 20 mm/s was critical for all tested configurations, as it resulted at least in a transition mode for all test scenarios.

4.1.2. Characteristics of different crushing types

The identification of crushing modes reveals that the interaction of model ice with a vertical structure is immoderately influenced by flexural deformation of the model ice sheet if the aspect ratio is high. For aspect ratios greater than three, the ice fails in buckling rather than in crushing. Submerged ice contact often establishes at low inden-

v [mm/s]	21010	21011	23010	23020	24010	25010/ 25011	26010	26020	31030	32030
5	IC	trans / mixed	IC / mixed	buckling	IC / mixed	buckling	IC	trans	IC	IC
10				IC		FLI			trans	
15	trans		trans / mixed	trans			trans	FLI		trans
20	FLI			FLI	FLI		FLI		FLI	
25	trans			buckling			trans	trans		
30		CC			trans		CC		trans	FLI
35						trans		CC	mixed	
40	CC		CC		CC	CC				trans
45										
50										
55										
60										
65										
70										
75										
80										
85										
90										
95										
100										
150										
200									CC	CC

Table 7: Identified failure modes depending on ice drift speed for different structural and ice parameters. Parameters are compiled for each Run in Tab. 5

tation speed, and prevails until the end of the test run, or global flexural failure. The contact area remains at water level when the model diameter is small and ice thickness is high.
Despite this issue, the data can be used to assess the load and response characteristics of the different types of crushing and corresponding dynamic response.
In this section, main characteristics of the three crushing regimes of interest are assessed. Only clear events are included in the comparison and transition stages are omitted.

Characteristics in time domain

Exemplary time series of load and response during IC, FLI and CC obtained in Run 32030 are given in Fig. 30 to Fig. 32. The time history of intermittent crushing shows that structure and ice remain in full contact over the entire – or almost the entire – interaction cycle. The structure is deflected as the global load increases until strength capacity of the ice is reached. Afterwards, the ice fails over the entire contact area. When the ice crushes, the structure moves towards its equilibrium position with the same speed as the ice edge moves due to local failure. While the structure moves back, it slightly vibrates in its natural frequency, which is much higher than the frequency of global ice failure.
Structure and ice also remain in contact during FLI. The load time series shows a fairly periodic pattern, and the response is almost sinusoidal. The load drop following the global peak load is less steep than in IC, and does not decrease to zero. Several load

cycles show a force plateau when the structural displacement is small. Load peaks are aligned with deflection maxima, and deflection minima are delayed to load minima. Fig. 33 compares an exemplary measurement of deflection during FLI from Run 32030 to a sine function with an offset corresponding to the mean deflection, oscillation frequency as obtained in FFT of response (comp. Fig. 34), and amplitude matching the peak amplitudes of the considered interval, thus a theoretical free oscillation without damping. The difference between the FLI measurement and the sine function is – next to the natural scatter of actual measurements – mainly a slower movement when the structure approaches the offset maxima, shown by a lower inclination of the deflection curve compared to the free oscillation.
Load and response time series in CC are different. The natural frequency of the model is visible in the response, superimposed by additional higher frequencies. There is no periodicity in load, which is also evident in the FFTs shown below (Fig. 34).

Basic characteristics in frequency domain
Load and response spectra obtained by FFT are presented for examples of IC, FLI and CC in Fig. 34. These show that the spectra of load and response in IC are similar, which reflects above observations. Compared to FLI and CC, the low frequency range shows significantly higher amplitudes, but no clear peak frequency. Load and response have the same dominant peak in FLI, close to the natural frequency of the structure. First harmonic oscillation is also prominent in the spectrum. The harmonics disappear in CC, and the natural frequency is dominant in the response spectrum, but not in the ice load.

Characteristics in phase space
The three main crushing regimes can also be compared in phase space. Delay representations or *phase portraits* are exemplarily given for three tested velocities from Run 32030 which depict IC (v=5 mm/s), FLI (v=55 mm/s) and CC (v=150 mm/s) in Fig. 35. Delay τ=0.03s is chosen for a fair phase space reconstruction for FLI, and for reasons of comparison also for CC. Delay τ=0.33s reveals the attractor in IC more clearly.
IC and FLI response time histories show attractors in phase space. CC is a generally more stochastic process and no attractor was found. Structure displacement and global ice load are similar in time and phase state during IC, while the attractors of load and response during FLI show significant differences.

The previously shown differences in load and response time characteristics result in differing load levels across the failure regimes, which are compiled and compared in Tab. 8. Therein, arithmetic mean values – indicated by an overbar – are calculated based on the entire event duration. Average peak loads – marked with a hat – are calculated by identifying the peak loads of each cycle, and averaging these by the number of peaks. For the almost periodic FLI time series, the peak load identification is based on the oscillation period of the structure, which defines the minimum peak distance. For consistency, the same peak distance is defined for CC. However, the slower load build-up in IC requires a larger peak distance to ensure that only one peak value is evaluated

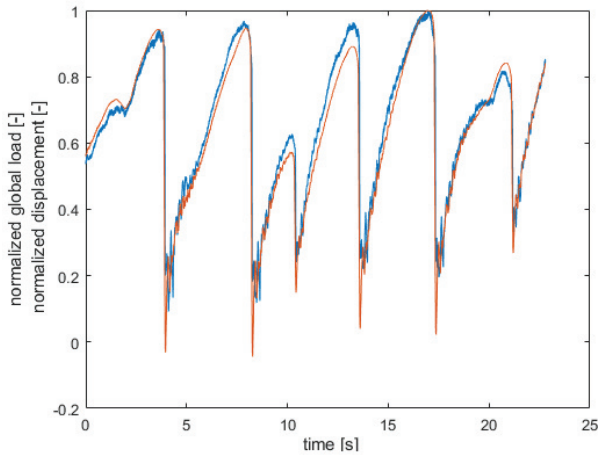

Figure 30: Normalized load (blue) and response (orange) time series of IC, v=5 mm/s

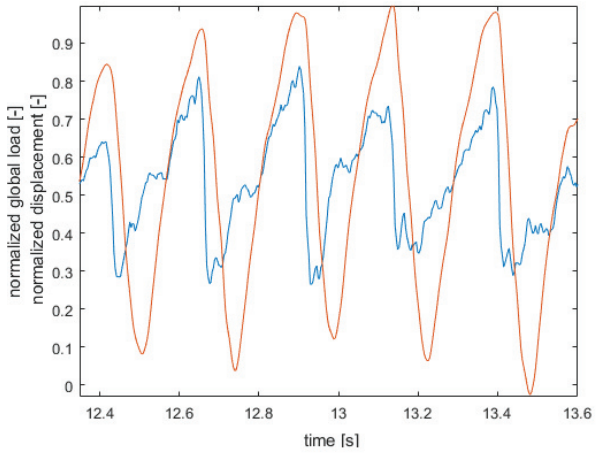

Figure 31: Normalized load (blue) and response (orange) time series of FLI, v=55 mm/s

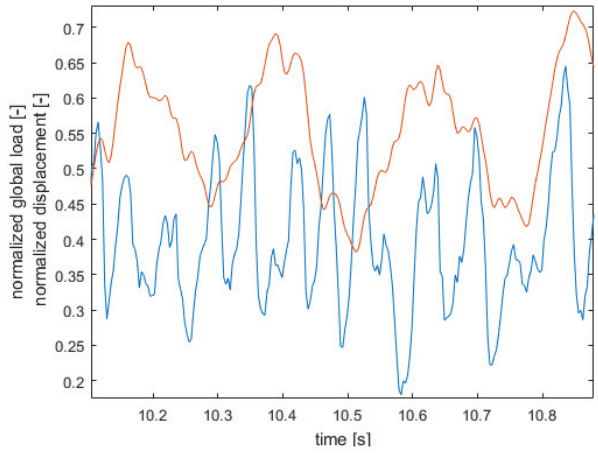

Figure 32: Normalized load (blue) and response (orange) time series of CC, v=150 mm/s

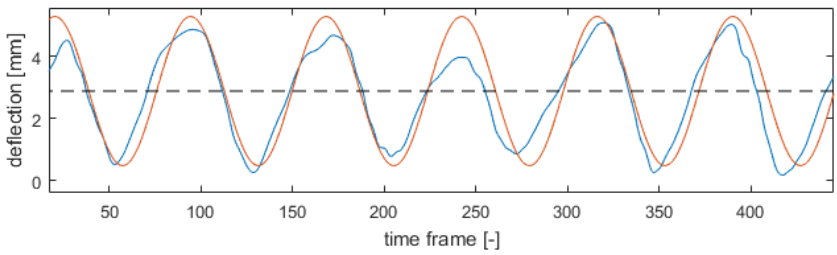

Figure 33: Comparison of FLI response to sine function

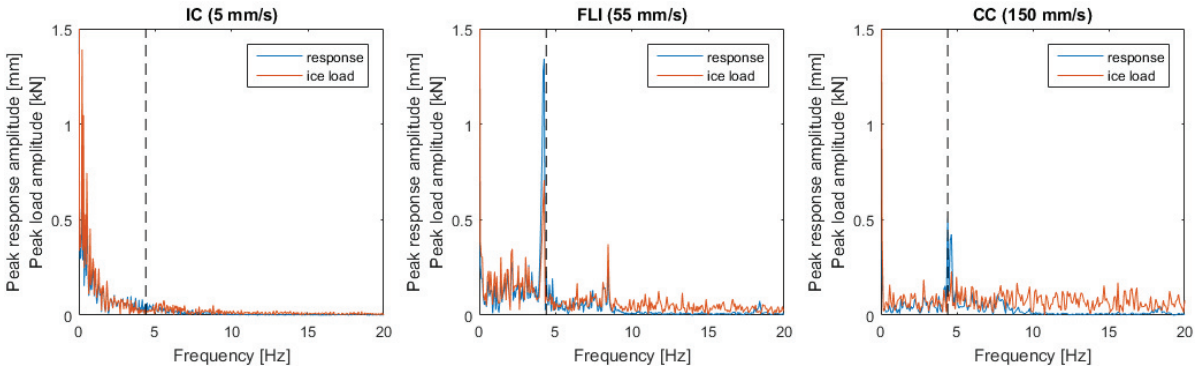

Figure 34: Load and response spectra for selected events representative for IC, FLI and CC (Run 32030)

for each loading cycle. The time interval of the IC cycles is therefore calculated by identifying the time instances when the global load drops below the mean load level of the entire event, representing the time instance of the global failure. The maximum load between two consecutive time instances of failure constitutes the peak load for the respective load cycle. To increase the comparability between the different events which have different durations, outliers among the peak values for each events are identified following Chauvenet's criterion and excluded from the presented mean load ratios.[13] Results for all velocities leading to the respective failure type within one test run are averaged. Only clear events with contact over the entire circumference or projected width are taken into account. Due to the small number of test runs, Chauvenet's criterion is applied again, based on Student t-distribution for small sample sizes. However, outliers were only excluded if the number of evaluated events per failure type was larger than three. A full overview including results from individual tests is given in App. C.1. The comparison illustrates that the average peak load values in FLI and IC are about the same. Also, the general mean load level as well as the average peak load level in FLI is about the same as in CC. However, the average peak load level in CC highly depends on the chosen minimum peak distance, and the presence of superimposed flexural fail-

[13] Chauvenet's criterion defines a data point as spurious if it occurs at a probability lower than $P \leq \frac{1}{2n}$ (n being number of samples). The probability is based on the assumption of a normal Gaussian Distribution.

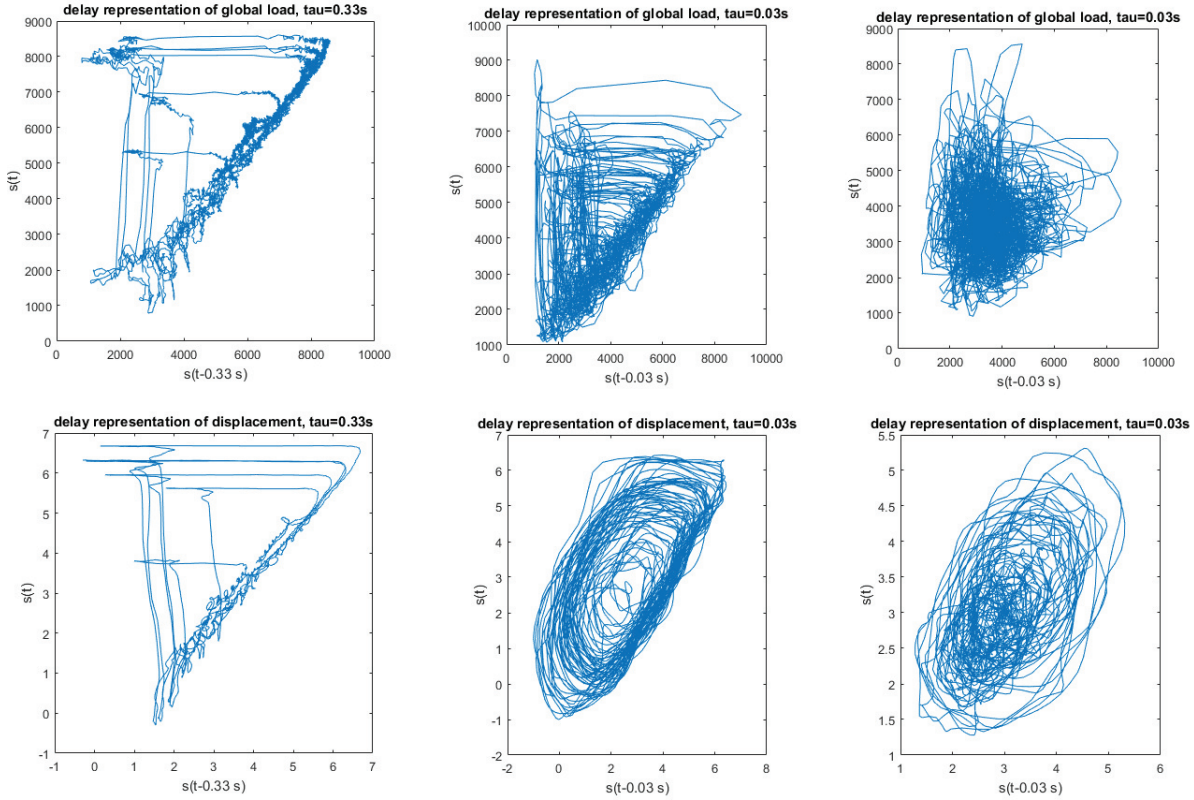

Figure 35: Delay representation of IC (v=5 mm/s, left), FLI (v=55 mm/s, center), and CC (v=150 mm/s, right). All from Run 32030.

ure and structure vibrations in the crushing interaction. Also, changing ice parameters during the test run aggravates the direct comparison. Exemplary time series illustrating the considered peak values are shown in Fig. 36.
Note that the provided mean values are only indicative as the individual events are weighted differently, depending on the number of velocities within one test run that led to the considered failure.

4.1.3. Development of contact area and local pressure

The tactile sensors show how the contact area develops during the different types of crushing. In this section, measurements obtained during Run 32030 are exemplarily investigated. Run 32030 was conducted with a 120 mm wide flat indenter, equipped with the detailed tactile sensor D. C1 configuration was used; ice properties are characterized by high thickness and strength. Due to the thick ice and low aspect ratio, the interaction was clear crushing with no superimposed bending. This test run was used as basis for the analysis because it contains high quality measurements of IC, FLI and CC within the same test run. The results were checked against all other test runs afterwards.

Run	21010	24010	25011	26010	26020	31030	32030	mean
shape	cyl	cyl	flat	corner-first	flat	flat	cyl	
D	500	120	200	283	200	120	120	
$\frac{\hat{F}_{\mathrm{FLI}}}{\hat{F}_{\mathrm{IC}}}$	1.26	-	-	0.97	-	-	1.05	1.09
$\frac{F_{\mathrm{FLI}}}{F_{\mathrm{CC}}}$	1.36	0.99	1.02	1.05	0.85	1.11	1.08	1.13
$\frac{\hat{F}_{\mathrm{FLI}}}{F_{\mathrm{FLI}}}$	1.45	1.45	1.68	1.33	1.58	1.34	1.55	1.48
$\frac{\hat{F}_{\mathrm{FLI}}}{\hat{F}_{\mathrm{CC}}}$	1.30	0.94	1.17	1.20	1.03	1.02	1.06	1.10

Table 8: Comparison of mean load ratios between different crushing types within the same test run. Only runs with full contact over the entire upstream circumference are considered. Configurations are described in Tab. 5.

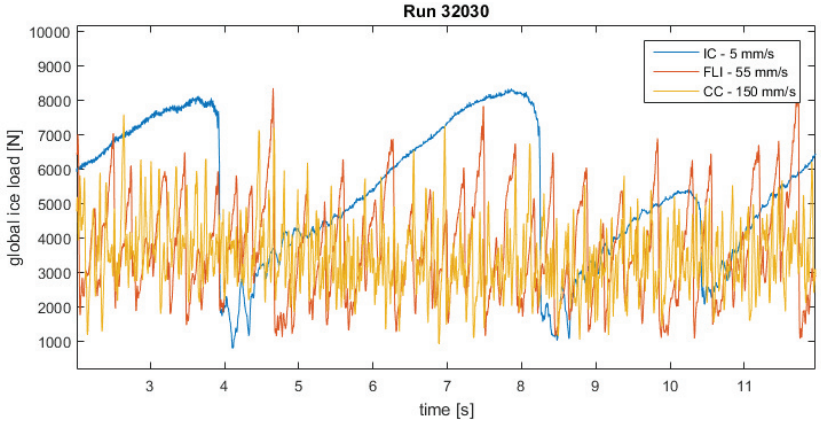

Figure 36: Exemplary time series of IC, FLI and CC; all taken from Run 32030.

First, general trends in area development are shown based on time series of selected events. Some exemplary time histories are presented in Fig. 37. Therein, contact is normalized by the nominal contact area of the specific test run[14], and global load is normalized by the maximum global load measured in the respective run, i.e. by the global load peak across all observed interaction regimes. In the presented example of IC and FLI, contact area grows along with the global load. The average area maxima in the respective IC event correspond to 37% of nominal contact, whereas FLI contact area peaks only reach 27% in the shown time interval, and maximum contact in CC is 20% based on averaged maxima. Hence, the actual contact differs significantly between the different crushing types. The time series of CC show that the percentage differences in load correspond well to differences in area. In IC, load increases more than area, hence area increase must involve additional pressure increase. The same accounts for FLI, although the difference in load and area increase is smaller. The observed area increase is quantified in Sec. 4.1.4.

A closer look at the contact area development reveals that most of the area increase in IC as well as in FLI originates from an increase in contact height, while only a small ratio is generated by closure of discontinuous contact over width. In the beginning of global load build-up, width and height increase simultaneously. When discontinuities have been closed, only height grows. Figure 38 shows exemplary snapshots from tactile measurements at global load minima and maxima during different crushing types. The snapshots illustrate the largest contact variation in IC, accompanied by a large share of high pressure across the contact. The average maximum contact height recorded in Run 32030 during the example of FLI (30.1 mm) is about the same as in the presented event of IC (30.5 mm). For comparison, the maximum height found in CC from the same run amounts to only 23.6 mm.
It should be noted that the mean contact height is affected by the choice of threshold during tactile post-processing to exclude rubble contact. Hence, the height of contact area covered with high pressure zones is chosen as a more comparable value, which is investigated in Sec. 4.1.4.
The difference in contact height is only captured by Sensor D, because Sensor L's spatial resolution is insufficient. On Sensor L, the load increase is reflected in closure of contact discontinuities, and simultaneous pressure increase.
The maximum local pressure is on the same level in all crushing scenarios within the same test run. More information on local pressures is given in App. C.1.

Figures 39 to 41 illustrate the combined effects of area and pressure development. Therein, the trend of actual pressure normalized by the maximum actual (global) pressure is shown, next to the normalized global load and the ratio of actual and nominal contact area.
The time history of IC shows rather static actual pressure except for the phases of failure and contact re-establishment, and growing contact area resulting in almost periodic ice

[14]Nominal contact area is defined by mean ice thickness h_{ice} times projected indenter width W.

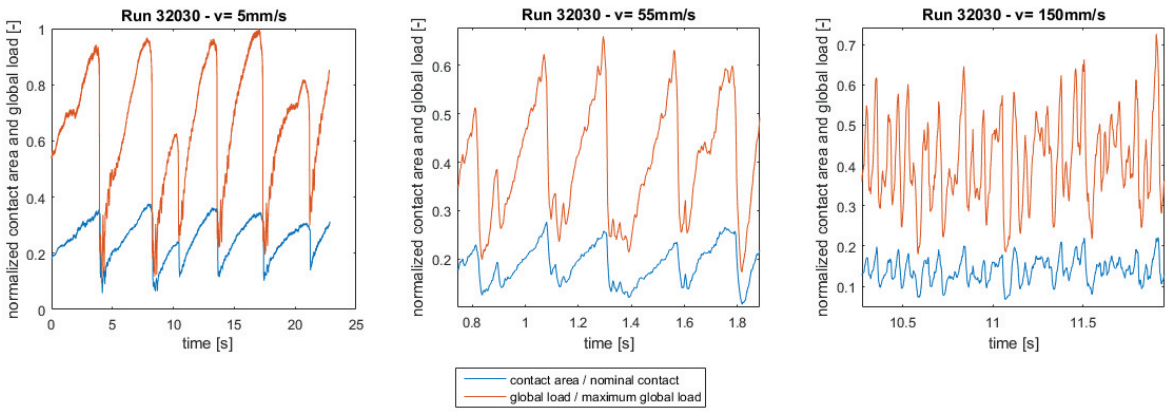

Figure 37: Normalized contact area and global ice load in ice drift direction for IC (left), FLI (center), and CC (right). Examples taken from sensor D during Run 32030 with flat indenter and high aspect ratio.

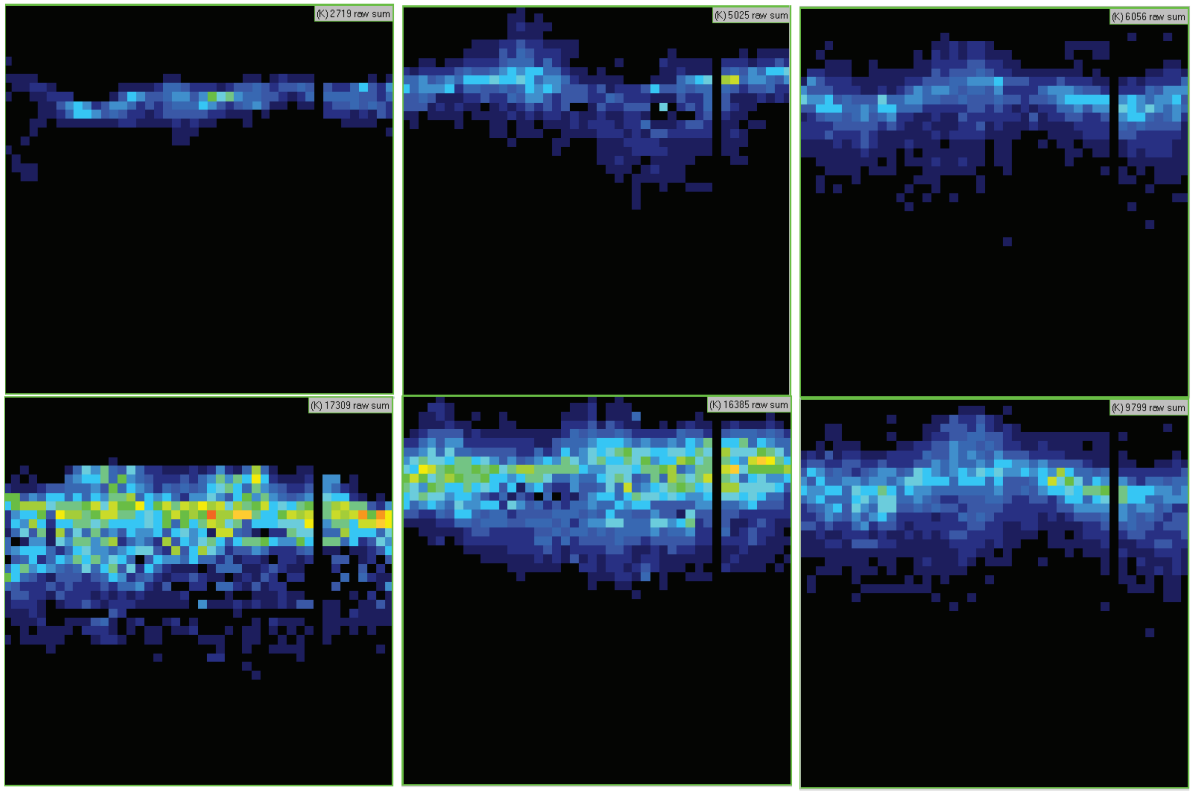

Figure 38: Snapshots from tactile measurements during IC (left), FLI (center) and CC (right); contact at representative minimum global load (top) and maximum global load (bottom). Snapshots show uncalibrated raw data from Run 32030.

load. In FLI both, actual pressure and contact area, grow along with the ice load during each cycle.

Results for all tested velocities from Run 32030 are compiled in Fig. 42. The plot illustrates the larger area variation amplitudes in IC and a tendency of decreasing amplitudes over increasing ice drift speed in IC regime. Despite some scatter, the maximum contact area developing during FLI is rather constant over the entire FLI regime, and drops towards CC. Data from other test runs shows that the area is quite constant over the CC regime; however, clear CC without mixed mode interaction has been rarely observed, thus no distinct trends can be derived from the data for this regime.

Above considerations indicate that the increase in total load during FLI cycles results from a combination of significant area increase and simultaneous increase of pressure across the interaction area. The same accounts for IC; however, the pressure increase occurs rather instantaneously when contact re-establishes after global failure, and the pressure level remains almost constant while the contact area grows in height. In CC, pressure and area can increase independently. Generally, the variation in contact area is small in this type of crushing. FLI shows characteristics from both, IC and CC, regimes. The local pressure maxima are the same for all crushing types.
Above described qualitative trends are investigated with reference to the corresponding behaviour of high pressure zones in the following.

4.1.4. Development of high pressure zones

High Pressure Zones (HPZ) are deemed decisive for the transport of ice load during continuous crushing (comp. Sec. 2.2.3). According to Richard and Taylor, HPZ carry 80% of the total load on about 10% of the nominal contact area [86]. Fig. 43 shows how the global load is distributed over the contact area in Run 32030. The depicted lines were calculated by applying different threshold values in steps of 10%. An area fraction of 100% refers to the entire loaded area, thus the number of sensels which show non-zero pressure, summed up for all time steps within the respective event. The ratio of load on 100% of the loaded area equals the total load. Next, the considered area is stepwise reduced by sorting all measured local loads, and clipping them at the vector length representing the area fraction to be considered. Division of the load acting on the considered area by the total load (without clipping) delivers the load ratio plotted on the y-axis in Fig. 43. The same is done for all other considered area fraction values, and results are interpolated to obtain the complete trend. It should be noted that for IC and FLI, this procedure is less expressive than for CC, and the different phases of FLI and IC are averaged. This procedure shall define a clear threshold value to identify HPZ. Averaging all signals ensures consistent treatment of measurements from all interaction regimes.

In IC, on average 62% of the actual contact area carry 80% of the global load. In FLI, the fraction increases to 64%, and it amounts to 69% in CC. Related to the nominal

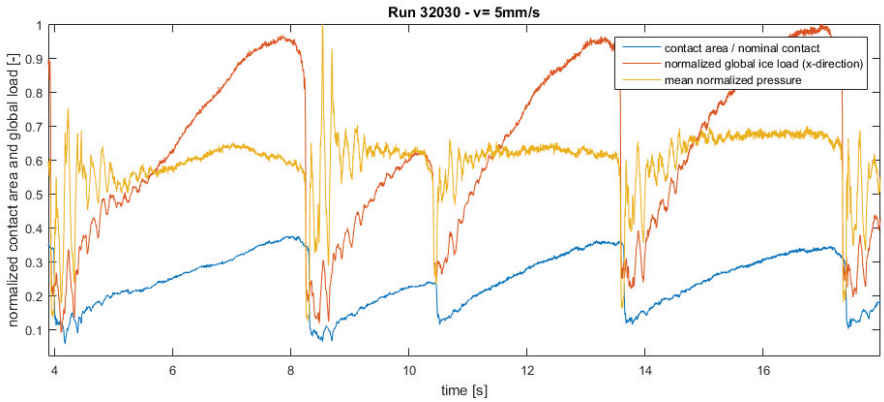

Figure 39: Development of global load, contact area and mean pressure during intermittent crushing (Run 32030, v=5 mm/s)

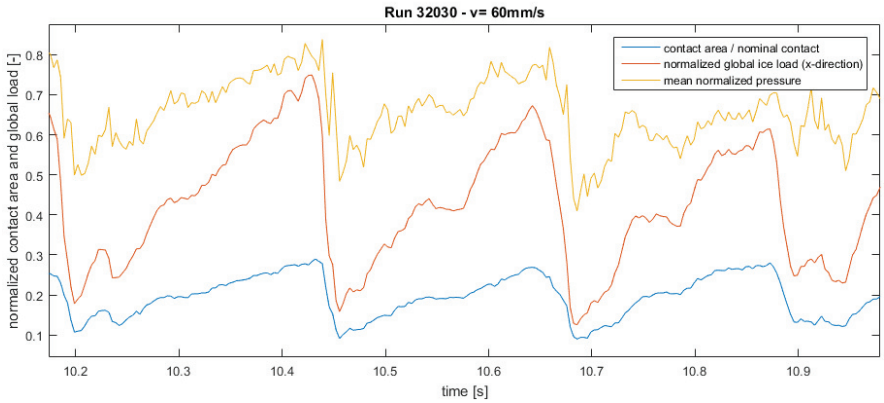

Figure 40: Development of global load, contact area and mean pressure during frequency lock-in (Run 32030, v=55 mm/s)

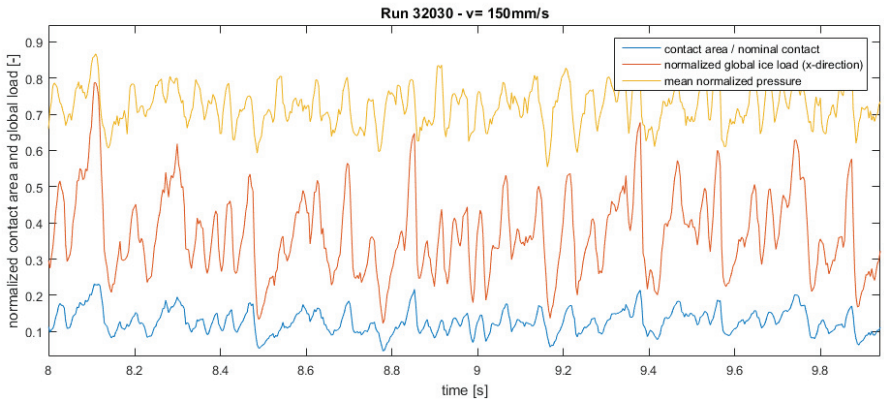

Figure 41: Development of global load, contact area and mean pressure during continuous crushing (Run 32030, v=150 mm/s)

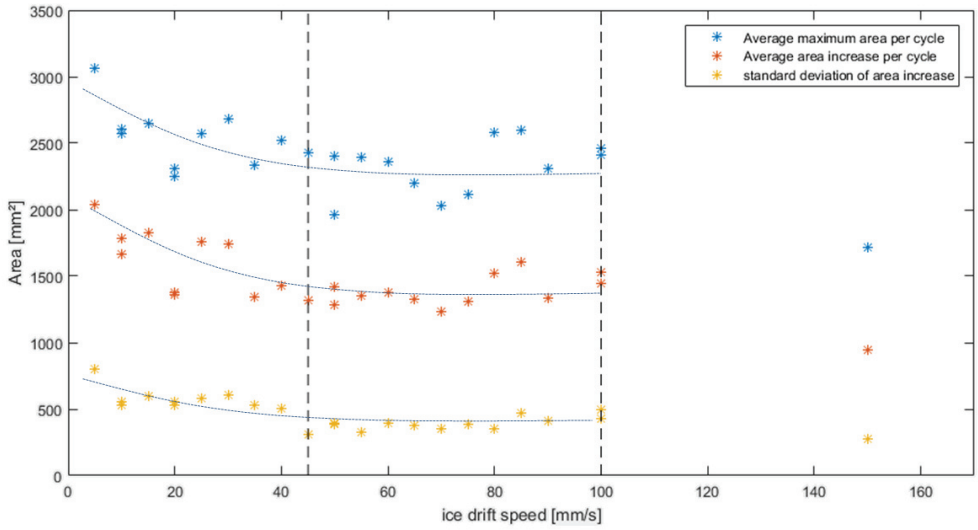

Figure 42: Contact area variation for all tested ice drift speeds in Run 32030. FLI interval is marked with dashed lines. Dotted lines indicate decreasing trend of peak contact area over increasing ice drift speed in IC regime.

contact area, these values correspond to 23% in IC, 17% in FLI, and 11% in CC. It can be noted here that the share of HPZ in continuous crushing of model ice in this respective test is in line with measurements of sea ice crushing (compare Sec. 2.2.3).
A threshold pressure of 2 MPa is universally chosen for the identification of HPZ on Sensor D in the presented study. In the analysed data, the low-pressure areas are removed for the following assessment of HPZ characteristics.

High pressure zones are analysed regarding their evolution in time. First, only development of pressure around the circumference of the structure is assessed. The pressures in HPZ are therefore integrated over the sensor height for each column. Hence, horizontal spatial resolution is preserved, but vertical resolution is omitted. This is relevant for the interpretation of the results, as the previously shown increase of contact in height is not included. If the shown *ratio of contact area* equals one, it means that the entire width of the structure's circumference is covered with HPZ in the respective mode. However, contact can still develop over height, which is further investigated at a later point in this section.
For each time step, it is evaluated which ratio of the actual contact in width is covered by HPZ which are currently increasing in pressure (fraction of contact in build-up), and which by HPZ that are failing (fraction of contact in failure), identified by decreasing pressure. Only the difference to the preceding time step is taken into account. If the pressure level remains the same as in the previous time step, the respective area occurs in none of the two categories. But due to the high pressure resolution and negligence of low pressure areas, this hardly occurs. Note that this definition also counts HPZ as *failing* which are temporarily being unloaded due to movement of the structure in

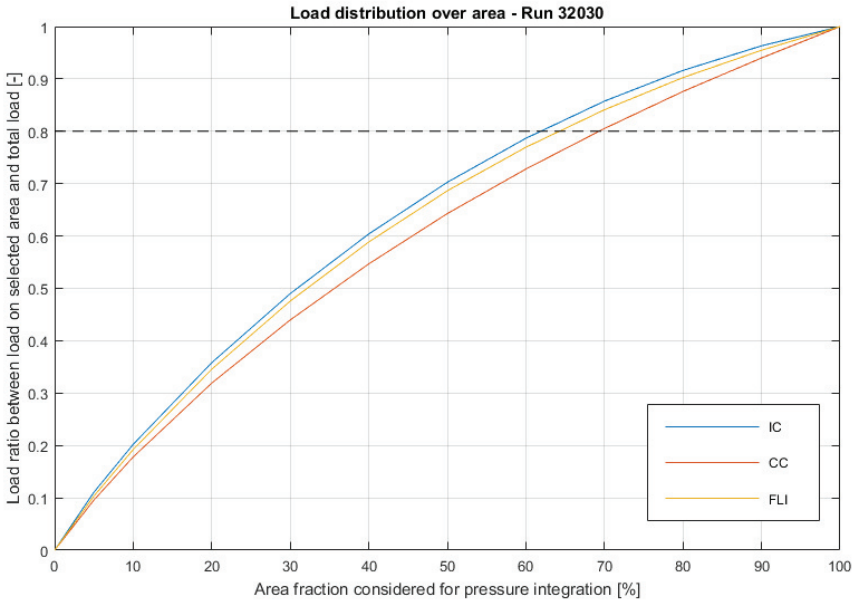

Figure 43: Illustration which percentage of the active area carries which fraction of the total load (averaged), based on Run 32030. 80% load level is marked by dashed line.

ice-drift direction. Results are shown in Fig. 44 for Run 32030: Again, it is evident that the load increase in IC largely stems from increasing contact. There is almost full failure of the contact width after each global load peak. The ratio of HPZ in failure gradually decreases as the global load increases. There is a short period without local failure just before the global load peak is reached.
In FLI, only parts of the contact fail in each recorded time step. The number of failing HPZ over width indicates a chain reaction rather than instantaneous failure, as more than 50% of the contact width remain in (or enter) build-up while the global load drops. During a short time of about a quarter FLI oscillation period, a considerable number of HPZ is unloading. After that phase, there is a global failure stop which lasts for the remaining three quarters of the oscillation period. At the same time, pressure increases simultaneously in all HPZ across the structure's interaction area.[15]
Failure and build-up naturally follow opposite trends also in CC, and build-up slightly correlates with the global load, but neither full failure nor significant simultaneous build-up is visible.

The average fraction of contact width in simultaneous build-up is calculated for all FLI events. If more than one FLI event has occurred in the respective test run, results from all events are averaged. The ratio of simultaneousness in build-up during FLI ranges

[15] Note that this simultaneous pressure increase is, as described earlier, actually composed of local pressure increase and parallel increase of contact area, which amplifies the apparent pressure increase in the column-integrated representation.

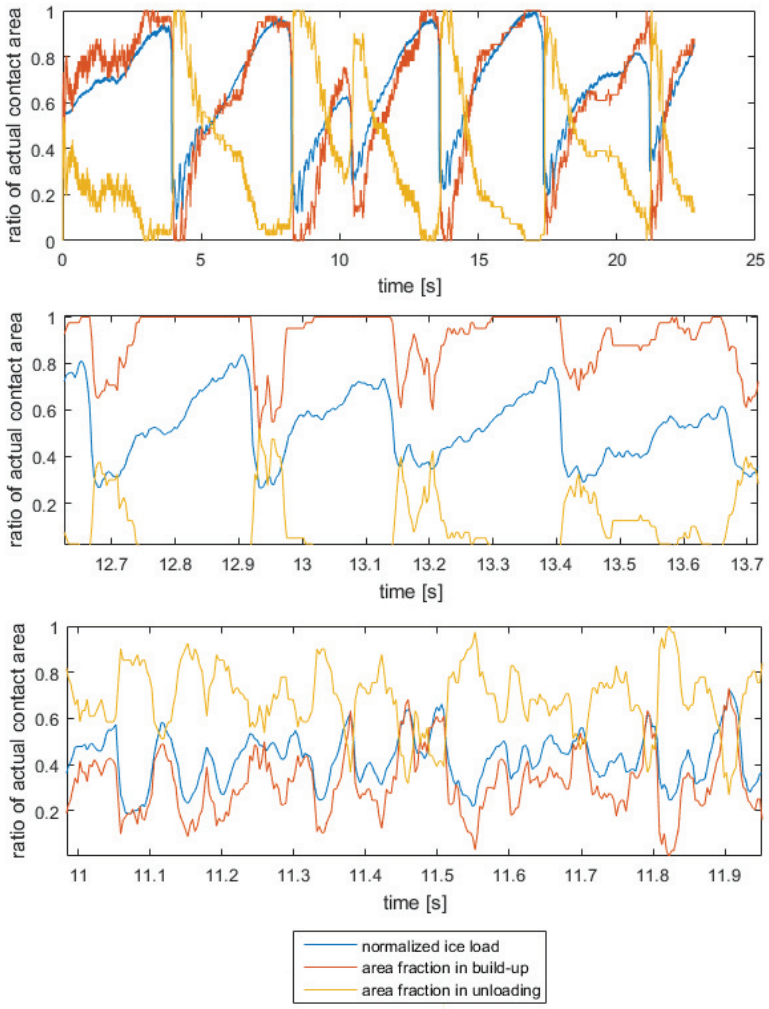

Figure 44: Ratio of actual contact width covered with HPZ in build-up and failure during IC (top), FLI (center) and CC (bottom).

from 0.768 (Run 25011, 200 mm flat indenter) to 0.999 (Run 21010, 500 mm cylinder). Mean values are generally lower for a flat indenter than for cylinders, and increase with increasing cylinder diameter. However, the highest peak in area fraction is 1.0 for almost all test runs, and the difference of average peak values between the individual runs of the same test type is marginal and insufficient to deduct general trends. Values are compiled in Tab. 9.

The increase in height during IC and FLI described above is only visible on Sensor D, hence only on a limited area around the center line of the structure. However, it has been shown that the simultaneous pressure build-up is a global phenomenon, as it covers the entire (or almost entire) interaction width.

The increasing contact area visible on Sensor D comes along with growth of the high

Run	shape	width	maximum area fraction in simultaneous build-up during FLI	average area fraction in simultaneous build-up during FLI
21010	cylinder	500 mm	1	0.999
23010	cylinder	200 mm	1	0.994
24010	cylinder	120 mm	1	0.840
25010	flat indenter	200 mm	1	0.768
26010	corner-first	283 mm	1	0.866
26020	flat indenter	200 mm	0.993	0.772
31030	cylinder	120 mm	1	0.979
32030	flat indenter	120 mm	1	0.823

Table 9: Fraction of contact width in simultaneous build-up during FLI (averaged over all FLI events within the same test run; for number of evaluated events see Tab. 6)

pressure zones, which cover large portions of the actual contact. The average maximum contact height covered by HPZ ($\hat{h}$) is calculated for Runs 31030 and 32030, and presented in Tab. 10. $\hat{h}$ is defined from the N peaks of HPZ contact area $\hat{A}_n$, automatically identified from the HPZ load time series using a minimum peak distance of 0.95 times natural oscillation period, multiplied by the sampling rate:

$$\hat{h} = \frac{\sum_{n=1}^{N} \hat{A}_n}{N \cdot CQ \cdot CW} \tag{11}$$

Equation 11 shows that the calculated mean maximum HPZ contact height refers to a uniform contact over the sensor width[16] and uniform height. Test runs with high aspect ratios, where the interaction mainly occurred with the top layer and the HPZ did not form in the same way as observed in thicker ice, have been excluded from this assessment.
The comparison reveals that the increase of contact described earlier is indeed an effect of increasing HPZ, which grow in height approximately by factor 1.5.

4.2. Characterization of frequency lock-in

The previous analysis has revealed general characteristics of FLI in comparison to other crushing regimes. This section concentrates on FLI and some of its characteristic features previously used for failure type identification.

[16] Measures CQ and CW, being column quantity and column width.

Run	W [mm]	h_{ice}	$\hat{h}_{\text{FLI}}$ [mm]	$\hat{h}_{\text{CC}}$ [mm]	$\frac{\hat{h}_{\text{FLI}}}{\hat{h}_{\text{CC}}}$ [-]	$\frac{\hat{h}_{\text{CC}}}{h_{\text{ice}}}$ [-]
31030	120	41	13.3	7.0	1.58	0.29
32030	120	70	36.5	24.0	1.52	0.34

Table 10: Average peak height of high pressure zones in FLI and CC events; mean values averaged over all events of the respective interaction regime within the same test run. Only test runs with full interaction area coverage with Sensor D taken into account.

4.2.1. Assessment of FLI criteria

The criteria gathered in Sec. 2.3.1 were calculated for the identification of FLI events. Their trends are briefly discussed below.

Frequency similitude
Once in FLI regime, the structure oscillates in a frequency close to its natural frequency in open water. Fig. 45 shows a constant frequency ratio over the entire FLI range. The example is taken from Run 25010, but is representative for the FLI regimes of all tests. However, the dominant frequency in CC in the presented test is lower than in FLI, but can also be higher (comp. Fig. 34), so no general trend should be deducted from these examples. Added mass and damping effects from the ice are deemed decisive here.
The trend of frequency ratio over cylinder diameter is also illustrated in Fig. 45. It indicates a decreasing trend of dominant oscillation frequency over diameter. This can be related to the increasing amount of crushed ice resulting from the interaction with larger cylindrical structures that adds to the damping, which decreases the oscillation frequency. Note that the trend partially bases on results with the 830 mm model from Phase 1 tests with the submerged compliant basis, hence different added mass effects.
If clear IC regime develops at low ice drift speed, the dominant loading frequency increases gradually with increasing ice drift speed until transition to FLI. An exemplary spectrogram of load and response over IC and FLI regime is shown together with the respective time histories in Fig. 48.

β-ratio
Ratio β is calculated for each tested velocity and exemplarily plotted for run 26020 in Fig. 46 (right). The trend of β over ice drift speed can be quite different. However, comparison of all test runs shows also consistent trends: The mean oscillation velocity grows in FLI regime as the ice drift speed increases. Typically, the β-ratio is high at the beginning of FLI regime, remains constant over some velocities, and then slowly decreases until the interaction falls out of the defined β-range. Histogram of all calculated β-values is given in Fig. 46 (left).

γ-ratio
The ratio γ is a measure for the steadiness of the response. In transition events, γ is

typically the first value to exceed the FLI range (threshold $\gamma = 0.2$), while the dominant frequency of response and the mean ratio β often remain longer in FLI range. A histogram of calculated γ-values is given in Fig. 47 (right). It shows that the majority of events has significantly higher steadiness than required to fulfil stipulated FLI criteria.

Dynamic amplification
The Dynamic Amplification Factor DAF is calculated for each FLI event by dividing the respective global ice load of each displacement peak by the structure's stiffness at waterline. This value represents a theoretical response to a static ice force. Averaging the ratio of actual and static response over the entire FLI event yields the respective average DAF. Fig. 47 (left) gives an overview of typical DAF found in the presented study.

The trends of the three criteria over ice velocity are shown for two test runs in Fig. 49. Therein, the left plot refers to a flat indenter and the right plot to a cylindrical structure, both having a diameter of 120 mm. Direct comparability is reduced by a difference in ice thickness of factor 1.6. A consistent trend among the different data sets is the increasing DAF over the FLI range, and decreasing β towards the transition from FLI to CC and beyond. However, the data is scattered and highly influenced by individual conditions for each test run. All values are compiled in App. C.1.

4.2.2. Phases enabling the lock-in cycle

Analysis of the measured data indicates that the lock-in cycle can be subdivided into two phases based on the local pressure characteristics:

1. **Global build-up phase**: Global build-up is characterized by complete failure stop (number of contact loss is zero), a high ratio of contact elements in simultaneous pressure increase, and an increasing number of HPZ which increase in their vertical extent.

2. **Local crushing phase**: The local crushing phase has different parts: First, the number of elements with decreasing pressure increases and the global ice load drastically decreases. At the same time, the number of elements in global build-up reduces and the number of failing elements reaches its maximum. As the number of failing elements decreases again, the global load increases.

The condition for the interaction to conclude Phase 1 and enter Phase 2 is local exceedance of the ice strength, resulting in local failure which rapidly spreads over the entire contact area. The condition to enter Phase 1 is crucial for the onset of FLI vibrations. It requires a complete failure stop resulting from negative relative velocity between ice and structure, leading to a short phase of unloading before the pressure increases simultaneously in all existing HPZ when the relative velocity becomes again positive.
This mechanism is illustrated by a force-velocity curve in Fig. 50. Assuming that the condition for failure stop is met, the interaction starts at point **1** in the curve. Ice load

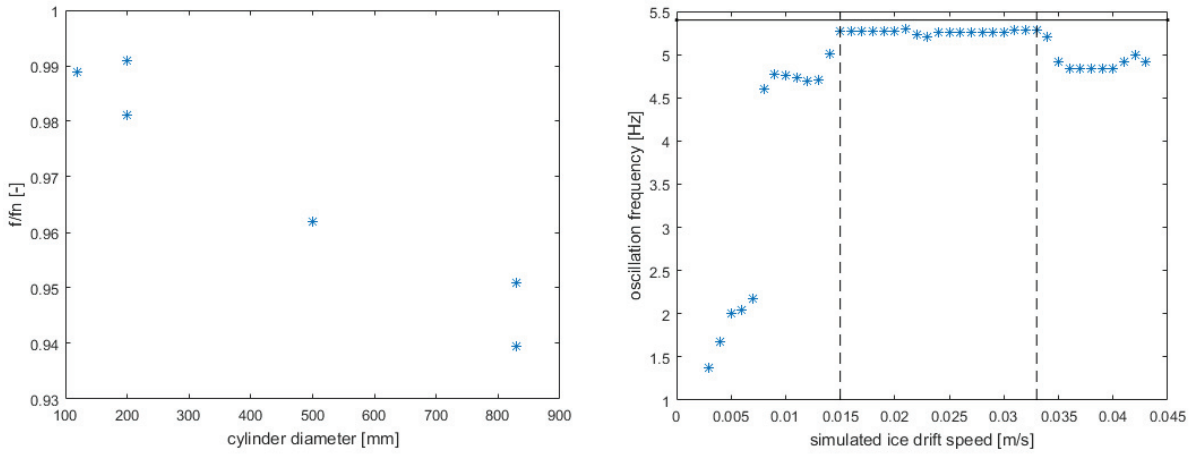

Figure 45: Exemplary trend of oscillation frequency, expressed as fraction of natural frequency (without presence of ice), vs. cylinder diameter (left); Trend of oscillation frequency over ice drift speed (right, Run 25010)

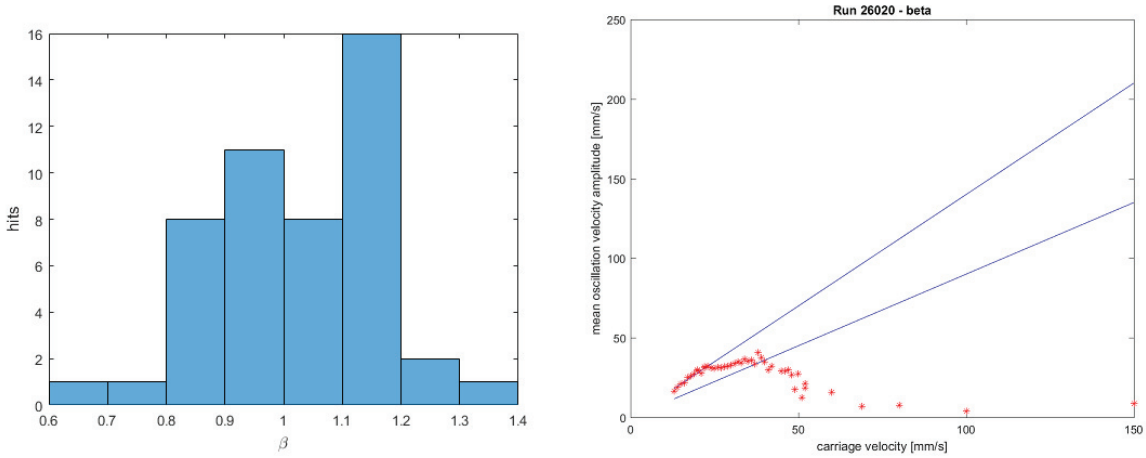

Figure 46: Values for β-ratio. Left: histogram for all FLI events; right: Values for each velocity tested in Run 26020. Blue lines indicate boundaries of 0.9 and 1.4.

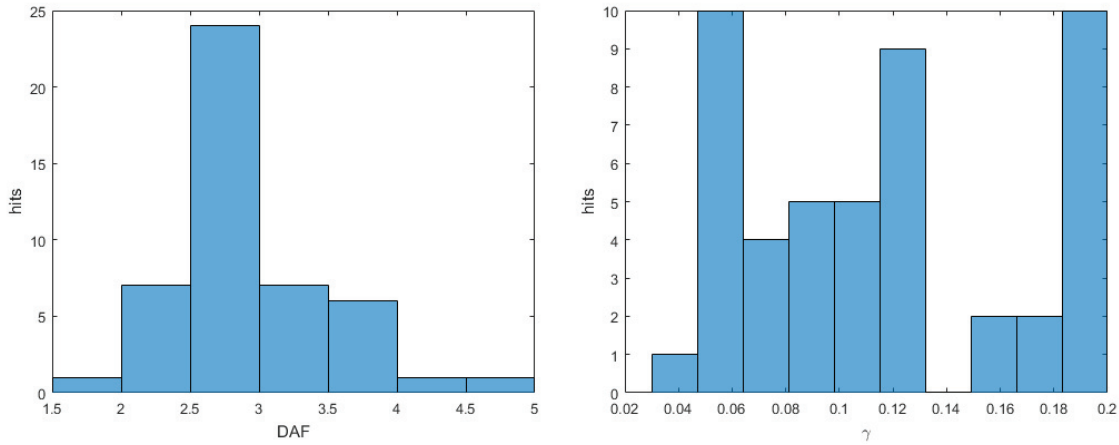

Figure 47: Histogram plots for DAF and γ-ratio distribution (all clear FLI events, no transition)

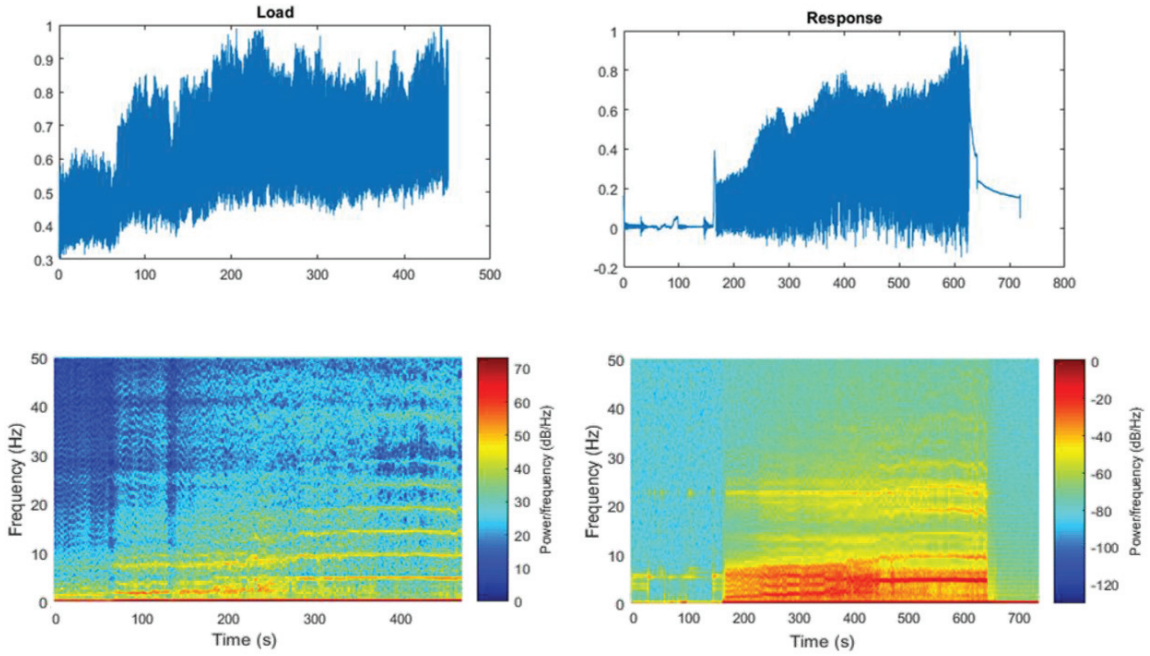

Figure 48: Spectrogram of load and response measured during Run 26020

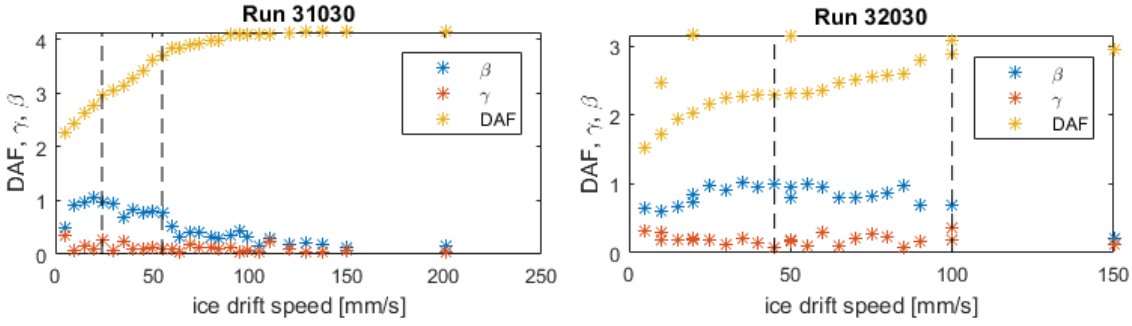

Figure 49: DAF, γ and β calculated for all tested velocities in Run 31030 and 32030. Dashed lines mark FLI range.

gradually increases while the relative velocity between structure and ice increases. At point **2**, local loads exceed the bearing capacity of the ice, and ice begins to fail locally. After initial failure of first parts of the ice, others are rapidly loaded, and also fail. This chain-reaction failure happens almost instantly, resulting in the load drop from point **2** to point **3**. Structure and ice then interact in continuous crushing, characterized by the rather constant load level prevailing until the relative velocity becomes again small enough to initiate the failure stop and start another global build-up phase. After the failure stop, all HPZ align in phase as they simultaneously start to increase size and pressure.
Fig. 51 shows the force-velocity curves for FLI events at different speeds, where basically the same characteristic can be found. In comparison, the curve for CC shows that force and relative velocity remain about the same during a time interval with the same duration as plotted for the FLI events. The crushing load level equals the mean load during FLI crushing phase at the same relative velocity.
The cycle illustrates that FLI can only develop if point **1** is reached. If the ice speed is too high, the interaction remains in the higher relative velocity range, and the nonlinear behaviour cannot develop. If the ice speed is too low, the load increases without increasing relative velocity, thus the interaction remains in the linear regime.

Figure 52 shows the local qualitative pressure registered by the tactile sensor (D) during FLI on a flat indenter in Run 32030. The global pressure increase between start and end of global build-up phase is clearly shown. The contact primarily increases in height after the relative velocity between structure and ice has been negative and became positive again. Afterwards, the entire contact area participates in global build-up, and no local failure occurs. Hence, the global pressure increases, and due to the enlarged contact area, higher ice load can be transferred from ice to structure without increased local strength. Local crushing is initiated by termination of global build-up due to local exceedance of ice strength. This coincides with increased momentum from the structure that has passed its oscillation amplitude and starts moving back to its equilibrium position, i.e. into the direction of approaching ice. During crushing, the contact drastically decreases in width and height. Spalls extruded downwards can be seen on the lower part of the sensor. The contact becomes discontinuous. Measurements clearly show that the local crushing process is a chain reaction, and no simultaneous failure across the entire contact area takes place. As the potential energy of the deflected structure is initially higher than the work needed to crush the ice, the structure first moves almost unhindered through the approaching ice sheet, and is then slowed down[17]. While structure and ice have almost the same speed or shortly move in opposite directions away from each other, a complete failure stop and subsequent simultaneous load build-up in all HPZ occur.
The average and absolute minimum relative velocities during all FLI cycles is calculated for each event and plotted in a histogram in Fig. 53. The absolute minimum velocity is negative in all tests of the presented campaign. However, positive mean values exist as

[17] Compare also reference to the free oscillation case, Fig. 33.

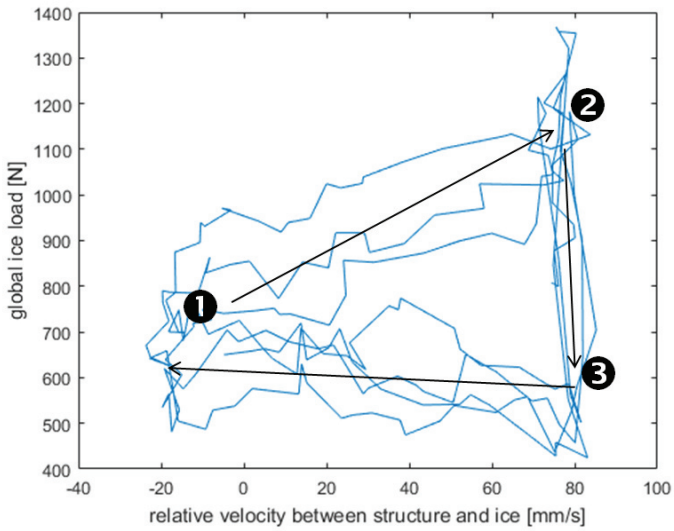

Figure 50: Force vs. relative velocity for three consecutive cycles of FLI (Run 26020). (1) Start of global build-up phase, (2) Begin of local crushing, (3) Continuous crushing until end of cycle

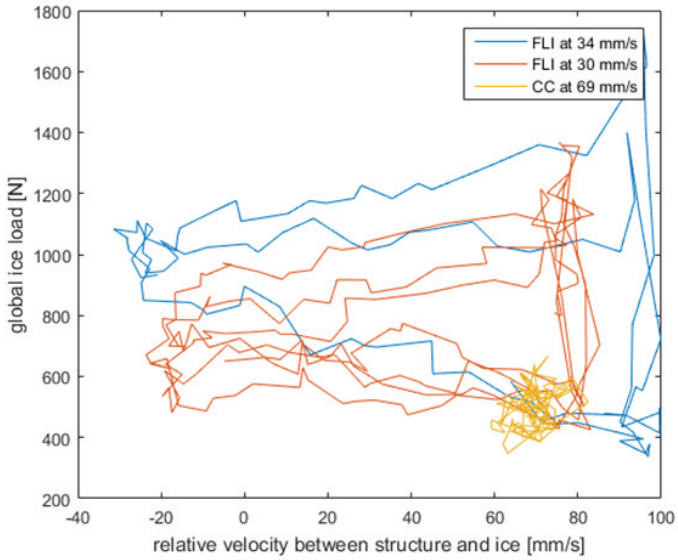

Figure 51: Force vs. relative velocity for different ice drift speeds in FLI and CC (Run 26020)

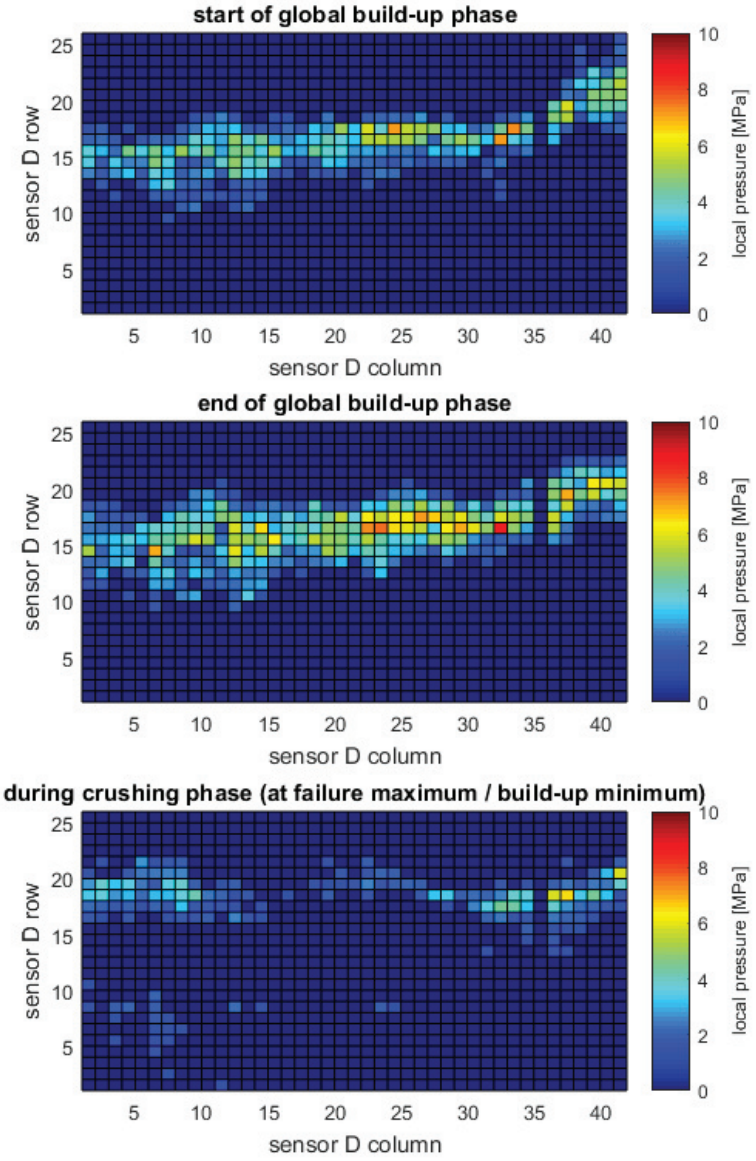

Figure 52: Local qualitative pressure at start of build-up (top), end of build-up (center) and during crushing phase (bottom) measured on Sensor D in Run 32030.

well, indicating that very low relative speed is sufficient for the failure to stop.

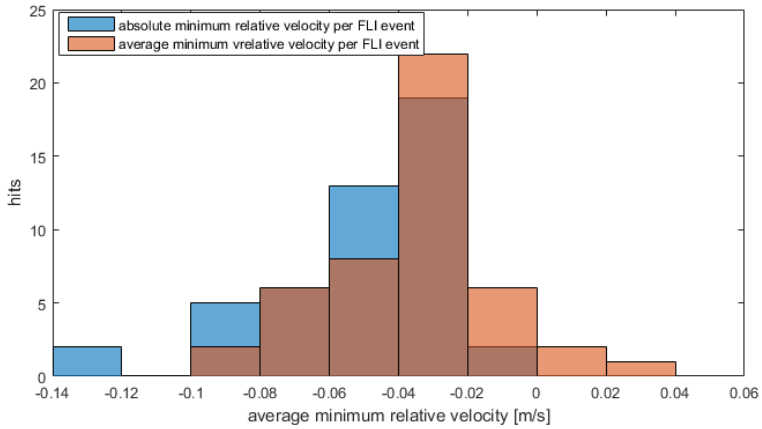

Figure 53: Histogram of minimum relative velocity between ice and structure during FLI oscillations

A significant finding is that the necessary condition of (almost) zero relative velocity has to be met for each cycle anew. This circumstance is further illustrated in Fig. 54. For this consideration, the column-integrated pressure data is used. For each peak identified in the FLI event, each column is checked for its participation in the global build-up and subsequent failure. Build-up participation is separated into two categories: Collective load increase (yellow), meaning that the integrated pressure of the respective column has increased at the time instance of the peak compared to the start of the build-up phase, and continuous build-up (green), meaning that the local pressure has continuously increased over the build-up phase. Then, it is checked whether the pressure in the respective sensor column has dropped to zero during the global crushing phase following the global peak. The corresponding plots do not show any patterns. The participation of a column in the previous peak, representing the load build-up, does not seem to have a significant influence on the next one. This observations matches the described mechanism well. The occurrence of the failure stop is decided anew for each individual cycle. The previous cycles are in that respect decisive that they are needed to maintain the vibration and enable the amplified interaction. However, the local contact area development is completely unrelated to the previous cycle, as each global crushing phase resets the ice contact area.

4.3. Discussion

The analysis of FLI observed in the presented test campaign has shown clear characteristics of HPZ behaviour enabling FLI to develop. A significant increase of HPZ height subsequent to a full failure stop at zero or low relative velocity in low frequent (>10 Hz) FLI vibrations has been measured and quantified for the first time. It has been shown

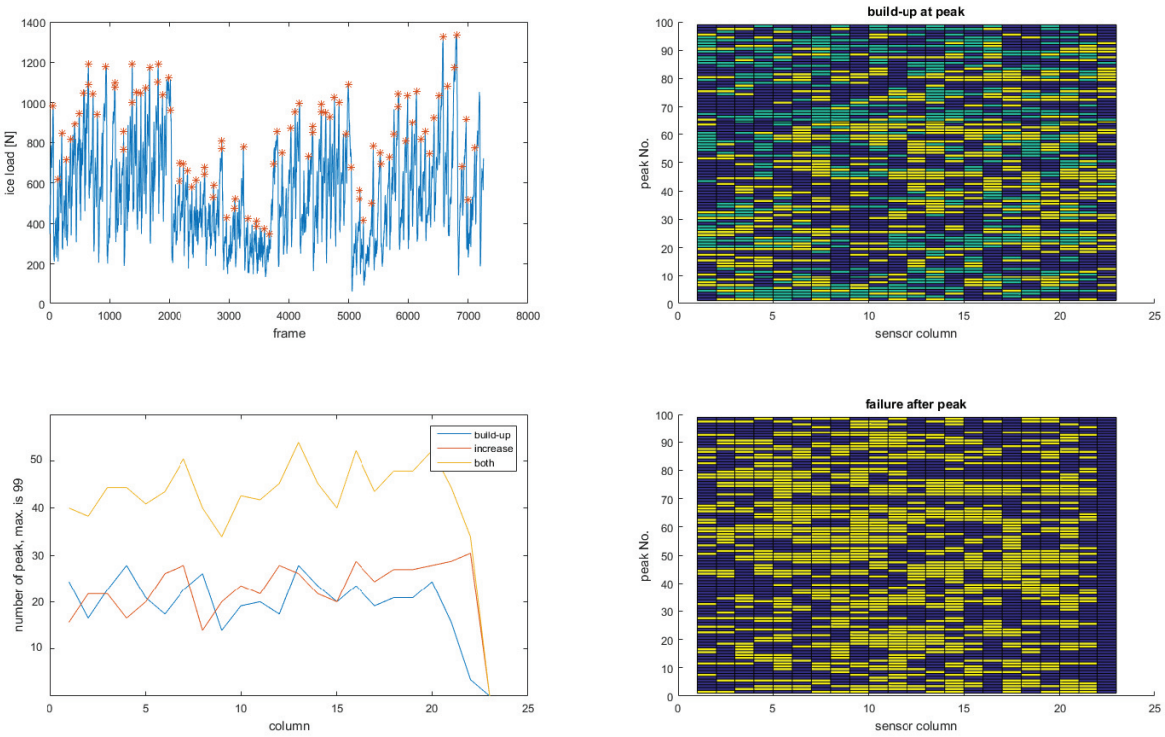

Figure 54: Top, left: identified peaks during lock-in event (Run 25010); Bottom, left: number of peaks followed by each sensel column; Top, right: Sensor columns involved in collective load increase (green) and collective continuous build-up (yellow) for each identified peak; Bottom, right: Sensel columns which lose contact after subsequent crushing

that a phase-adjustment due to the simultaneous failure stop in connection with the increased HPZ area allows transfer of higher ice load from the ice to the structure.
The significance of these findings for full scale applications is checked by comparison of the model test results to available full scale data. Afterwards, the results of the experimental test campaign are briefly discussed with respect to the currently available theories on the physical mechanism of FLI.

4.3.1. Comparison to full scale data

A fundamental question concerning the derived characteristics of FLI is whether the same phenomena are the decisive factors in full scale interaction of vertical offshore structures with sea ice. Unfortunately, the question cannot be conclusively answered as there is no data which provides the same insight into local pressure and contact area development as the model tests. However, full scale data is briefly checked to see whether general observations agree to the found relations, or whether contradicting observations have been made.
Full scale data used for comparison are measurements from lighthouse Norströmsgrund

(NSG, briefly introduced in Sec. 2.3.2), obtained during the STRICE project [4]. The lighthouse has been equipped with nine force measuring panels with dimensions of 1.2 m × 1.6 m each, covering 167° of the structure's circumference at water level. Due to the insufficient spatial resolution of the load measurement system at NSG lighthouse, it is not possible to evaluate the increase in contact height and full failure stop with the full scale data. However, the time series of model test and prototype structure show the same characteristics (Fig. 55), with a force plateau preceding the global build-up phase, and a build-up duration of about a quarter period. The figure shows results from Phase 1 tests (12050) where the same aspect ratio as found at NSG lighthouse was tested (D/h = 17).

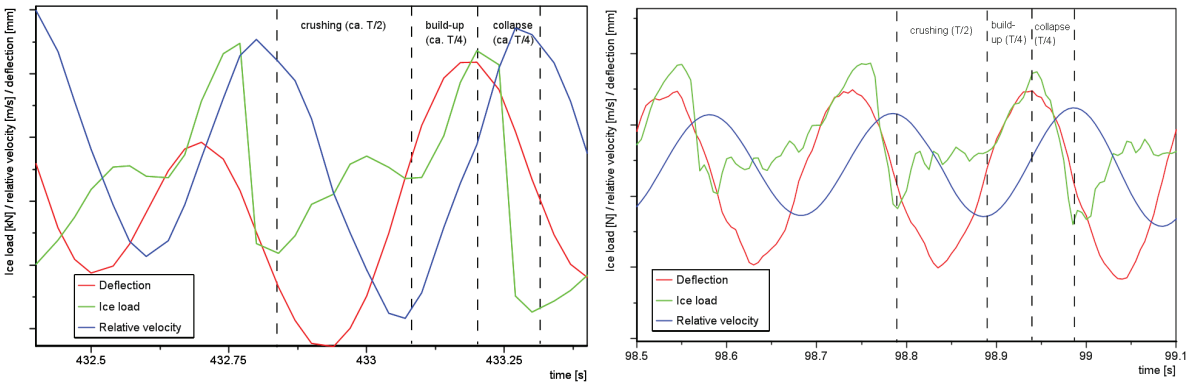

Figure 55: Normalized ice load, structure deflection at water level and relative velocity between structure and ice, measured at NSG lighthouse (STRICE event 1904-040, left) and during IVOS campaign (Run 12050, right)

When data from NSG lighthouse is shown in literature, it often appears as if the loads across the interaction area were highly correlated [63]. But looking at the tactile sensors, it was impossible to find sensels which remain synchronized, or correlated, over more than one cycle. The individual loads on 150 discrete areas (DA), each DA representing one tactile sensor column of Sensor L, are shown in Fig. 56c). They can be categorized in four main groups of sawtooth-shaped loads, plateau-shaped loads, sensels only participating in the chain-reaction collapse phase (characterized by steep load increase and subsequent complete load loss during the global crushing phase), and sensels with no significant contribution to the global load. The four groups are randomly distributed over the contact width, with an increasing share of non-participating sensels towards the cylinder sides, and higher local loads towards the center line. In Fig. 56b), the local pressures are integrated over discrete areas with a size comparable to NSG load panels. Here, the load trends are more consistent over the considered areas. It should also be noted that in the full scale measurements, the "sychronized" loads were often registered on 2-3 adjacent load panels only, while the synchronization over 5-6 panels as presented by Palmer and Bjerkås ([63], Fig. 4) was rather rare.
Whether or not the NSG panel loads are also composed of spatially highly varying local loads with different characteristic trends remains unknown.

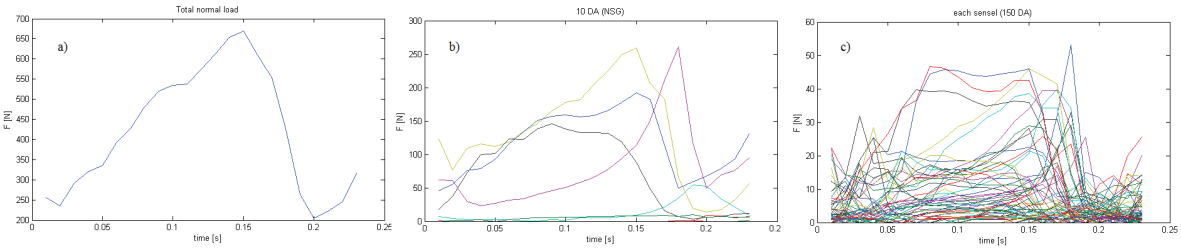

Figure 56: Global load 8(a), local loads (150 discrete areas, c) and NSG-comparable local loads (10 discrete areas, b) during one cycle of FLI, measured in Run 12050. Plot published in [107].

Although the full scale data is not suited to compare the HPZ behaviour on local level, the comparison of full scale and model scale FLI load time histories does not show inconsistency with the previously derived mechanism. Comparison of the load increase during global build-up phase measured in full scale with the model test data shows, however, that the magnification is smaller at NSG than measured in the model tests (see C.2). This could indicate a smaller area increase at low relative velocity of sea ice in large scale interaction than observed in the model ice and small scale tests, or a lower area ratio in simultaneous build-up. Considering the large diameter of NSG lighthouse compared to the model for the laboratory tests, the latter aspect seems plausible. However, there are only few full scale events which could be used to check for the load increase ($n = 3$), so there is limited confidence in their arithmetic mean.
More information on selected full scale events from NSG lighthouse are gathered in [58] and App. C.2.

4.3.2. Comparison of results to current theories

Analysis has revealed that the key mechanism for the occurrence of FLI is creation of a periodic load after a time instance of unloading due to negative (or very low) relative velocity, leading to simultaneous pressure increase in all existing HPZ when the loading starts anew. The corresponding increase of area entails higher nominal pressure, which could be interpreted as increased strength although the local pressure maxima remain the same. The periodicity is imposed onto the ice by the structure.

The experimental observations basically agree to the theory on contact area increase at low relative speed being decisive for FLI vibrations to occur [22]. However, the ideas of a simultaneous failure, synchronization of local failure mechanisms and an increase of (nominal) strength (comp. Sec. 2.3.4) can also be partially justified by the experiments. This is a plausible explanation why all available theories work well for selected validation cases: For any predictive model for the occurrence of FLI, it is essential to include a mechanism which allows higher loads to be periodically transferred to the structure. In

practice, this can be either done uncoupled by a pre-defined saw-tooth shaped loading function, or coupled by an increase of area, of strength, or a combination of these, when the relative velocity has become zero or negative.[18]

[18] Approaches based on strain or strain rate can have the same validity when suitable assumptions on strain rate are made, e.g. a linear relation of strain to structure diameter and displacement.

5. Prediction method for critical velocities for occurrence of frequency lock-in

The characteristic time series for lock-in found in the data analysis can be used to introduce a simple mathematical model, and to derive necessary conditions for the occurrence of frequency lock-in. The following subsections describe the analytical formulation and empirically based simplifications. The method is validated with experimental and full scale data at the end of the chapter.

5.1. Prediction model and analytical formulation

A simple mathematical model is proposed which predicts critical lower and upper ice velocity susceptible for FLI for a vertical structure with known dynamic parameters under defined ice conditios. The model is based on a simplified force time history containing the build-up phase, considered as linear elastic load increase, and a crushing phase, where a constant load is assumed. The simplified load and corresponding response time history are shown in Fig. 57. Similar approaches can be found in ISO guidelines and early research on FLI, e.g. [30,92]. A fundamental difference between the proposed model and the existing ones is the duration and position of build-up phase. ISO suggests a sawtooth-function without constant crushing phase (comp. Fig. 6). Toyama [92] considers a shorter build-up phase and time lag between maximum load and maximum response.

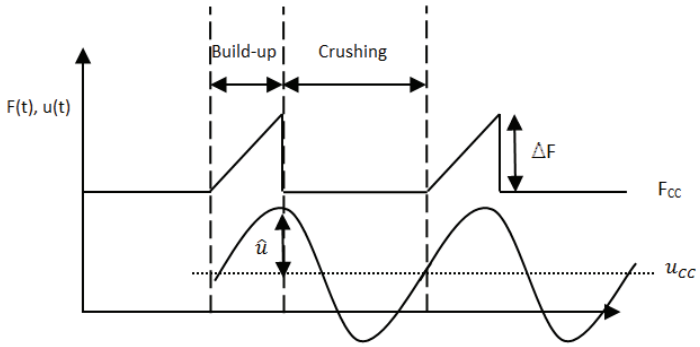

Figure 57: Simplified load and response time history for mathematical model

Considering the problem in a SDOF system, the equation of motion reads:

$$m\ddot{u} + c\dot{u} + ku = F_{\text{ice}}(t) \tag{12}$$

Therein, m, c and k are coefficients of mass, damping and stiffness, respectively. F_{ice} is the ice force, which can be simplified as constant mean crushing load F_{CC} plus phase-dependent build-up force $\Delta F(t)$:

$$F_{\text{ice}}(t) = F_{\text{CC}} + \Delta F(t) \tag{13}$$

ΔF represents the total force increase due to simultaneous build-up, which can be interpreted as a magnification of the brittle crushing load F_{CC} by the factor η:

$$\hat{F}_{ice} = \eta F_{\mathrm{CC}} \tag{14}$$

Considering F_{CC} as static is a major simplification, as the actual response and resulting oscillation velocity (hence also relative velocity) vary greatly during the crushing phase. The variation of indentation speed changes the load. However, the actual time varying load during crushing phase is not relevant for the occurrence of FLI, but its mean value is.
In stationary FLI, the structure response can be considered as sine function superimposed to the static deflection u_{CC}:

$$u(t) = u_{\mathrm{CC}} + \hat{u}\sin(\omega t) \tag{15}$$

The necessary condition for the failure stop to initiate simultaneous build-up is vanishing relative velocity between ice and structure, which occurs when the oscillation velocity is highest. At the end of the build-up phase, which lasts about a quarter oscillation period, ice load has increased by ΔF and oscillation velocity $\dot{u}$ is zero:

$$m\ddot{u} + k(u_{\mathrm{CC}} + \hat{u}) = \eta F_{\mathrm{CC}} \tag{16}$$

Considering $\ddot{u} = 0$ and that the damping part is small compared to the other terms and can be neglected for the simplified consideration, the crushing load and respective displacement are given by:

$$k u_{\mathrm{CC}} = F_{\mathrm{CC}} \tag{17}$$

If lock-in develops, the dynamic amplification factor DAF is greater than one. It relates to the end point of build-up phase, when both displacement and load are at their maximum. When FLI develops, inertia loads $m\ddot{u}$ increase the actual response, and DAF increases. Therefore, DAF=1 denotes the transition towards the amplified condition.
Implementing above formulas yields:

$$\mathrm{DAF} = \frac{u_{\mathrm{CC}} + \hat{u}}{\frac{F_{\mathrm{CC}}+\Delta F}{k}} = \frac{(\frac{F_{\mathrm{CC}}}{k} + \hat{u})k}{\eta F_{\mathrm{CC}}} > 1 \tag{18}$$

From the necessary condition of ratio β in the lock-in range (compare Sec. 2.3.1, Eq.1) the maximum oscillation amplitude can be written as:

$$\beta = \frac{\frac{\mathrm{d}u}{\mathrm{d}t}}{v_{\mathrm{ice}}} \Rightarrow \hat{u} = \frac{\beta v_{\mathrm{ice}}}{\omega} \tag{19}$$

Combining above equations delivers a necessary condition for ice and structure to enter FLI regime:

$$v_{\mathrm{ice}} > \frac{(\eta - 1)F_{\mathrm{CC}}\omega}{\beta k} \tag{20}$$

In Eq. 20, $(\eta-1)$ relates to the increase of ice load in build-up compared to the crushing load. The formula based on the introduced mathematical model and the necessary conditions for FLI predicts the minimum critical velocity (v_{I}) for FLI to occur. The actual critical velocity range is limited by the upper critical velocity v_{II}. In the theoretical framework, structural response has to increase along with the ice drift speed. This requires increasing DAF, which is physically limited by damping of the structure and the magnitude of inertia load the structure can add to the ice load (comp. Eq. 12). Hence, critical velocities can be predicted by:

$$v_{\mathrm{I}} = \frac{(\eta-1)F_{\mathrm{CC}}\omega}{\beta k} \tag{21}$$

$$v_{\mathrm{II}} = \frac{(\mathrm{DAF}_{max}\eta-1)F_{\mathrm{CC}}\omega}{\beta k} \tag{22}$$

5.2. Choice of input parameters

The prediction method introduced above consists of two formulas (Eq. 21 and 22) which contain parameters that can be measured, calculated or estimated as follows:

Load magnification factor η
The load magnification factor η reflects the simultaneous increase of local pressures and growth of HPZ, resulting in a higher build-up force during FLI. Analysis of the experimental data indicates a similar η for all tested scenarios, although a small velocity effect as well as differences based on indenter shape exist. However, the impact of velocity and shape is small and hence negligible in the prediction model where several simplifications have been made. Therefore, all calculated values can be summarized by their mean $\eta = 1.6$, corresponding to the slope of a linear regression curve fitting all experimental data (Fig.58, left)[19].

Crushing load F_{CC}
The mean load during continuous brittle crushing on a vertically sided structure F_{CC} depends mainly on ice parameters (thickness h_{ice}, compressive strength σ_c) and structure parameters (projected width W), combined with a factor accounting for confinement and general differences between actual and nominal contact area and the pressure distribution over the contact (α):

$$F_{\mathrm{CC}} = \sigma_c h_{\mathrm{ice}} W \alpha \tag{23}$$

Equation 23 is known as *Korzhavin's Equation*. It should be noted that α is a function of h_{ice} and W. It can be considered as a combination of two effects: First, the ratio of actual and nominal contact area, which is fairly constant over the entire crushing velocity regime, and second, a ratio taking into account the pressure distribution over contact area as result of confinement. Analysis of the experimental data reveals that

[19] Arithmetic mean of all calculated η values is 1.620, compared to linear regression factor 1.598 with $\mathrm{R}^2 = 0.9917$.

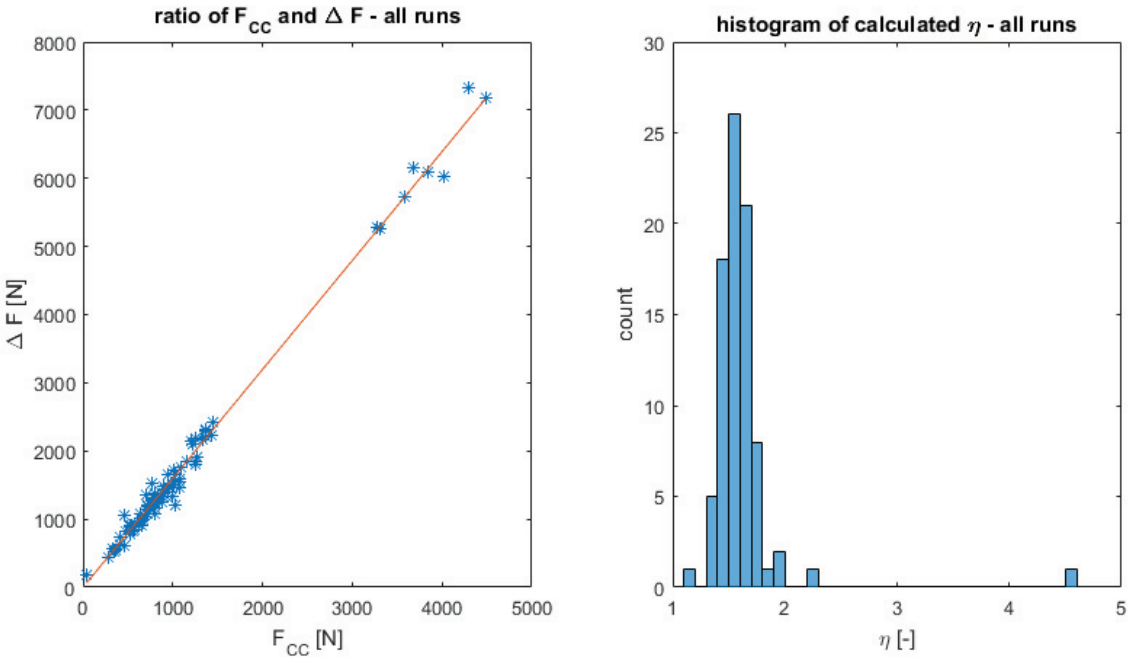

Figure 58: Calculated η values for all observed FLI events of the data set and linear regression curve fit ($\Delta F = 1.6 F_{\mathrm{CC}}$, left), and histogram of η values (right).

this value is about 0.3 for high aspect ratios ($D/h_{\mathrm{ice}} > 10$), while the factor significantly increases for lower aspect ratios. This increase coincides with a larger ratio of actual and nominal contact as briefly discussed in Sec. 4.1.4.
Fig. 59 shows the α values calculated for all evaluable test runs, based on the mean crushing load and the reported mean ice parameters. Only tests with constant mean crushing load were evaluated for prediction of F_{CC}. Due to local inhomogeneities of the model ice sheet and random vibrations of the structure, several test runs fail the demand for constant mean. Based on the remaining experimental data base, α is empirically defined as:

$$\alpha = \begin{cases} 0.3 & \text{for } D/h > 10, \\ 3(D/h)^{-0.995} & \text{for } D/h \leq 10. \end{cases} \tag{24}$$

A potential function fitted to the entire data set approaches $\alpha = 0.3$ for an aspect ratio of 10. This value was additionally validated by comparison to further data sets from HSVA data base for tests on cylindrical structures with high aspect ratio. Experimental data analysed by Yap [97] shows a vanishing confinement effect for D/h of approximately 7. The identified trend matches theoretical indentation factors as a function of aspect ratio by idealizing ice as a purely elastic material, as provided by Croasdale [10].
Simplified, α can be regarded as inversely proportional to D/h for low aspect ratios.

Oscillation frequency ω
The oscillation frequency during FLI ω deviates from the eigenfrequency ω_n due to hydrodynamic effects and added mass and damping from crushed ice. In this study,

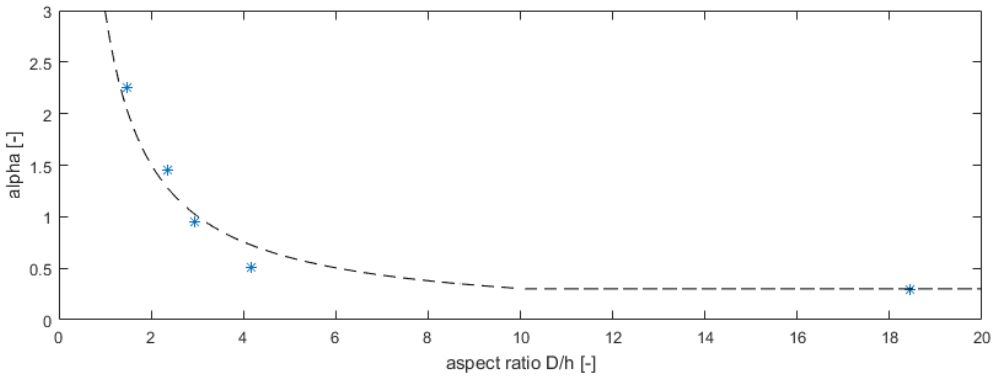

Figure 59: Calculated α factors for all evaluable tests, plotted against aspect ratio D/h_{ice}

necessary criterion for FLI identification is ω being in a range between 0.95 and 1.05 ω_n. These values serve as an upper and lower boundary, if no further information is given for the structure at hand. However, ω can be treated as a constant if one lock-in event is known for a structure, and the model shall be used to find further critical conditions based on the known event. This is possible because analysis has shown that ω is defined by structure and ice parameters and remains practically the same over the entire velocity range, if the ice and structure conditions are unchanged (see Sec. 4.2.1).

Ratio of oscillation velocity and ice drift speed β

The ratio β between maximum structure oscillation velocity and ice drift speed has been reported between 0.8 and 1.5 in literature and physical model tests (comp. Sec. 2.3.1). The formulas presented above help to define a physical upper limit for β: During build-up, the ice edge travels with v_{ice} for the build-up duration, which is about a quarter period. At the same time, the structure moves back with its oscillation velocity $\dot{u} = \beta v_{ice}$. As structure and ice cannot lose contact during build-up without interrupting the FLI interaction, the structure cannot move faster than the ice sheet edge travels:

$$\int_{\frac{\pi}{2\omega}} v_{\mathrm{ice}} \mathrm{d}t = v_{\mathrm{ice}} \frac{\pi}{2\omega} \geq \frac{\beta_{\mathrm{max}} v_{\mathrm{ice}}}{\omega} \Rightarrow \beta_{\mathrm{max}} = \frac{\pi}{2} \tag{25}$$

Equation 25 provides an upper limitation for β which can be used in the prediction formula. The lower boundary remains the value from literature and data analysis (β=0.8).

Structural stiffness k

Structural stiffness of the model at water level in ice drift direction k is typically known for a model in laboratory tests or can be obtained from pullout tests. If the considered system is not of SDOF kind, a generalized stiffness has to be found for the mode that is likely to provoke FLI. This is typically the fundamental eigenmode. In case of non-SDOF setup, stiffness used for static and dynamic deflection have to be treated individually. It should be noted that the method is designed for SDOF systems.

Maximum dynamic amplification factor DAF

The maximum dynamic amplification factor can be estimated based on the damping ratio as fraction of critical damping (ξ) [78]:

$$\mathrm{DAF}_{\max} = \frac{1}{2\xi} \tag{26}$$

Eq. 26 requires knowledge about the damping of the system in crushing condition, hence including surrounding ice. If this full damping ratio is unknown, DAF can be set to three, as typical values range between 2 and 4 [31, 58, 92].

Above parameter identification refines the introduced prediction formulas for critical velocities allowing FLI to develop:

$$v_{\mathrm{I}} = \frac{(\eta - 1)\alpha\sigma_c h_{\mathrm{ice}} W 0.95\omega_n}{\frac{\pi}{2}k} \tag{27}$$

$$v_{\mathrm{II}} = \frac{(\mathrm{DAF}_{\max}\eta - 1)\alpha\sigma_c h_{\mathrm{ice}} W 1.05\omega_n}{0.8k} \tag{28}$$

Figure 60 visualizes the predicted ranges of critical velocities for varying ice parameters for a given structure with known structural parameters.

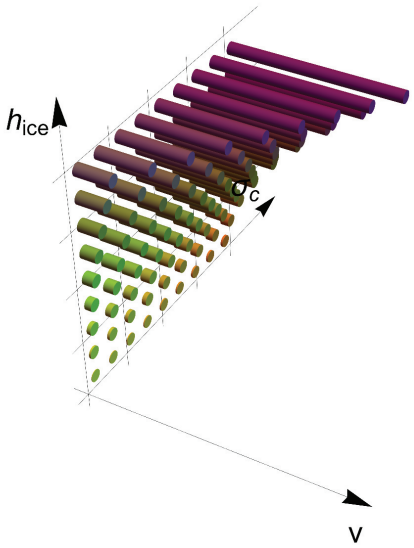

Figure 60: Visualization of identified critical velocity ranges for different ice conditions and constant structure parameters, based on the prediction formulas.

5.3. Validation of the prediction formula

For a first assessment of the model validity, it is applied to the conducted experiments. Since the model bases on analysis of these particular measurements, it is expected to perform satisfying. If large differences are observed between experiments and model prediction, the identification has to be revisited.
Figure 61 shows the predicted and actual critical velocities for all test runs that covered the full velocity range from intermittent to continuous crushing velocity. DAF = 3 is assumed for calculation of the maximum critical velocity.

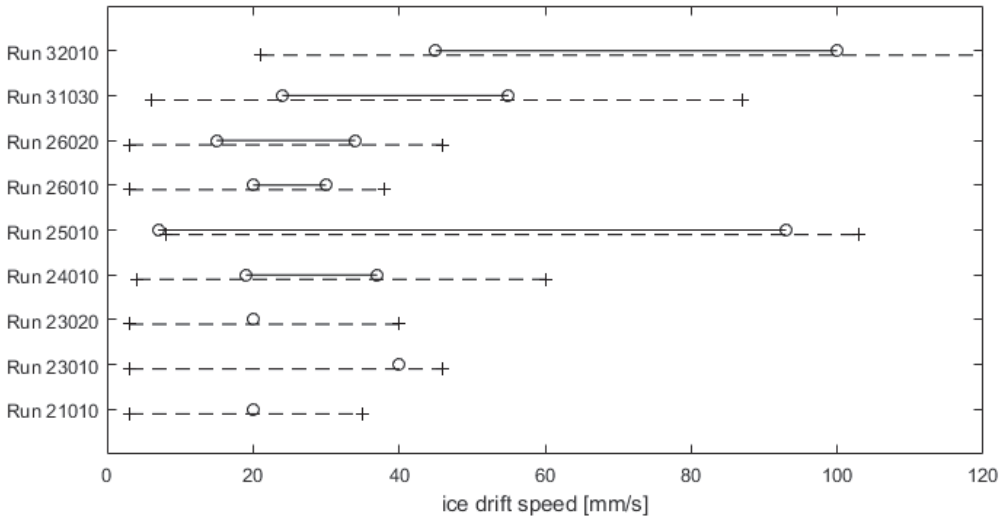

Figure 61: Predicted and measured critical velocities. Dashed lines indicate predicted range, circles and solid lines the interval of actual FLI observations. For details of the test runs refer to Fig. 5.

The model predicts critical velocities conservatively. All observed FLI events fall in the predicted ranges. The prediction formula correctly estimates the highest critical speeds for Run 32030, followed by Run 25010. The trend experimentally observed by Huang [28] and numerically by Hendrikse et al. [26], indicating a shift of transition velocities to higher values for lower stiffness, is reflected in the model.
For Run 32030, $v_{\mathrm{II}} = 293$ mm/s is predicted. Actual observations stop at lower ice velocity, because large deflection of the structure is required to enter lock-in regime. If there is no external excitation, the structural movement is too slow to create the necessary condition of zero relative speed, and the interaction remains in the CC regime.
However, validation with the same data set as used for development is of limited significance. Therefore, a later data set is additionally used. The corresponding experiments are described in [84]. A cylindrical model with 500 mm diameter, natural frequency of 3.4 Hz and translational stiffness at water level of 850 N/mm was tested. The ice thickness was 41 mm and flexural strength 41 kPa. Only flexural strength was measured

ice speed [mm/s]	A1	A2	A3	Actual
lower limit ($\beta = \frac{\pi}{2}$)	11	27	17	15
upper limit ($\beta = 0.8$)	23	54	37	35

Table 11: Comparison of predicted and actual critical velocities for additional data set, based on different assumptions for mean crushing load.

during these tests, which aggravates prediction of F_{CC}. Based on HSVA's data base for flexural and compressive strength values from numerous ice tank tests, it is known that the ratio of flexural and compressive strength is typically in a range between 1 and 2.5 when the flexural strength ranges between 70 and 100 kPa. The validation is done with three assumptions:

- A1: $\sigma_c = \sigma_f$
- A2: $\sigma_c = 2.5\sigma_f$
- A3: F_{CC} taken from measurements

Aspect ratio of the tested cylinder was D/h=11.6; therefore, α is 0.3. Table 11 compiles the estimated and experimentally identified critical velocities for the occurrence of lock-in. It should be noted that the experiments were conducted with stepwise velocity decrement of 5 mm/s, hence experimentally identified transition velocities are not accurate.

If the actual F_{CC} is used, the predicted critical velocities are in close agreement to the measurements. Taking the upper and lower limit predictions for compressive strength delivers a range of critical velocities from 11 to 54 mm/s, which is still in reasonable accordance to the actual FLI range from 15 to 35 mm/s.

Although designed for tests in model ice, the model is also applied to Norströmsgrund Lighthouse to check its applicability to full scale scenarios. Unfortunately, ice conditions have not always been measured, e.g. actual compressive strength is often unknown, and structural parameters are not reported consistently. Still, the data can be used to check whether a reasonable velocity range is predicted. Input parameters are listed along with results in Table 12. Therein, the lower boundary is first calculated with the transition DAF (DAF = 1, $v_{\mathrm{I},1}$), and additionally with observed DAF (DAF = 2, $v_{\mathrm{I},2}$) to check the plausibility of the lower limit estimate based on actually observed events.
The predicted velocities are in good agreement with full scale observations.

5.4. Discussion of the prediction method

The formulas constitute a simple, straight-forward method to determine the critical velocities for FLI occurrence. Furthermore, the same definitions can be used to estimate

Parameter	Value	Source
α	0.3	D/h > 5
F_{CC}	1482 to 533 kN	D = 7.6m, h = 0.25 to 0.9m, $\sigma_c = 2.6$MPa
ω	16.34 s^{-1}	$\omega/\omega_n = 0.98$ (medium estimate)
β	0.8 to $\frac{\pi}{2}$	full range
k	$1.72 \cdot 10^9$ N/m	based on static pullout test results [16]
$v_{\mathrm{I},1}$	0.005 m/s	Based on minimum load estimate, upper boundary for β and DAF = 1.
$v_{\mathrm{I},2}$	0.02 m/s	Based on minimum load estimate, upper boundary for β and DAF = 2.
v_{II}	0.14 m/s	Based on maximum load estimate, lower boundary for β and DAF = 2.
$v_{\mathrm{FLI,min}}$	0.02 m/s	Full scale observation
$v_{\mathrm{FLI,max}}$	0.15 m/s	Full scale observation

Table 12: Comparison of predicted and actual critical velocities from STRICE data (Lighthouse Norströmsgrund, based on values compiled in [57, 105] and observations noted in the STRICE log books [85].)

the structural response of a SDOF system during FLI:

$$u_{\max} = \frac{\alpha \sigma_c h_{\mathrm{ice}} W}{k} + \frac{\pi v_{\mathrm{II}}}{2\omega} \tag{29}$$

Equation 29 has basically already been proposed by Toyama et al. [92], and widely used in research since then. However, the fundamental relation found in the 1980s has here been extended by knowledge on the maximum value of β and suggestions to calculate the mean crushing load, which is treated as input value in [92]. The physically founded upper limit for β explains discrepancies of reported β in literature from the widely accepted range of 1.0 to 1.4. The non-linear increase of crushing load for decreasing aspect ratio observed in model ice has been formulated based on the experimental data. Increased knowledge on the load magnification, above introduced as η, further helps to also estimate the maximum global ice load acting on a structure during FLI. The derived equations agree to the dimensionless parameter for FLI proposed by Yap [97], but extend this value by taking upper and lower boundaries into account. This significantly increases the predictive capability of the proposed method compared to Yap's work.

The method does not deliver time series and cannot be used to assess the interaction of ice with a multi-modal structure. However, it is useful to define a velocity range of interest, which can be investigated in more detail by numerical simulations or further analytical methods. Direct calculation of critical velocities based on a set of known input parameters, as well as prompt estimation of corresponding maximum ice load and maximum amplitude, can be helpful during the design phase of offshore structures and saves time compared to the current industry practice working with time domain simulations [78].

The accuracy of the method compared to state-of-the-art models is assessed by comparison of the predicted critical velocities to calculations performed with a numerical model for coupled calculation of dynamic ice-structure interaction developed by Hendrikse [22, 95]. The model was validated using, amongst others, part of the data set created for the present study [26, 61, 62]. The results of this validation are compared to results from the proposed prediction method in Fig. 62. In [61] two validation cases are made: *Case A* with ice load calculations based on measured mechanical ice properties, and *Case B* using the actual mean crushing load measured during the tests. Further information on the model itself, the input parameters and model calibration are given in the referred publications.

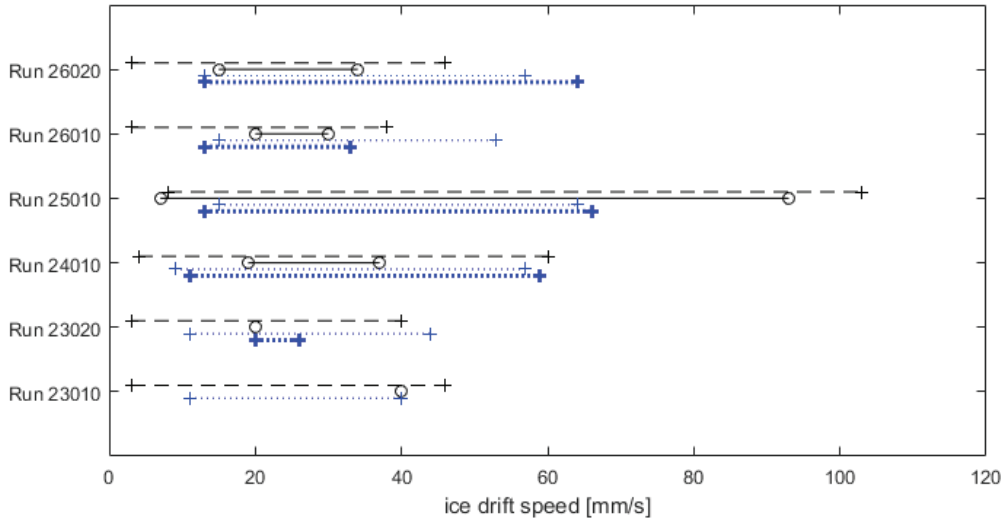

Figure 62: Comparison of predicted velocities for FLI occurrence based on numerical model (blue, thin: Case A, bold: Case B) and proposed prediction method (black, dashed) with experimental observations (black, solid). For details of the test runs refer to Fig. 5.

The numerical model predicts the range of critical velocities well. The prediction improves in Case B compared to Case A. However, Case B does not predict FLI to occur in Run 23010. The authors of the validation study relate this to the presence of flexural deformation of the ice sheet superimposed to the crushing interaction. This bending mechanism also complicates correct crushing load estimation [61]. This accounts both for the numerical model and the prediction method.
The comparison shows that the accuracy of both methods is comparable. Generally, the proposed method is more conservative than the numerical model. The results proof the value of the prediction method for estimation of critical velocities, as its accuracy is satisfying and its calculation time is much lower than that of time domain simulations. The conservatism regarding upper boundary can be explained by the nature of the analytical formula: It basically checks whether FLI can be maintained, given that the

structure oscillates in a frequency close to its natural frequency. As explained above, this needs external impulse if the ice drift speed exceeds the transition speed to continuous crushing. If no excitation is given, the interaction will remain in crushing. However, if the structure is set into oscillations, it may lock-in and maintain the interaction. Therefore, it is likely that predicted high-velocity cases are often not observed in reality.
Additionally, the values for β and ω/ω_n are chosen very conservative. The majority of observed FLI events, both in the current test campaign an in literature, occur with higher β ($>$0.9) and lower ω/ω_n ($<$1.0). v_{II} reduces by almost 15% if the less conservative values are chosen.

Given the considerable simplifications of the dynamic system and the complex ice failure mechanism, the model performs satisfactory. More validation exercises can be found in App. C.3. Results could potentially be improved by further refinement of the upper limit, but this would include more extensive calculations, e.g. to capture the influence of ice damping correctly. Also, a higher minimum DAF could be chosen for the transition to improve the prediction of v_{I}, as DAF $= 1$ requires inertia force to be zero at the end of build-up phase. That is no valid FLI case, since acceleration is in phase opposition to displacement if a harmonic response function is assumed. However, the limitation of DAF $= 1$ is conservative, and constitutes a simple necessary condition for practical use. Next to the real-life application for estimation of critical cases for offshore structure designs which can be further investigated in more detail, the formulas serve as a manual how to produce FLI in model tests, i.e. how to choose structure parameters, ice strength and ice drift speed to allow FLI to develop.

6. Scaling of crushing and ice-induced vibrations in model tests

Analysis of the experimental data presented in Sec. 4 revealed that a simultaneous load build-up after failure stop and subsequent increase of contact area is decisive for the onset of FLI vibrations. Such behaviour was shown for model ice, and it was found that a similar process can exist in nature. In this section, scalability of FLI is discussed.
A major difficulty in scaling FLI from a prototype to a model in a laboratory test is the difference of the involved materials (sea ice and model ice), as the transition from ductile to brittle behaviour as well as the potential load magnification due to simultaneousness of local pressure build-up is believed to highly depend on material properties. Therefore, it is questionable whether transition speeds for FLI regime are in any way scalable from model test to prototype or vice versa. Hence, similitude of FLI within the model regime is studied first, defining a scaling scheme applicable to model tests conducted with model ice, and scaled cylindrical structures.
Afterwards, the reproducibility of the crushing process of sea ice with model ice is assessed, pointing out the shortcomings of standard model ice for this respective application case. Finally, an alternative ice type for laboratory tests is introduced, and results from first tests with the new ice are presented.

6.1. Scaling of crushing interaction and FLI in model ice

State-of-the-art scaling of ice forces in model tests follows Froude and Cauchy scaling laws adapted from model tests with ice-breaking ships, as explained in Sec. 3.1.2. However, this approach has often been questioned, as it makes the model ice rather soft and flexible [64]. Furthermore, the basic justification of Froude similarity being required to preserve the influence of gravitational forces is questionable, as gravitational forces do not play a decisive role in crushing scenarios [66].
Froude number Fr is defined by:

$$Fr = \frac{v}{\sqrt{gL}} \tag{30}$$

Cauchy similarity ensures similitude of elastic forces:

$$Ch = v^2 \frac{\rho}{E} \tag{31}$$

Therein, E is Young's modulus of the ice and ρ ice density. Combination of Eq. 30 and Eq. 31 yields a set of scale factors required to fulfil Froude and Cauchy similarity, which are compiled in Tab. 13.
A common alternative suggested for model tests with crushing scenarios is replica modelling. In replica modelling, all used material is supposed to be identical, and only geometries are scaled. In practice, this delivers much higher ice loads in basin tests, which may exceed the testing capabilities. Furthermore, ice basins are today furnished to prepare model ice, and preparation of geometrically scaled sea ice is difficult. Other approaches are for example summarized by von Bock und Polach and Molyneux [94] and

Quantity	Unit	Scale factor
Length	m	λ
Time	s	$\sqrt{\lambda}$
Velocity	$\frac{\mathrm{m}}{\mathrm{s}}$	$\sqrt{\lambda}$
Force	N	λ^3
Ice Strength	$\frac{\mathrm{N}}{\mathrm{mm}^2}$	λ
Frequency	$1/\mathrm{s}$	$\lambda^{-0.5}$

Table 13: Scale factors for selected properties based on Froude and Cauchy similarity

Palmer and Croasdale [64]. However, none of these have been put into practice so far, as there is no consensus on the correct scaling law amongst researchers yet. Additionally, proposed scaling laws are typically either infeasible due to practically impossible physical parameters of structure or ice, or show inconsistency with FLI characteristics. Therefore, alternative suggestions to scale crushing failure and especially FLI are given below.

For the following derivation, a prototype structure (parameters marked with subscript p) and a model (m) which shall be similar to the prototype with respect to occurrence and magnitude of ice-induced vibrations are considered. Both, model and prototype, interact with model ice, thus the material is regarded as similar.
Following Eq. 23, the crushing load on the prototype is defined by:

$$F_{\mathrm{CC},p} = \sigma_{c,p} h_{\mathrm{ice},p} D_p \alpha_p \tag{32}$$

Similarly, the crushing load on the model is given by:

$$F_{\mathrm{CC},m} = \sigma_{c,m} h_{\mathrm{ice},m} D_m \alpha_m \tag{33}$$

Hence, ice load scales with a strength scale factor λ_σ, a geometric scale factor λ and a ratio of the values for α for differently scaled models. These are not scaled, as α cannot be controlled by the experimentalist. The α-ratio χ ($\chi = \alpha_p/\alpha_m$) has to be taken into account for similarity. One could choose different scale factors for ice thickness and structure geometry; however, keeping the same scale factor for all geometric measures ensures similitude of the aspect ratio, which was found to have a significant impact on the load levels and is a relevant factor for the occurrence of buckling and superimposed bending.
This delivers a scale factor for crushing loads:

$$\lambda_{\mathrm{CC}} = \lambda_\sigma \lambda^2 \chi \tag{34}$$

Equation 34 requires the strength scale to compensate for differences in crushing load level imposed by χ:

$$\lambda_\sigma = \frac{\lambda}{\chi} \tag{35}$$

If crushing tests with rigid structures are considered, implementation of Eq. 34 and Eq. 35 delivers correct load level estimations based on differently scaled structures, accounting for effects of size and confinement in model ice.
It should be emphasized that the dependence of the local pressure distribution on aspect ratio and ice thickness prevents full similitude of two geometrically scaled models. Scale factors can be adjusted such that the obtained loads are similar, but the local processes are inherently different. The occurrence of buckling will not scale correctly, and the contact development between ice and structure differs for different ice thickness. Hence, emphasis is put on the global similarity while acknowledging that local similitude is impossible.

Considering FLI, similarity of the process requires similarity of the dynamic amplification factor. This ensures similar contribution of ice load and inertia force to the structure oscillation:

$$\frac{m_m \ddot{u}_m}{\eta F_{\mathrm{CC},m}} = \frac{m_p \ddot{u}_p}{\eta F_{\mathrm{CC},p}} \tag{36}$$

In addition, the local failure processes governing the occurrence of simultaneous load build-up can be assumed as geometry independent, meaning that the ice will not fail or deform slower or faster if the indenting structure is larger. Thus, time scale factor should be unity, and velocity needs to scale with the same factor as length to preserve similarity of strain rate $\dot{\varepsilon} = v/(2D)$, which is decisive for ductile to brittle transition of the ice in indentation with a cylindrical structure [50]:

$$\frac{v_p}{v_m} = \lambda \tag{37}$$

In case of a SDOF system, the maximum of the structural oscillation acceleration $\ddot{u}_m$ of the model is defined by the oscillation amplitude $\hat{u}_m$ and the oscillation frequency ω_m. Hence, the inertia and ice load ratio (Eq. 36) of model and prototype yields:

$$1 = \frac{m_m}{m_p} \left(\frac{\omega_m}{\omega p}\right)^2 \frac{\hat{u}_m}{\hat{u}_p} \frac{\sigma_{c,p}}{\sigma_{c,m}} \frac{h_{\mathrm{ice},p}}{h_{\mathrm{ice},m}} \frac{D_p}{D_m} = \frac{1}{\lambda_m} \frac{\lambda}{\chi} \lambda^2 \chi \Rightarrow \lambda_m = \lambda^2 \tag{38}$$

With above requirement for scaling the oscillating mass, all necessary scaling factors are defined. If Eq. 36 is fulfilled, prototype and model are similar concerning crushing forces and FLI occurrence. Table 14 summarizes the corresponding scale factors for the most relevant parameters.

Compared to current practice of Froude and Cauchy scaling, the difference of the suggested scaling scheme is preservation of time, and therefore, also natural frequency. This is physically justified by ensuring similarity of crushing behaviour. Violation of Froude similarity entails overestimation of gravitational forces by factor λ. However, gravitational forces are negligible in crushing interaction [64], unless severe ice accumulation plays a significant role, which has not been observed so far. Since model ice and sea ice are supposed to have the same density, the proposed similarity cannot be fully implemented, and buoyancy forces are not correct. Again, their impact on the crushing

Quantity	Unit	Scale factor
Length	m	λ
Time	s	1
Velocity	$\frac{\mathrm{m}}{\mathrm{s}}$	λ
Force	N	λ^3
Ice Strength	$\frac{\mathrm{N}}{\mathrm{mm}^2}$	$\frac{\lambda}{\chi}$
Frequency	1/s	1

Table 14: Proposed scale factors for selected properties

process is minor. The proposed scaling is consistent with the dimensionless parameter for FLI proposed by Yap (Eq. 4, [97]) which requires:

$$\frac{v_p}{v_m} = \frac{\frac{\omega_p}{\omega_m}\lambda^2\lambda_\sigma}{\frac{k_p}{k_m}} \tag{39}$$

However, Yap suggests to use above formulation in conjunction with replica modelling for scaling ice-induced vibrations, and therefore scales time with λ which violates above considerations of local crushing mechanisms being time-independent. Yap argues that velocity should not be scaled, as critical velocities found in model scale tests have the same order of magnitude as those observed in full scale. However, this may be interpreted differently if the stiffness is considered: Replica modelling, as suggested in [97], demands for stiffness to scale with the geometric scale factor λ. But rough comparison of prototype stiffness and stiffness used in model tests indicates a significant difference in the order of stiffness magnitude.[20] This difference results in much larger displacement of the models compared to their diameter. In fact, the observation that the order of magnitude of prototype and model scale critical velocities is the same rather indicates that similar oscillation amplitudes are required for FLI. This seems plausible as the failure depth of the ice can be assumed as a largely scale independent material parameter. However, this basically states that geometric scaling is only possible for small scale factors.

Moreover, the discussion points out another major difficulty of scale model testing of FLI: If stiffness scales with λ^2, large geometric scale factors are required to obtain a feasible stiffness for the compliant model of a full scale prototype structure. Additionally, absolute values of deflection in a scaled model test have to be considered: Oscillation amplitudes of NSG lighthouse are found to be typically about 2 mm in full scale[21]. Scaled down to a feasible model size, the vibrations virtually diminish, and become smaller than typical noise vibrations of the test system.

[20] Prototype stiffness of NSG lighthouse 1720 MN/m, Monopod MDO-1 197 MN/m [25]; minimum model test stiffness 24 kN/m [28], maximum model test stiffness 2460 kN/m [38]; minimum and maximum refer to model test compilation presented in Tab. 1.

[21] This value was found by double time integration of measured acceleration amplitudes. It contains uncertainties stemming from the type of acceleration measurement, but gives evidence for the order of magnitude [58].

To check the proposed scaling factors for the model regime, all model test results from tests with cylinders are scaled to a cylinder with 200 mm diameter using traditional Froude and Cauchy scaling and the proposed scaling scheme. If FLI is observed for more than one velocity, the critical velocity v_{FLI} is set to the mean value of observed minimum and maximum for a clearer presentation of the results. SDOF model stiffness, natural frequency, ice thickness and compressive strength are calculated for the virtual prototype as given in Tab. 15. A reference velocity v_{ref} based on ice and structure parameters is defined as basis for comparison:

$$v_{\mathrm{ref}} = \frac{D\sigma_c h_{\mathrm{ice}}\omega}{k} \tag{40}$$

According to the previously derived prediction formula and literature (e.g. [97]), v_{FLI} is assumed to be linearly dependent on v_{ref}. Results of the comparison are shown in Fig. 63. The coefficient of determination for a linear trend line fitted to the values obtained from the proposed scaling scheme is $R^2 = 0.976$, thus the observed linear dependence of v_{FLI} on the reference velocity is captured well by the scaled model test results. However, this is expected since the proposed scaling bases on the experimental observation of a linear dependence between v_{ref} and v_{FLI}. Froude and Cauchy scaling does not result in a linear trend ($R^2 = 0.610$).

Run	λ [-]	$v_{\mathrm{ref,PS}}$ [mm/s]	$v_{\mathrm{ref,FC}}$ [mm/s]	$v_{\mathrm{FLI,PS}}$ [mm/s]	$v_{\mathrm{FLI,FC}}$ [mm/s]
31030	0.6	47	29	66	19
24010	0.6	33	25	47	15
21010	2.5	5	6	16	63
23010	1	15	15	20	20
23020	2.5	5	7	16	63

Table 15: v_{ref} and v_{FLI} for model tests with cylindrical structures scaled according to Froude and Cauchy (subscript FC) and proposed scaling scheme (PS)

The application of the proposed scaling scheme delivers reasonable results. However, objective validation of the scaling is difficult. The proposed scaling scheme bases on the model test analysis, and therefore matches the deducted relations well. The work by Yap [97] further supports the significance of the linearity between reference velocity and critical velocities for FLI based on full scale data.
A major issue with the proposed scaling scheme is the invariant transition velocity from ductile to brittle behaviour v_{CC}. Although its magnitude is unknown, it can be assumed as a strain rate dependent material parameter. If the geometric scale factor is large, the critical velocities increase compared to a test with a smaller scale factor. Hence, they may become higher than v_{CC}, and FLI does not occur in the tests due to the chosen scale factor. This issue relates to above mentioned minimum oscillation amplitude connected

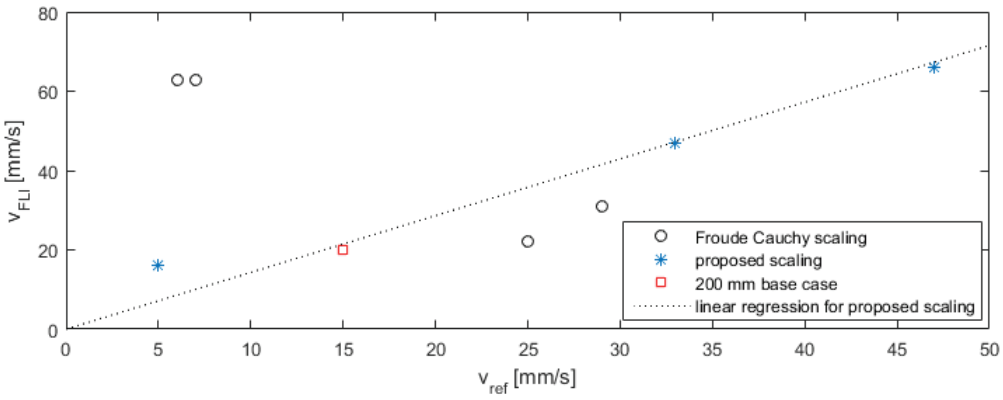

Figure 63: Trend of critical velocities for FLI occurrence over reference velocity obtained from scaled model tests

to the failure depth required for FLI. Hence, the material characteristics essentially require scale factors of unity for displacement and velocity to completely overcome this issue. Preserving the harmonic oscillation relations, time then needs to scale with unity as well. Scaling the stiffness needs to account for differences in crushing load level, stemming from differences in the contact area and in ice strength. Such approach would decouple the developing oscillation from the structure itself. It basically states that any cylindrical model can show comparable FLI vibrations, if the ice is able to transfer the required crushing load to the structure. This can be provided by adjusting the contact area (diameter and ice thickness) and the ice strength. However, this approach can only be used to find critical structure and ice parameters resulting in a similar FLI event as observed in the prototype. It does not deliver any information how the interaction changes when these parameters change. It may not be used to compare different data sets if the requirement of stiffness to scale with the same factor as force is violated.

To conclude, the proposed scaling factors can be useful to compare data sets from model tests within limited ranges, as long as the scale factors are small and the range of critical velocities does not exceed the transition velocity to continuous crushing. However, they are not suited for representation of a full scale prototype structure in the basin for several reasons: First and foremost, the material is different, and the impact of this difference is not scalable. Additionally, SDOF representation of a complex dynamic prototype system with several eigenmodes is a significant simplification, which is believed to affect the results. Finally, the practical feasibility of the prototype representation is limited due to restrictions of feasible stiffness, minimum oscillation amplitude, and transition velocity towards continuous crushing.

6.2. Representation of sea ice crushing behaviour in laboratory tests

Next to the question of similarity between dynamic systems, a fundamental issue with scaled tests on ice crushing against vertical structures is the similarity of the material involved. The limitations of current HSVA standard model ice are described in the following. Afterwards, a new ice type is proposed which can be a starting point for more sophisticated model ice development in the future.

6.2.1. Limitations of model ice

Columnar saline model ice is known to typically suffer from too low ratio of compressive and flexural strength, and too low Young's modulus [76]. Two additional major shortcomings of HSVA's standard model ice (MI) have been identified during test analysis: First, the top layer tends to carry too much of the load, and second, the ice sheet tends to deform and submerge during crushing. Both issues amplify each other, as flexural deformation of the ice sheet results in a tilted ice edge, naturally establishing contact between top layer and structure. The natural wedge-shaped contact in continuous crushing described in Sec. 2.2.3 results from confinement of the center part of the ice where HPZ form, and the possibility for internal cracks in the upper and lower ice parts to open towards the ice surface. In case of a strong top layer close to the center part of the ice (thus thin ice), the top layer prevents opening of the cracks, and shifts the confined zone closer to the top layer. Experimental observations indicate that a minimum thickness of about 45 mm is required in MI for the cracks to also open through the top layer instead of bottom surface only. Hence, only tests in Series 22000, 31000 and 32000 were not affected by interaction of the structure with mainly the top layer. Consequently, these were the only test runs where persistent continuous crushing has been observed.

The inability of the current standard model ice to create persistent crushing time series over the entire ice property range is a major downside, as long measurements of crushing are typically needed to derive meaningful statistical values on mean and peak loads to be expected on a structure. Therefore, reduction of the superimposed bending is inevitable for reliable tests on continuous crushing. Fig. 64 illustrates the different visual appearance of sea ice and model ice crushing against cylindrical structures with similar aspect ratio.

6.2.2. Development of improved model ice for crushing

In Section 6.1, a scaling law for model tests on FLI has been suggested, but it has been pointed out that the process is actually hardly scalable. However, scaled ice model tests could potentially be used to assess the load level during continuous crushing on cylindrical structures, if the problem of superimposed bending and unrealistic transfer of broken rubble in thin ice or high aspect ratio scenarios could be overcome. In order to reduce the significant impact of thickness on the observed interaction, a new model ice type is

Figure 64: Left: Crushing of sea ice against NSG lighthouse [42], right: crushing of model ice against a cylindrical structure with similar aspect ratio

proposed which improves the crushing behaviour in thin model ice.
The basic idea for a new model ice type improved for crushing failure (*improved crushing model ice*, ICMI) is elimination of the strong model ice top layer and increasing the stiffness of the ice sheet.
Limitations for the development of ICMI are given by practicalities: Changing the basin water in the LIMB would be expensive and time-consuming. Therefore, current tank water (7% sodium chloride solution) has to be used. Furthermore, the towing capacity of the main carriage amounts to 50 kN. Thus, some weakening of the ice, i.e. reduced compressive strength, is required to enable testing with reasonably sized models.
In their discussion about scaled model ice, Palmer and Dempsey conclude that "ice is best modelled by real ice" [66]. This conclusion leads back to the basic idea of replica modelling known from solid mechanics, where the same material is used for the model as for the prototype, and only length scales are introduced [47]. Unfortunately, replica modelling is not feasible for ice crushing tests due to extreme ice loads experienced by the structure. If Lighthouse Norströmsgrund is considered as a potentiel prototype structure to be tested in the basin in replica modelling, a geometric scale factor of $\lambda = 10$ is reasonable to obtain a suitable structure width (0.76 m, 7% of basin width). The ice load is then expected to scale by $\lambda^2 = 100$ due to the reduced structure diameter and equally reduced ice thickness. Choosing event 3003-0400-01 with severe FLI, this would lead to almost 50 kN static ice load and more than 10 kN dynamic ice load (see Tab. 22), which is clearly above feasibility limits in the basin.
The fundamental idea for ICMI development is therefore to create a more natural ice under laboratory conditions, which reflects sea ice properties as good as possible, and to weaken the ice while maintaining these properties to maximum possible extent.

Any ice grown in a model basin is in a way "model ice" and differs from sea ice in its crystalline structure and therefore also in its material properties. Sea ice grows over several months. The water temperature continuously decreases when seasons turn to winter. First ice crystals form on the water surface exposed to the cold air. These crystals grow primarily in horizontal direction and conglomerate, often with additional snow, to larger structures such as frazile or pancake ice. The form of the conglomerates

depends on the freezing rate, and the effect of wind and sea state on the ice formation. When a solid ice surface has developed, ice grows mainly downwards. The orientation of this vertical growth is largely defined by the crystalline structure of the top layer. Snow may settle on the surface, refreeze, and hence increase the thickness. The resulting ice sheet typically has a top layer with differing ice parameters, whose thickness is small compared to the overall thickness. As described earlier, the interaction mainly occurs in the middle of the ice, as top and bottom layer are expelled in spalling and flaking. A similar structure shall be created in the laboratory to improve the crushing behaviour of the model ice. Therefore, a more natural initiation of the ice cover is used: instead of the standard spraying procedure (comp. Sec. 3.1.2), the initial crystals shall form while the cold water is kept in motion by wave makers. The new procedure is described in the following.

ICMI is grown in four phases:

1. Pre-cooling phase
2. Wave cooling phase (WCP)
3. Still cooling phase (SCP)
4. Tempering phase

Phase 1, 3 and 4 are the same as in standard MI production. During pre-cooling, the room temperature in the basin is lowered to $-20°C$. Afterwards, all ice is removed. Next, the wave makers are started. Wave makers cover the entire width of the basin and keep the water surface in motion. The parameters of the wave makers can be changed and are subject to optimization in order to create the best possible starting condition for ICMI. After WCP, the initial crystals can either be removed or kept, and the still cooling phase without waves starts. Gassing starts by releasing pressure saturated water into the basin (same procedure as for MI to keep the benefits of white, density-corrected and brittle ice) and is kept until end of tempering phase. The tempering phase lasts only as long as it takes to raise the room temperature to $+2°C$. The end temperature is lower than for MI production ($+4°C$) to reduce the ice weakening. Different end conditions of the WCP were tested as described in [104, 106]. Open water conditions or brash / slush ice proved to be the most promising start condition for ICMI. For reasons of better repeatability, open water was chosen as starting condition. Therefore, all ice was removed after WCP before start of SCP.
Wave parameters have to be chosen such that the resulting waves are not stationary in the basin, but create material transportation to facilitate formation of small single crystals instead of conglomerates. Waves should be short-crested to prevent formation of large crystals.
After WCP, the water is colder than during conventional seeding of MI, and first small crystals have formed. When SCP starts, the initial phase with primarily lateral growth begins. The space for lateral growth of each crystal is limited by other crystals forming

Figure 65: Waves in the basin during WCP (left) and resulting ice sheet ready for testing (right).

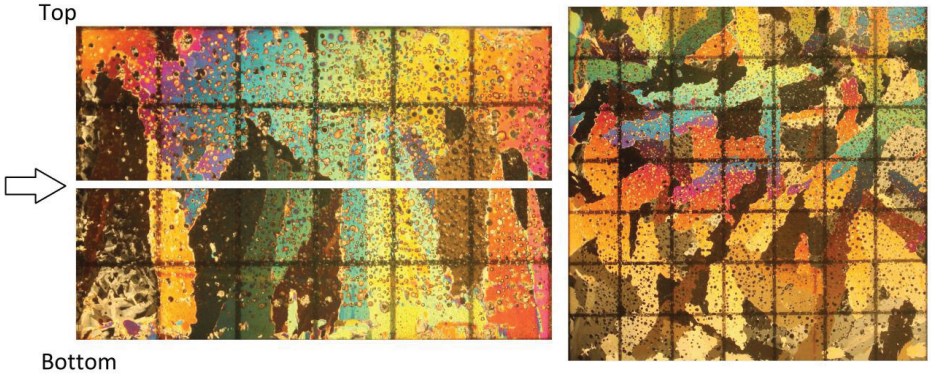

Figure 66: Vertical (left) and horizontal (right) thin sections of ICMI grown for Series 27000, taken by Philipp Hinse (HSVA).

and growing at the same time. The resulting ice sheet is designed to have larger crystals with increased ramification compared to the primarily columnar MI crystals. The related interlocking increases the inner cohesion, supposedly increasing the ice sheet's stiffness and decreasing its tendency to deform in global bending.

6.2.3. Experimental validation of ICMI

An ICMI ice sheet was grown for Series 27000 based on pre-study results [104]. The visual appearance of the ice sheet at end of tempering phase was good, showing the desired white color thanks to the gassing procedure. Fig. 65 shows the waves during WCP and the resulting ice sheet after SCP. A thin section of ICMI is shown in Fig. 66. It proves the aspired crystalline structure, and shows significantly larger crystals than MI (compare Fig. 9 in Sec. 3.1.2).

The performance of ICMI is in the following assessed by three approaches: Visual comparison of the crushing process, evaluation of measured loads, and assessment of mechanical ice properties.

Visual comparison
In Series 27000 (ICMI) and 24000 (MI), the same model with 120 mm diameter was pushed through the ice sheet. A visual comparison of the failure in the two ice types is shown in Fig. 67. Both pictures were taken from events of continuous crushing. There is considerably more crushed ice expelled onto the ice sheet in ICMI. While flooded aerials develop during crushing in MI, no submergence occurs in ICMI.
The limitation of the flexural deformation and prevention of ice sheet submergence is a major improvement of ICMI compared to MI.

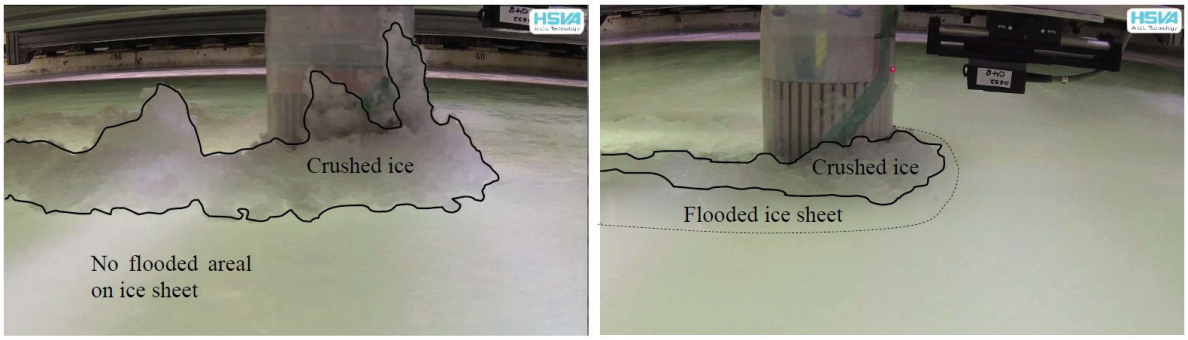

Figure 67: Photographs from Run 27020 (ICMI, left) and Run 24010 (MI, right) with indication of crushed ice and flooded aerials on the ice sheet.

Evaluation of load measurements
Exemplary contact and pressure distributions recorded by the detailed tactile sensors are shown in Fig. 68. The contact in ICMI visually agrees to the ISO definition of the crushing process (Sec. 2.2.3), as location and irregular distribution of pressure in high pressure zones are more realistic.
Exemplary time histories of global ice load originating from MI and ICMI crushing at a similar indentation speed are presented in Fig. 69, along with their spectra obtained from FFT. The aspired irregular, broad-band characteristic of crushing load time series is visible in both ice types.

Figure 70 compares the calculated ratio η between average FLI peak loads in ICMI with the results from MI tests. Despite the considerably smaller data base from ICMI tests, a shift of η towards higher values is clearly visible. Hence, the effect of simultaneous pressure increase and contact area variation is more pronounced in ICMI, resulting in a shift of critical velocities compared to MI scenarios. Other characteristic values, i.e. β, γ and DAF are not significantly affected by the change of ice type (compare results in App. C.1).

Mechanical properties of ICMI
Measured ICMI ice properties are given in Tab. 16 and compared to the standard model ice (MI) sheet grown for Series 24000. The measurements indicate that the quality of

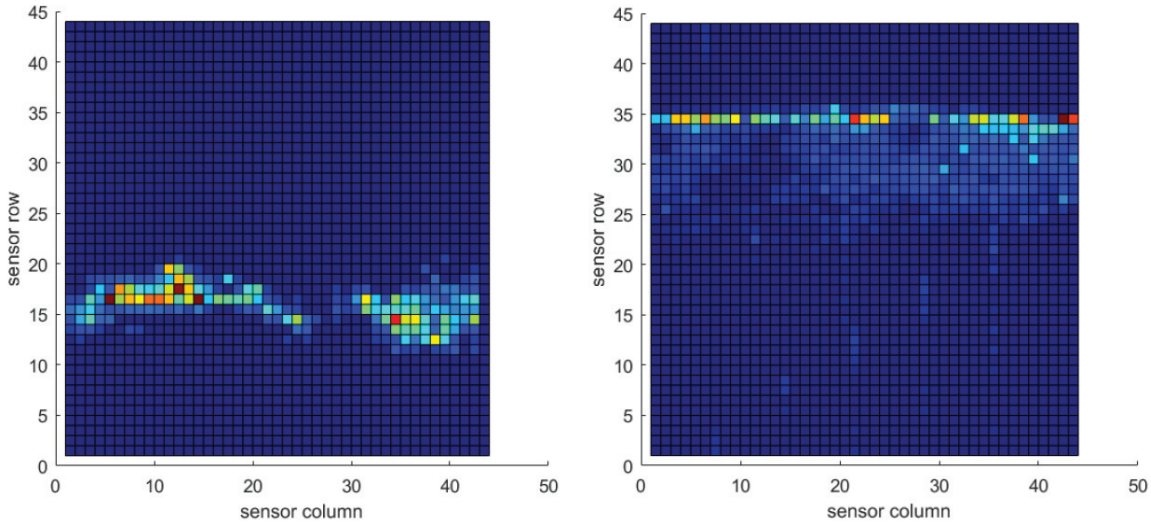

Figure 68: Exemplary raw tactile measurements (Sensor D) showing contact and corresponding pressure distribution during crushing in ICMI (left) and MI (right). While the right distribution indicates interaction with the top layer, the left distribution is similar to the desired characteristic illustrated in Fig. 3.

the ICMI ice sheet is satisfying, as most properties are in the expected range and show comparable scatter as found in MI. Ratio of flexural and compressive strength as well as ratio of flexural strength and qualitative elastic modulus[22] have clearly improved. A major issue is the flexural strength measurement: The cantilever beam tests were performed according to HSVA's standard procedure, which defines the width of a beam based on the ice thickness following ITTC recommendations [8]. Calculation of flexural strength σ_f bases on the assumption that the cantilever fails at the root. However, the ICMI cantilever beams are small compared to the crystal size of the new ice. As ice tends to fail along crystal boundaries in bending, the crack of an ICMI cantilever often does not run straight along the root of the beam but closer to the tip, and also often along an irregular track. Hence, applied theoretical formula for strength calculation and corresponding assumptions on the load case are no longer valid, and the calculated strength value differs from actual flexural strength. Still, the measurements give an indication on the strength level of ICMI compared to MI.

Above considerations show promising behaviour of ICMI in crushing interaction with cylindrical structures. Intermittent crushing and frequency lock-in have been successfully generated in the laboratory using ICMI, proving that the full interaction range is possible. Some additional information on measurements in ICMI are provided in App. A.2.

[22] The qualitative elastic modulus is the Young's modulus calculated from cantilever beam tests by assuming fixed support of the cantilever beam at the root and elastic deformation. This does not deliver a correct ice Young's modulus, but good indication of its magnitude.

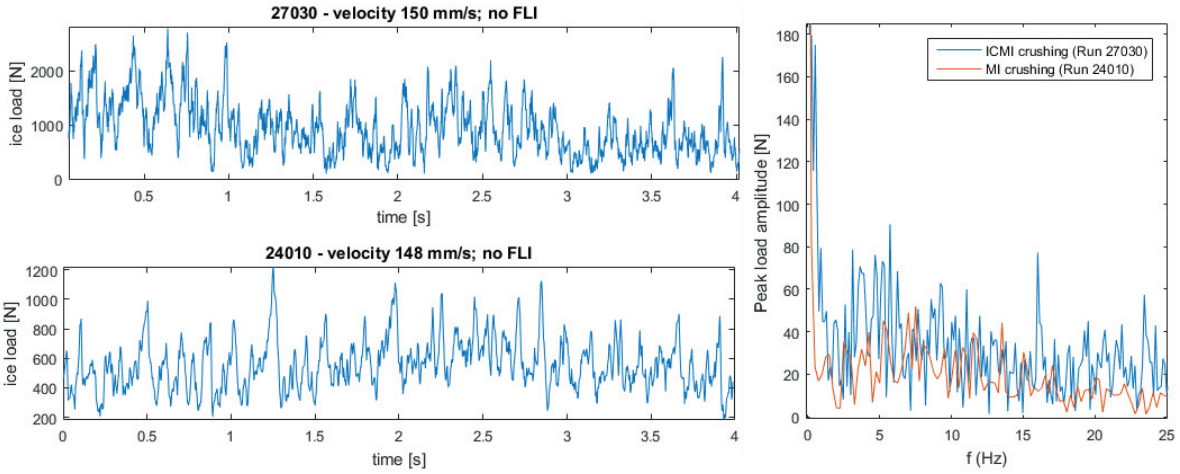

Figure 69: Left: Exemplary time series of continuous crushing in ICMI (top) and MI (bottom), right: corresponding load spectra

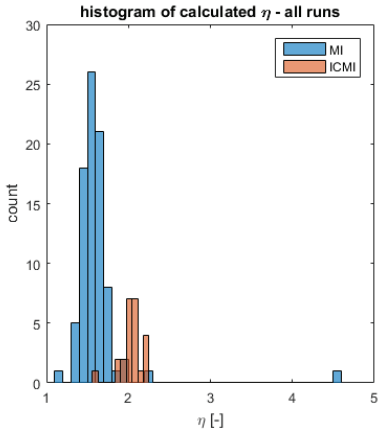

Figure 70: Histogram for η ratio in MI and ICMI

Evaluation and further modification of ICMI for scaled representation of continuous crushing is an ongoing process that exceeds the scope of this work. However, considerations presented above were made to pave the way for continued research in this area. The basic idea of generating a model ice that is more similar to sea ice generally seems promising. Details of the crushing process have to be further investigated on material and local fracture level to validate its similarity to the full scale process.

Property	MI	ICMI	Comment
Ice thickness [mm]	41 [0.048]	38 [0.052]	Thickness scatter in ICMI in the same range as in MI.
Ice density [kg/m^3]	893 [0.001]	809 [0.049]	Lower density and increased scatter in ICMI due to air inclusions resulting from the wave cooling period.
Flexural strength [kPa]	69 [0.077]	128 [0.344]	Significantly larger scatter in measured flexural strength values, resulting from inconclusive failure during cantilever beam tests. The observed scatter may stem partly from inhomogeneity of the ice itself, but also from the measuring method error.
Compressive strength [kPa]	135 [0.071]	454 [0.076]	Compressive strength scatter in ICMI on the same level as in MI.
σ_f/σ_c	1.95	3.5	More realistic ratio of flexural and compressive strength in ICMI.
Qualitative elastic modulus E_q [MPa]	29 [0.188]	483 [0.143]	Qualitative elastic modulus scatter in ICMI is on the same level as in MI.
E_q/σ_f	420	3773	The ratio E_q/σ_f significantly improved in ICMI.

Table 16: Comparison of main ice properties in MI (Series 24000) and ICMI (Series 27000). The table provides mean values and the corresponding coefficient of variation for all conducted property tests in brackets.

7. Conclusion and outlook

Conclusion

In this thesis, the development of frequency lock-in vibrations (FLI) of vertical, bottom-fixed structures in level ice has been studied. Starting point for the presented research was the identification of lacks in the current data basis concerning measurements of FLI, aggravating full validation of existing theories on its physical mechanism.
Therefore, a comprehensive experimental test campaign has been planned and conducted with a test setup that enabled systematic parameter variation of model ice sheet and indenting compliant model. It was possible to generate time histories of all relevant types of crushing, including FLI, for nine different test configurations. These include variation of shape, model width, stiffness, and natural frequency. Additionally, ice thickness and compressive strength have been varied. Application of local pressure mapping technique (tactile sensors) provided novel insight into the physical processes at ice-structure contact area during dynamic ice-structure interaction.
The data analysis revealed important aspects of frequency lock-in. The tactile sensor showed a clear increase of contact area at low relative speed, mainly by increase of high pressure zones in height. This results in adjustment of local loading phases in FLI, and allows for higher global loads to be transferred to the structure by the ice without exceeding the local ice strength. Necessary condition for the area increase is a full failure stop across the interaction area, initiated by low or even negative relative speed.
The experiments have been carried out in three test phases over a time span of four years, including several setup modifications and improvements. However, the dynamic interaction process of a quite large and massive physical test setup with the complex material of model ice contains numerous uncertainties, which are reflected in the analysis. Although the data basis for the presented study was significantly larger than those found in literature over the past decades, only a limited number of events could actually be evaluated in comparative analysis. Hence, compared to other fields of data analysis, the number of experiments is still small, and does not provide a suitable basis for statistic evaluation or data-driven approaches. Still, the derived trends are consistent over the entire data base, and the derived mathematical model shows good agreement to theories and model test as well as full scale measurement results found in literature.
Some reservation regarding application of tactile sensors in dynamic ice model tests persists due to a low pass filter effect inferred by the sensel rise time. However, the characteristics of a full failure stop due to negative relative velocity and subsequent simultaneous increase of the high pressure zones in size and pressure are evident in all measured FLI events, giving clear evidence for the underlying local processes enabling FLI to develop, regardless of qualitative tactile sensor measurement results.

A simple mathematical model, combining state-of-the-art analytical relations with empirical results, was proposed to derive prediction formulas for straightforward estimation of critical velocities that may lead to lock-in for a known structure in specified ice conditions. After model identification with the experimental data, validation with additional

data sets showed satisfying predictive capabilities of the derived prediction formulas.

A scaling scheme was proposed to relate different setups in the model regime. However, it was found that several issues such as non-linear effects of confinement and probability of buckling, scale-independent transition velocity to continuous crushing regime, and practical limitations of physical model implementation aggravate conclusive scaling. It is therefore suggested to study the occurrence of ice-induced vibrations of a prototype structure primarily in theory and with the use of numerical models. The proposed prediction formula can help to define critical ice conditions which are then evaluated numerically in more detail, e.g. in a coupled simulation using a state-of-the-art model [95]. Physical model tests remain a valuable and necessary tool to validate and verify such numerical models. Furthermore, ice model tests can be used to estimate the magnitude of mean crushing loads, and their temporal and spatial evolution. However, that requires realistically scaled representation of the crushing process. The conducted tests have substantiated reservations against utilization of thin columnar saline model ice for crushing tests with vertical structures, since the ice shows exaggerated flexural deformation and an unrealistic distribution of high pressure zones over ice thickness if the model ice sheet is thin or the aspect ratio of structure and ice large. To address this problem, a new procedure to freeze a model ice sheet with improved crushing characteristics has been suggested as part of this study. First tests with the new ice type show promising behaviour.

Outlook

A clearly required next step based on the presented research work is further development of the improved model ice for crushing. This includes studies on the reproducibility of ice parameters in several ice sheets, and a more in-depth analysis of the local failure mechanisms in model ice compared to sea ice.

With respect to the ice-induced vibrations, this thesis can be considered as a further step towards understanding the driving mechanism for the onset of vibrations, which can be found in the contact area development. This finding can guide the way to more sophisticated analysis of the high pressure zones and their evolution in time and space. Such analysis should be accompanied by consideration of the local fracture mechanics of the ice. However, it remains uncertain whether the gathered experimental data is sufficient for such task. If the study should be extended on analysis of local fractures, additional tests of specimens loaded at very low indentation rates may be required. However, conduction of such tests is difficult because larger physical setups typically do not allow to test at constant, low speed due to non-rigidity of setup components.[23] Also, a method would be required to visualize the fracture and possible re-crystallization inside

[23] Attempts have been made to test the studied models in rigid configuration and measure the local loads during indentation with low speed, but these were not successful due to the (unintended) flexibility of the test setup and the tendency of the ice to rapidly fail in buckling before considerable load has established at the contact area.

the ice, thus looking beyond the contact area.
The comparative analysis of MI and ICMI tests revealed a significant difference between the distributions of measured load magnification factors in lock-in (η). The dependence of η on the involved material needs to be further addressed to increase the understanding of the process, but also to improve the prediction formulas.

References

[1] A. Barker, G. Timco, H. Gravesen, and P. Vølund. Ice loading on Danish wind turbines. Part 1: Dynamic Model Tests. *Cold Regions Science and Technology*, 41(1):1–23, 2005.

[2] J. Bechthold, G. Ziemer, K.-U. Evers, P. Jochmann, and N. Hoffmann. Study of local ice pressure distribution on a cylindrical offshore structure using tactile sensors. In *Proceedings of 22nd IAHR International Symposium on Ice*, Singapure, 2014.

[3] M. Bjerkås. Global design ice load's dependence on failure mode. *International Journal of Offshore and Polar Engineering*, 14:189–195, 2004.

[4] M. Bjerkås, B. Bonnemaire, D.S. Sodhi, S. Gehrisch, and P. Jochmann. STRICE Report: Extended Observations Of Ice-Structure Interactions at the Lighthouse Norstrømsgrund Winter 2003. Technical Report Report N. D-3.1, Hydromod, 2003.

[5] M. Bjerkås, C. Lønøy, and A. Gürtner. Seasonal variations in the occurrence of ice-induced vibration of a bottom fixed structure. In *Proceedings of the Twenty-second (2012) International Offshore and Polar Engineering Conference ISOPE*, pages 1358–1364, Rhodes, Greece, 2012.

[6] K. Blenkarn. Measurements and analysis of ice forces on Cook Inlet structures. In *Proceedings of the second annual Offshore and Technology Conference*, volume II, Houston, Texas., 1970.

[7] Y. Chen, B. Yu, Y.M. Low, and K.T. Yap. Modelling randomness in the simulation of ice-induced vibrations. In *Proceedings of the ASME 2018 37th International Conference on Ocean, Offshore and Arctic Engineering*, Madrid, Spain, 2018.

[8] International Towing Tank Conference. *Recommended Procedures and Guidelines*. ITTC, 2014.

[9] K.R. Croasdale. Ice forces on marine structures. In *Proceedings of the IAHR Symposium on Ice*, pages 315–337, Hanover, New Hampshire, USA, 1975.

[10] K.R. Croasdale, N.R. Morgenstern, and J.B. Nuttall. Indentation tests to investigate ice pressures on vertical piers. *Journal of Glaciology*, 81:301–312, 1977.

[11] A. Engelbrektson. Observations of a resonance vibrating lighthouse structure in moving ice. In *Proceedings of the Seventh International Conference on Port and Ocean Engineering under Arctic Conditions*, Helsinki, Finland, 1983.

[12] A. Engelbrektson. An ice-structure interaction model based on observations in the Gulf of Bothnia. In *Proceedings of the POAC 89 Conference on Port and Ocean Engineering under Arctic Conditions*, volume 1, pages 504–519, 1989.

[13] K.-U. Evers and P. Jochmann. An advanced technique to improve the mechanical properties of model ice. In *Proceedings of the Conference on Port and Ocean Engineering under Arctic Conditions*, Hamburg, Germany, 1993.

[14] D. Finn, S. Jones, and I. Jordaan. Vertical and inclined edge-indentation of freshwater ice sheets. *Cold Regions Science and Technology*, 1993.

[15] R. Frederking. Ice pressure variations during indentation. In *Proceedings of the 17th IAHR International Symposium on Ice*, St. Petersburg, Russia, 2004.

[16] R. Frederking. Tiltmeter application at Norströmsgrund Lighthouse. In *Proceedings of the 18th International Conference on Port and Ocean Engineering under Arctic Conditions*, Potsdam, USA, 2005.

[17] R. Gagnon. Consistent observations of ice crushing in laboratory tests and field experiments covering three orders of magnitude in scale. In *Proceedings of the 15th International Conference on Port and Ocean Engineering under Arctic Conditions*, Espoo, Finland, 1999.

[18] R. Gagnon. An inside look at ice-crushing induced vibration and lock-in. In *Proceedings of the 21st International Conference on Port and Ocean Engineering under Arctic Conditions*, 2011.

[19] H. Gravesen, S.L. Sørensen, P. Vølund, A. Barker, and G.W. Timco. Ice loading on Danish Wind Turbines. Part 2: Analyses of dynamic model test results. *Cold Regions Science and Technology*, 41(1):25–47, 2005.

[20] F. Guo. Analysis of the key parameters in ice induced frequency lock-in. In *Proceedings of the 22nd International Conference on Port and Ocean Engineering under Arctic Conditions, POAC13*, Espoo, Finland, 2013.

[21] T. Hammer, J. Koning, K. van Beek, and H. Hendrikse. A 2d motion-controlled test setup for basin tests aimed at dynamic ice-structure interaction. In *Proceedings of the 26th International Conference on Port and Ocean Engineering under Arctic Conditions*, Moscow, Russia, 2021.

[22] H. Hendrikse. *Ice-induced vibrations of vertically sided offshore structures*. PhD thesis, Delft University of Technology, 2017.

[23] H. Hendrikse and A. Metrikine. Interpretation and prediction of ice-induced vibrations based on contact area variation. *International Journal of Solids and Structures*, 2015.

[24] H. Hendrikse and A. Metrikine. Ice-induced vibrations and buckling. *Cold Regions Science and Technology*, 131:129–141, 2016.

[25] H. Hendrikse, M. Seidel, A. Metrikine, and S. Løset. Initial results of a study into the estimation of the development of freqeuncy lock-in for offshore structures subjected to ice loading. In *Proceedings of the 24th International Conference on Port and Ocean Engineering under Arctic Conditions*, Busan, Korea, 2017.

[26] H. Hendrikse, G. Ziemer, and C. Owen. Experimental validation of a model for prediction of dynamic ice-structure interaction. *Cold Regions Science and Technology*, 151, 2018.

[27] G. Huang and P. Liu. A dynamic model for ice-induced vibration of structures. *Journal of Offshore Mechanics and Arctic Engineering*, 2009.

[28] Y. Huang, Q. Shi, and A. Song. Model test study of the interaction between ice and a compliant vertical narrow structure. *Cold Regions Science and Technology*, 2007.

[29] International Standard Organization. *ISO 19906:2010. Petroleum and natural gas industries - arctic offshore structures*, 2010.

[30] International Standard Organization. *ISO 19906:2019. Petroleum and natural gas industries - arctic offshore structures*, 2019.

[31] K. Izumiyama, M. Irani, and G. Timco. Influence of compliance of structure on ice load. In *Proceedings of the 12th IAHR International Symposium on Ice,*, Trondheim, Norway, 1994.

[32] K. Izumiyama and S. Uto. Ice loading on a compliant indentor. In *Proceedings of the 16th International Conference on Offshore Mechanics and Arctic Engineering*, 1997.

[33] K. Izumiyama, D. Wako, and S. Uto. Ice force distribution on a flat indentor. In *Proceedings of the 14th International Symposium on Ice*, Potsdam, New York, USA, 1998.

[34] M. Jefferies and W. Wright. Dynamic response of 'Molikpaq' to ice-structure interaction. In *Proceedings of the Seventh International Conference on Offshore Mechanics and Arctic Engineering*, Houston, Texas, USA, 1988.

[35] X. Ji and E. Oterkus. A dynamic ice-structure interaction model for ice-induced vibrations by using van der pol equation. *Ocean Engineering*, 128:147–152, 2016.

[36] X. Ji and E. Oterkus. Physical mechanism of ice-structure interaction. *Journal of Glaciology*, 2018.

[37] I. Jordaan. Mechanics of ice-structure interaction. *Eng. Fract. Mech*, 2001.

[38] K. Kamesaki, Y. Yamauchi, and T. Kärnä. Ice force as a function of structural compliance. In *Proceedings of the 13th IAHR International Symposium on Ice*, Beijing, China, 1996.

[39] T. Kärnä. Steady-state vibrations of offshore structures. *Hydrotechnical construction*, 28:446–453, 1994.

[40] T. Kärnä, H. Andresen, A. Gürtner, A. Metrikine, D. Sodhi, M. Loo, G. Kuiper, R. Gibson, D. Fenz, K. Muggeridge, C. Wallenburg, J.-F. Wu, and M. Jefferies. Ice-induced vibrations of offshore structures - looking beyond ISO 19906. In *Proceedings of the 22nd International Conference on Port and Ocean Engineering under Arctic Conditions*, Helsinki, Finland, 2013.

[41] T. Kärnä, K. Izumiyama, Q. Yue, Y. Qu, F. Guo, and N. Xu. An upper bound model for self-excited vibrations. In *Proceedings of the POAC 2007 International Conference on Port and Ocean Engineering under Arctic Conditions*, pages 177–189, Dalian, China, 2007.

[42] T. Kärnä and P. Jochmann. Field observations on ice failure modes. In *Proceedings of the 17th International Conference on Port and Ocean Engineering under Arctic Conditions*, pages 839–848, Trondheim, Norway, 2003.

[43] T. Kärnä, K. Kamesaki, and H. Tsukada. A numerical model for dynamic ice-structure interaction. *Comput. Struct.*, 1999.

[44] T. Kärnä, K. Kolari, P. Jochmann, K.-U. Evers, X. Bi, M. Määttänen, and P. Martonen. Tests on dynamic ice-structure interaction. In *Proceedings of OMAE 2003 22nd International Conference on Offshore Mechanics and Arctic Engineering*, Cancun, Mexico, June 2003.

[45] T. Kärnä and A. Muhonen. Preliminary results from ice indentation tests using flexible and rigid indentors. In *Proceedings of the Tenth IAHR International Symposium on Ice*, Espoo, Finland, 1990.

[46] T. Kärnä and R. Turunen. Dynamic response of narrow structures to ice crushing. *Cold Regions Science and Technology*, 17:173–187, 1989.

[47] T. Malmberg. *Aspects of Similitude Theory in Solid Mechanics, Part I: Deformation Behaviour*. Forschungszentrum Karlsruhe, FZKA 5657, 1995.

[48] H. Matlock, W.P. Dawkins, and J.J. Panak. A model for the prediction of ice-structure interaction. In *Proceedings of the First Annual Offshore Technology Conference*, pages 687–694, Houston, Texas, 1969.

[49] H. McQueen and N. Srinil. A modified matlock-duffing model for two-dimensional ice-induced vibrations of offshore structures with geometric nonlinearities. *Journal of Offshore Mechanics and Arctic Engineering*, 2016.

[50] B. Michel. *Ice Mechanics*. Laval University, Quebec, 1978.

[51] B. Michel and D. Blanchet. Indentation of an s_2 floating ice sheet in the brittle range. *Ann. Glaciol.*, 19(81):285–300, 1983.

[52] M. Määttänen. Laboratory tests for dynamic ice-structure interaction. Technical report, DTIC, 1979.

[53] M. Määttänen. Modelling the interaction between ice and structures. In *Proceedings of the Seventh International Conference on Port and Ocean Engineering under Arctic Conditions*, Helsinki, Finland, 1983.

[54] M. Määttänen. Numerical model for ice-induced vibration load lock-in and synchronization. In *Proceedings of the 14th IAHR International Symposium on Ice*, pages 923–930, Potsdam, New York, 1999.

[55] M. Määttänen and E. Järvinen. Baltic aids-to-navigation ice-induced vibration measurements 2003. Technical report, Helsinki University of Technology, 2003.

[56] M. Määttänen, S. Løset, A. Metrikine, K.-U. Evers, C. Lønøy, I. Metrikin, T. Nord, and S. Sukhorukov. Novel ice induced vibration testing in a largescale facility: deciphering ice induced vibrations, part 1. In *Proceedings of the 21st IAHR international Symposium on Ice*, pages 946–958, Dalian, China, 2012.

[57] T. Nord, I. Samardzija, H. Hendrikse, M. Bjerkås, K. Hoyland, and H. Li. Ice-induced vibrations of the Norströmsgrund lighthouse. *Cold Regions Science and Technology*, 155:237–251, 2018.

[58] G. Onken. Design of a physical analogous model for the study of dynamic ice-structure interaction. Master's thesis, Hamburg University of Technology, 2012.

[59] G. Onken, K.-U. Evers, A. Haase, and P. Jochmann. Ice model tests with a cylindrical structure to investigate dynamic ice-structure interaction. In *Proceedings of the 22nd International Conference on Port and Ocean Engineering under Arctic Conditions*, Espoo, Finland, 2013.

[60] B. O'Rourke, I. Jordaan, R. Taylor, and A. Gürtner. Experimental investigation of oscillation of loads in ice high-pressure zones, part 1: Single indentor system. *Cold Regions Science and Technology*, 124:25–39, 2016.

[61] C. Owen and H. Hendrikse. Ice-induced vibrations of model structures with various dynamic properties. In *Proceedings of the 24th International Symposium on Ice*, pages 376–385, Vladivostok, Russia, 2018.

[62] C. Owen and H. Hendrikse. A study of the transition speed from intermittent crushing to freqency lock-in based on model-scale experiments. In *Proceedings of the 25th International Conference on Port and Ocean Engineering under Arctic Conditions*, Delft, The Netherlands, 2019.

[63] A. Palmer and M. Bjerkås. Synchronisation and the transition from intermittent to locked-in ice-induced vibration. In *Proceedings of the 22nd International Conference on Port and Ocean Engineering under Arctic Conditions*, Helsinki, Finland, 2013.

[64] A. Palmer and K. Croasdale. *Arctic Offshore Engineering*, chapter Ice Forces on Structures in the Sea. World Scientific, 2013.

[65] A. Palmer and J. Dempsey. Model tests in ice. In *Proceedings of the 20th International Conference on Port and Ocean Engineering under Arctic Conditions*, Lulea, Sweden, 2009.

[66] A. Palmer, Q. Yue, and F. Guo. Ice-induced vibrations and scaling. *Cold Regions Science and Technology*, 60(3):189–192, 2010.

[67] H.R. Peyton. Sea ice forces. In *Ice Pressures Against Structures*, 1968.

[68] W. Popko. *Impact of Sea Ice Loads on Global Dynamics of Offshore Wind Turbines*. PhD thesis, Leibniz Universität Hannover, 2019.

[69] W. Qiu and T. Wu. Numerical simulation of ice-induced vibrations of steady-state type. *Advances in Structural Engineering*, 22, 2019.

[70] M. Richard and R. Taylor. Analysis of high pressure zone attributes from tactile pressure sensor field data. In *Proceedings of the ASME 2014 33rd International Conference on Ocean, Offshore and Arctic Engineering*, San Francisco, USA, 2014.

[71] P. Ruckert. Kalibrierung und Equilibrierung eines TekScan-Sensors. Technical report, TUHH, 2019. (in German).

[72] H. Saeki, K. Hirayama, T. Kamesaki, S. Akagawa, K. Kato, K. Kawesaki, K. Saka, and A. Kurokawa. JOIA project of study on ice load. In *Proceedings of the 13th IAHR International Symposium on Ice*, pages 17–27, Beijing, China, 1996.

[73] E. Schulson. Brittle failure of ice. *Engineering Fracture Mechanics*, 68:1839–1887, 2001.

[74] E. Schulson and P. Duval. Creep and fracture of ice. Technical report, Cambridge University Press, 2009.

[75] J. Schwarz. The pressure of floating ice-fields on piles. In *Proceedings of the IAHR International Symposium on Ice and Its Action on Hydraulic Structures*, page 12, Reykjavik, Iceland, 1971.

[76] J. Schwarz. New developments in modeling ice problems. In *Proceedings of the 4th international Conference on Port and Ocean Engineering under Arctic Conditions, POAC 77*, pages 45–61, St. John's, Newfoundland, Canada, 1977.

[77] J. Schwarz and P. Jochmann. Ice force measurements within the LOLEIF-project. In *Proceedings of the 16th International Conference on Port and Ocean Engineering under Arctic Conditions*, volume 2, pages 669–682, Ottawa, Canada, 2001.

[78] M. Seidel and H. Hendrikse. Analytical assessment of sea ice-induced frequency lock-in for offshore wind turbine monopiles. *Marine Structures*, 60:87–100, 2018.

[79] S. K. Singh, G.W. Timco, R. Frederking, and I. Jordaan. Tests of ice crushing on a flexible structure. In *Proceedings of the Ninthth Offshore Mechanics and Arctic Engineering Symposium*, volume 4, pages 89–94, Houston, Texas, 1990.

[80] D. S. Sodhi. Ice-induced vibrations of structures. In *Proceedings of theNinth IAHR International Symposium on Ice*, Sapporo, Japan, 1988.

[81] D. S. Sodhi. Crushing failure during ice-structure interaction. *Engineering Fracture Mechanics*, 68:1889–1921, 2001.

[82] D.S. Sodhi. Effective pressures measured during indentation tests in freshwater ice. In *Proceedings of the Sixth International Cold Regions Engineering Speacialty Conference*, pages 619–627, Hanover, New Hampshire, 1991.

[83] D.S. Sodhi, T. Takeuchi, N. Nakazawa, S. Akagawam, and H. Saeki. Medium-scale indentation tests on sea ice at various speeds. *Cold Regions Science and Technology*, 28:161–182, 1998.

[84] T. Stange, G. Ziemer, and R.U.F. von Bock und Polach. Development of an experimental setup to investigate the impact of higher structural modes on dynamic ice-structure interaction. In *Proceedings of the 25th IAHR International Symposium on Ice*, Trondheim, Norway, 2020.

[85] STRICE Logbooks, 2001 - 2003. Excel files.

[86] R. Taylor, R. Frederking, and I. Jordaan. The nature of high pressure zones in compressive ice failure. In *Proceedings of the 19th IAHR International Symposium on Ice*, Vancouver, Canada, 2008.

[87] Tekscan Inc., South Boston, MA. *I-Scan User Manual*, 2011.

[88] G.W. Timco. Ice forces on structures: physical modelling techniques. Technical report, Second IAHR State-of-the-art report on ice forces on structures, special volume of proceedings IAHR symp. on Ice, 1984.

[89] G.W. Timco. Indentation and penetration of edge-loaded freshwater ice sheets in the brittle range. *Journal of Offshore Mechanics and Arctic Engineering*, 3(109):287–294, 1987.

[90] G.W. Timco. Laboratory observations of macroscopic failure modes in freshwater ice. In *Proceedings of the Sixth International Cold Regions Engineerings Specialty Conference*, pages 605–614, New Hampshire, USA, 1991.

[91] G.W. Timco, M.B. Irani, J. Tseng, L.K. Liu, and C.B. Zheng. Model tests of dynamic ice loading on the chineses JZ-20-2 jacket platform. *Canadian Journal of Civil Engineering*, 19:819–832, 1992.

[92] Y. Toyama, T. Sensu, M. Minami, and N. Yashima. Model tests on ice-induced self-excited vibration of cylindrical structures. In *Proceedings of the Seventh International Conference on Port and Ocean Engineering under Arctic Conditions*, Helsinki, Finland, 1983.

[93] M. Tsuchiya, S. Kanie, K. Ikejiri, A. Yoshida, and H. Saeki. An experimental study on ice-structure interaction. In *Proceedings of the Seventeenth Annual Offshore Technology Conference*, Houston, Texas, 1985.

[94] R.U.F. von Bock und Polach and D. Molyneux. Model ice: A review of its capacity and identification of knowledge gaps. In *Proceedings of the ASME 2017 36th International Conference on Ocean, Offshore and Arctic Engineering*, Trondheim, Norway, 2017.

[95] T. Willems and H. Hendrikse. Coupled simulation of ice-structure interaction of offshore wind turbines in BHAWC using VANILLA. In *Proceedings of the 25th International Conference on Port and Ocean Engineering under Arctic Conditions*, Delft, The Netherlands, 2019.

[96] M. Withalm and N. Hoffmann. Simulation of full-scale ice-structure interaction by an extended matlock model. *Cold Regions Science and Technology*, 60(2):130–136, 2010.

[97] K.T. Yap. *Level Ice-Vertical Structure Interaction: Steady-state self-excited vibration of structures.* PhD thesis, National University of Singapore, 2011.

[98] K.T. Yap and A. Palmer. A model test on ice-induced vibrations: structure response characteristics and scaling of the lock-in phenomenon. In *Proceedings of the 22nd International Conference on Port and Ocean Engineering under Arctic Conditions*, pages 1–11, Espoo, Finnland, 2013.

[99] Q. Yue and F. Guo. Physical mechanism of ice-induced self-excited vibration. *Journal of Engineering mechanics*, 138, 2012.

[100] Q. Yue, Y. Qu, X. Bi, and T. Kärnä. Ice force spectrum on narrow conical structures. *Cold Regions Science and Technology*, 49(2):161 – 169, 2007.

[101] Q. Yue, X. Zhang, X. Bi, and Z. Shi. Measurements and analysis of ice-induced steady state vibration. In *Proceedings of the 16th International Conference on Port and Ocean Engineerung under Arctic Conditions*, pages 413–421, Ottawa, Canada, 2001.

[102] G. Ziemer. IVOS Project Report 2015. Technical report, HSVA, 2015.

[103] G. Ziemer. IVOS Project Description. Technical report, HSVA, 2017.

[104] G. Ziemer. Towards a novel type of ice for model tests with vertically sided structures. In *Proceedings of the ASME 37th International Conference on Ocean, Offshore and Arctic Engineering OMAE 2018*, Madrid, Spain, 2018.

[105] G. Ziemer. Schlussbericht CoPSIS - Contact Pressure and Scaling of Ice-Structure-Interaction. Technical Report HSVA Forschungsbericht Nr. 1694, HSVA, 2019.

[106] G. Ziemer. Utilization of tactile sensors to investigate local ice pressure in scale model tests. In *Proceedings of the 6th International Conference on Advanced Model Measurement Technology for The Maritime Industry*, Rome, Italy, 2019.

[107] G. Ziemer and C. Deutsch. Study of local pressure and synchronization during frequency lock-in. In *Proceedings of the 23nd International Conference on Port and Ocean Engineering under Arctic Conditions*, Trondheim, Norway, 2015.

[108] G. Ziemer and K.-U. Evers. Model tests with a compliant cylindrical structure to investigate ice-induced vibrations. *Journal of Offshore Mechanics and Arctic Engineering*, 138, 2016.

A. Details on conducted model tests

Ice and structure parameters for all conducted test runs within the IVOS campaign, which forms the basis for the presented thesis, are collected below. First, the methods to assess these parameters are briefly described in the following subsection.

A.1. Determination of physical parameters

Physical parameters of the model ice and the test setup need to be assessed for each test. The determination methods are described below. Actual values for all test runs are compiled at the end of this appendix.

Determination of ice properties

Ice properties were determined during the IVOS project according to standard procedures. Following descriptions and figures are taken from HSVA's standard report template *App A HSVA Standard Model Ice*, with minor adjustments wherever relevant for the presented study.

Ice thickness
The thickness of the model level ice is measured after each level ice test by a slide caliper rule. The measurements are taken every meter on one side of the edge of the broken channel. All measured values are averaged over the length of the test track to obtain the thickness value representative for the respective tests.

Flexural strength
The flexural strength is determined by cantilever beam tests. The load is applied with an electrically driven loading device and applied load is recorded. The beam dimensions are $1h \times 2h \times 6h$, where h is the ice thickness.
The flexural strength is calculated from the failure force measurements by using the equation:

$$\sigma_f = \frac{6FL}{Bh_{ice}^2} \tag{41}$$

Therein, F is the failure load identified from the force measurement, L is the length of the beam (load point to root), B the width of the beam (at the root), and h_{ice} the thickness of the ice.
For level ice tests, strength measurements are carried out several times during the tempering phase and once directly before or after the test is performed. Whenever possible, the strength is measured at four different locations distributed over the tank length. Three cantilever beams are prepared at each location. The prepared cantilever beams and a schematic illustration of the test setup are shown in Fig. 71

Compressive strength
Uniaxial compression tests are carried out on a rigid closed loop controlled test frame

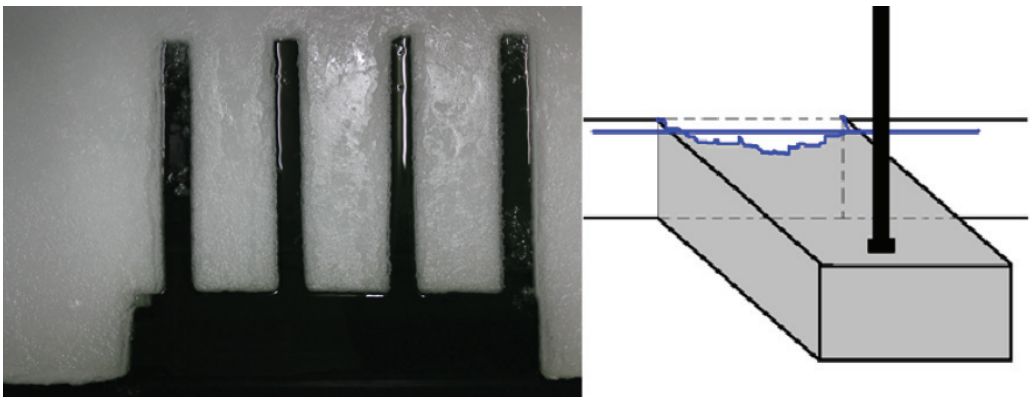

Figure 71: Cantilever beams prepared for flexural strength test, and illustration of the flexural strength measurement setup. From HSVA report template.

using an electric actuator for load application as it has the highest accuracy with respect of strain rate control. Prismatic ice samples having a size of $1h \times 2h \times 4h$, with h being the ice thickness, are cut and placed in between the two loading plates of the test frame. Fig. 72 shows such an arrangement.
The applied load and crosshead movement is recorded and the results are presented as load deflection curve. The compressive strength is calculated from the failure load identified from this curve according to following formula:

$$\sigma_c = \frac{F}{h_{\text{ice}} B} \tag{42}$$

Therein, F is the failure force, h_{ice} ice thickness, and B specimen width. Hence, h and B constitute the cross-sectional area.

Density and Salinity
At HSVA a special method to determine ice density is applied. Ice samples (120mm $\times$ 120mm $\times$ h_{ice}) are sampled from the model ice sheet at locations where cantilever beam tests are carried out and stored in a plastic bowl filled with tank water in order to avoid drainage. The testing procedure is presented in Fig. 73.
Salinity is measured with a salinometer using melted density samples.

Young's modulus – plate deflection method
The modulus of elasticity of the model ice is by standard determined by applying the infinite plate method. Hereby the ice cover is loaded at some locations along the centerline of the ice tank with defined weights, e.g. 50 g or 200 g depending of the sheet ice thickness. The deflection of the ice cover is measured at the center of the load by means of a LVDT (Fig. 74). Both load and deflection are recorded. At the same time flexural strength measurement is carried out for establishing the E/σ_f ratio. Preferably the modulus of elasticity is determined in undisturbed conditions before the first test run starts.

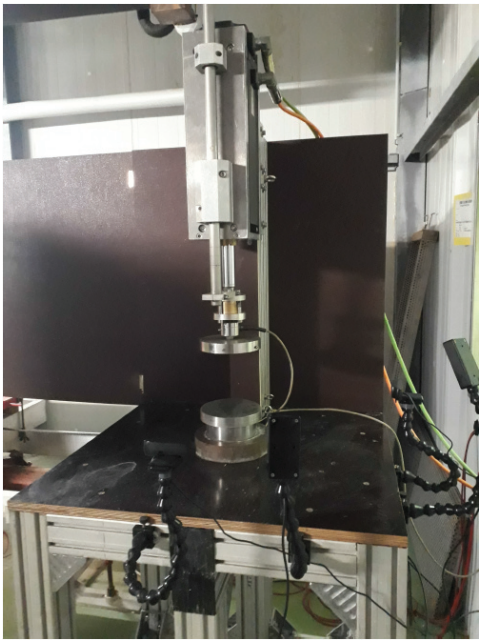

Figure 72: Uniaxial compression testing machine as used at HSVA

The modulus of elasticity can be calculated according to:

$$E = 0.1875 \cdot 109 \left(\frac{F}{w}\right)^2 \frac{1-\nu^2}{\rho_w g h_{\text{ice}}^3} \tag{43}$$

Where E is elastic modulus [MPa], rho_w water density (typically 1006 [kg/m^3], g acceleration due to gravity [m/s^2], $\rho_w g$ foundation factor for elastic foundation, ν Poisson's ratio (0.3), h_{ice} ice thickness [mm], and w measured plate deflection [mm].
The actual Young's modulus is calculated as the mean between all conducted weight steps. The steps are shown in Fig. 74.

Qualitative elastic modulus – beam deflection method
Determination of the Young's modulus by plate deflection method is time consuming and cannot be repeated in the damaged ice sheet in between tests. An alternative property to qualitatively compare the elasticity of different ice sheets is the elastic modulus obtained from the cantilever beam tests performed to obtain the flexural strength:

$$E_q = \frac{4FL^3}{h_{\text{ice}} B w} \tag{44}$$

Therein, the input parameters are the same as used for the flexural strength measurement (see above), plus the deflection of the beam at the tip w which is assumed to equal the speed of the linear piston which loads the cantilever, multiplied by the loading duration. The loading duration can be read from the load time series. It should be noted here that ice does not behave fully linear elastic until failure. Therefore, above formula

Test Series:		1000	
Water Density:	ρ_{water} =	1004.8	[kg/m³]
Water Salinity:	S_w =	7.0	[‰]
Oxygen set value:	O_2 =	18.0	[mg/l]

Ice Density ρ_i :

$$\rho_i = \left(\frac{w_2 - w_1}{w_3 - w_1} \right) \rho_w$$

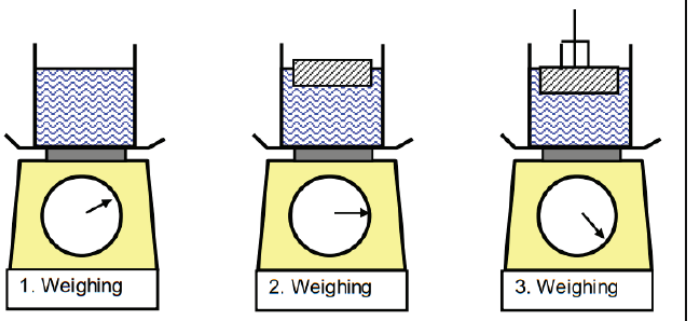

Specimen No. or x \ y-Tank Pos.	w_1 [g]	w_2 [g]	w_3 [g]	ρ_{ice} [kg/m³]	Salinity S_{ice} [‰]
54/1.5	0	387	431	902	3.1
54/1.5	0	397	540	739	3.2
66/1.5	0	399	456	879	3.4
mean >>>	0.0	394.3	475.7	840.0	3.2

Figure 73: Density calculation and documentation sheet

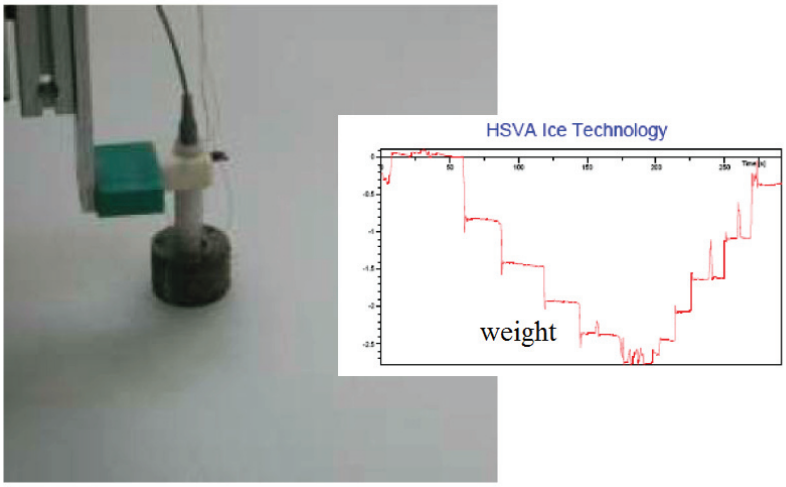

Figure 74: Device for plate deflection and time history of Young's modulus measurement.

is not fully applicable, but gives an indication on qualitative differences when no actual Young's modulus can be obtained.

Friction tests

The dynamic friction coefficient between ice and model surface is determined by using a testing apparatus as shown in Fig. 75. Instead of the model itself, a plate which has been painted together with the model is used for the friction test. In case of the IVOS tests, the friction test plate was covered with the same plastic foil as used for tactile sensor protection. The test plate is moved under the ice piece, which is put upside down onto the test plate. The ice piece is held in place by a frame suspended from a bridge frame. The tangential force is measured with two slightly pre-stressed load cells mounted between the frame and the bridge frame. The normal load on the contact surface is applied by the weight of the ice piece plus a variable ballast weight. The friction tests are performed at a speed of 0.1 m/s. The friction coefficient is then calculated according to Coulomb's friction law:

$$\mu = \frac{F_T}{F_V} \tag{45}$$

Therein, μ denotes the dynamic friction coefficient, F_T is the mean value of the measured tangential (friction) force during steady motion, and F_N the normal load on the contact surface.

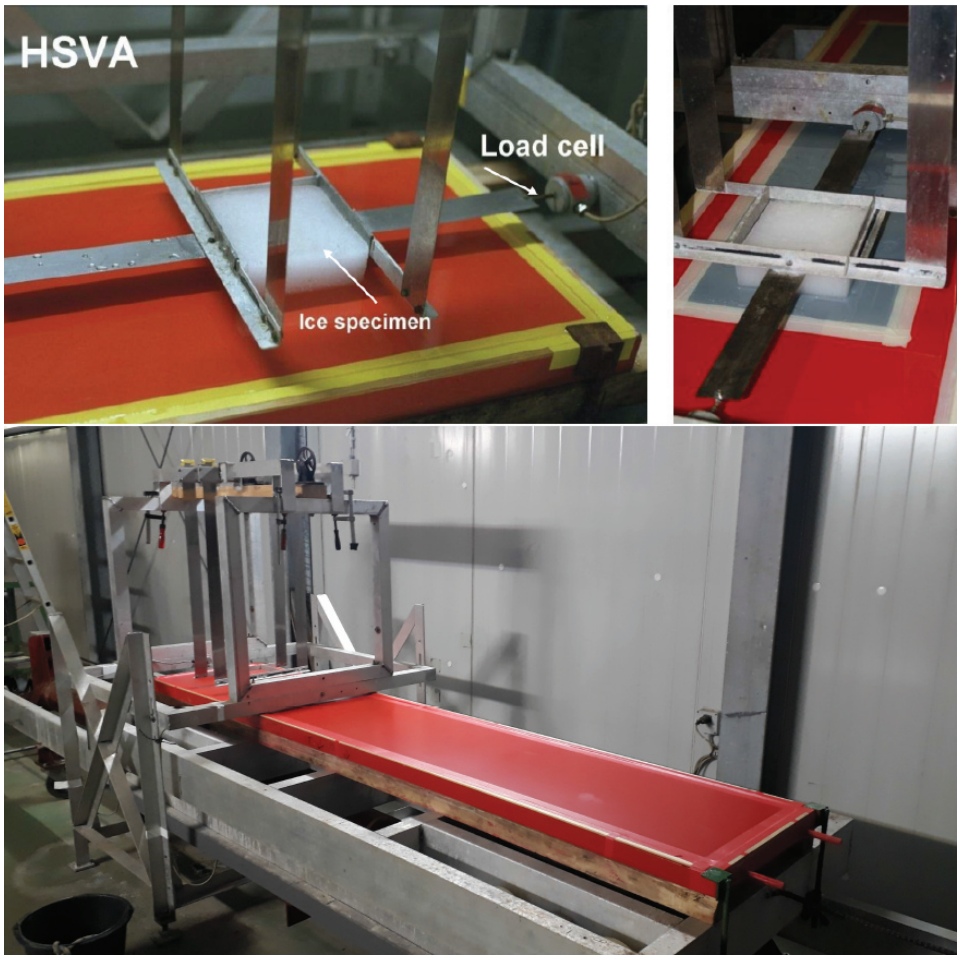

Figure 75: Photographs of the friction test apparatus

Determination of structure parameters

Stiffness at water level, dominant natural frequency of the structure, and the corresponding damping coefficient in open water condition are assessed by pullout and release tests. These tests were performed once each testing day, and repeated in case that the setup configuration was changed.
For pullout tests, an external load was applied to the model in ice drift direction close to the water surface. The load is supposed to increase steadily until the aspired load level – typically the maximum global load expected in the ice tests – is reached. This was done by connecting a towing rope by a hinge shackle at the downstream side of the model, and pulling this rope steadily with a crane. Extension coil springs connected rope and crane to transform the fast movement of the crane to a slow deflection increase at the model. This is necessary because the setup is designed for small deflections up to a maximum of 150 mm, and the load increases rapidly over deflection. Since human reaction time needs to be considered when a crane shall be manually driven to a certain load level, the duration of load increase has to be enlarged. For pullout tests, the structure is loaded by the crane, and afterwards released by the crane in the same manner. For release tests, a special shackle is inserted in the pulling rope which can be loosened manually. After releasing the shackle, the connection between crane and model breaks, and the model can oscillate freely. In both tests, the pull force is measured by an in-line uniaxial load cell connecting model and rope, and the model deflection is measured by a laser mounted in x-direction close to the water surface.
An example of load and deflection time histories of a pullout and release test is shown in Fig. 76.

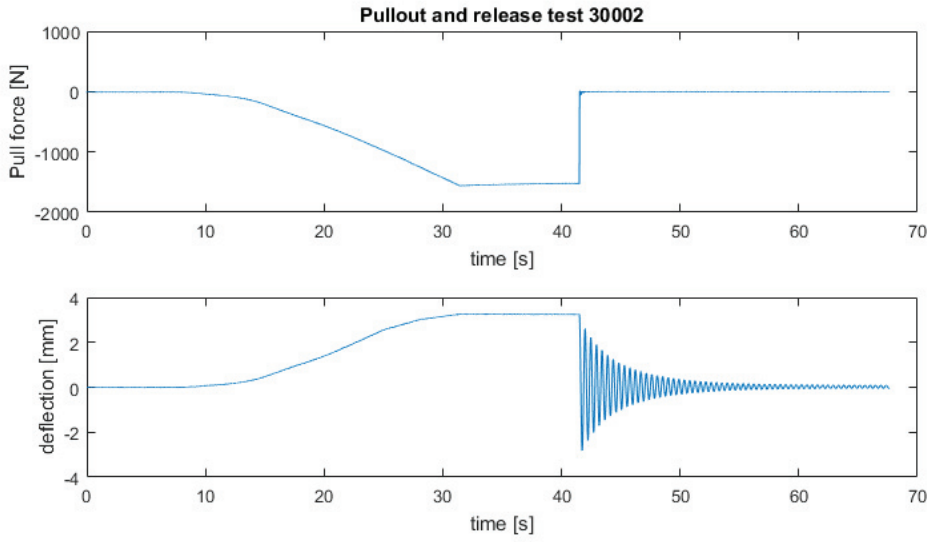

Figure 76: Time histories of load and response during pullout and release test (OW test 30002, Configuration C1)

The pullout tests revealed a linear load increase over increasing deflection (comp. Fig. 12 in Sec. 3.1.3). Hence, the stiffness values provided for each test were simply calculated by division of the load maximum applied during the pullout test by the corresponding deflection. The value is round off to the nearest 10, as the method is not expected to deliver more exact results.
The natural frequency is found by FFT of the response measurement and round off to one decimal place.
The damping as fraction of critical damping is calculated from the decaying response amplitudes:

$$\zeta = \sqrt{\left(1 + \left(\frac{2\pi N}{ln\left(\frac{s_n}{s_0}\right)}\right)^2\right)^{-1}} \tag{46}$$

The damping coefficient is in some cases not constant for the entire decay test, as the maximum deflection is a superposition of deflection of the compliant basis and additional flexibilities of the setup, e.g. bending of the model and non-rigidity of the 6-component scale. These additional, unintended flexibilities add high-frequent oscillations as their stiffness is rather high and the corresponding oscillating mass comparatively small. They are damped out quickly. Therefore, the calculation for a ζ representative for the dynamic ice-structure interaction is calculated from the time interval of the release test time history where the superimposed deflections have already decayed.

It should be noted that the resulting damping ratio is indicative, and in this study mainly serves the purpose to compare the damping in the different setups to check for comparable conditions. Hence, no exact values are needed, and the chose simplified approach is considered sufficient.

A.2. Details for all conducted test series

Phase 1

Model test setup

Series	Run	D [mm]	k [N/mm]	f_n [Hz]	ζ [%]	Shape	Configuration (deviation k [%]/ deviation f_n [%])
11000	11010, 11020, 11021, 11030, 11040, 11050	830	2230	5.45	1.5	Cylinder	C1 (+15 / -1)
12000	12010, 12011, 12020, 12030, 12040, 12050	830	2230	5.45	1.5	Cylinder	C1 (+15 / -1)
13000	13010, 13020, 13030, 13040, 13050	830	490	2.65	3.0	Cylinder	C2 (0 / 0)
14000	14010, 14020, 14030, 14040, 14050	830	490	2.65	3.0	Cylinder	C2 (0 / 0)

Measurement	Equipment
Global load on the model	6-component scale (load cell sandwich)
Local loads	3 adjacent tactile sensors type L
Acceleration of the model	Accelerometer
Acceleration of the compliant basis	Accelerometer
Deflection of the model at water level	laser transducer
Movement of the ice sheet at one specific location	Optical tracking markers (Qualisys)

Ice Properties

The properties written in brackets given in below, and all following, tables refers to a value which was not measured directly before or after a test run, but taken from the closest measurement. Due to different tempering gradients, no interpolation between property tests was made.

Run	h [mm]	σ_c [kPa]	σ_f [kPa]	ice drift speed [mm/s]
11010	49	74	63	20
11020	50	(74)	(63)	10
11021	50	(74)	(63)	10, 30
11030	51	64	64	20
11040	50	(64)	66	20, 40, 60
11050	49	78	67	40, 100, 150
12010	47	(96)	(46)	5, 20
12011	47	96	46	20
12020	48	(96)	48	30, 40
12030	48	95	48	40, 100
12040	47	120	56	40, 50, 60
12050	48	68	51	20, 30, 40, 50
13010	45	101	56	40, 50, 60
13020	46	(101)	(56)	60, 70, 100
13030	45	73	57	80, 90
13040	47	(73)	(57)	20, 30, 40, 50
13050	46	64	57	30 accelerated to 150
14010	46	131	61	10, 20, 30
14020	45	(131)	(61)	20, 30, 40, 50
14030	46	110	47	30, 32, 150
14040	47	101	73	20, 22, 24, 26, 28, 30, 32, 34, 36
14050	44	(101)	68	44, 42, 40, 38, 36, 34, 32, 30, 28

Test Runs

Load in x-dirction measured by the 6-component scale connecting model and compliant basis is presented for each test run of Series 10000 on the following pages. Note that the measured load is only indicative for the global ice load, as no inertia correction has been applied to the presented data.

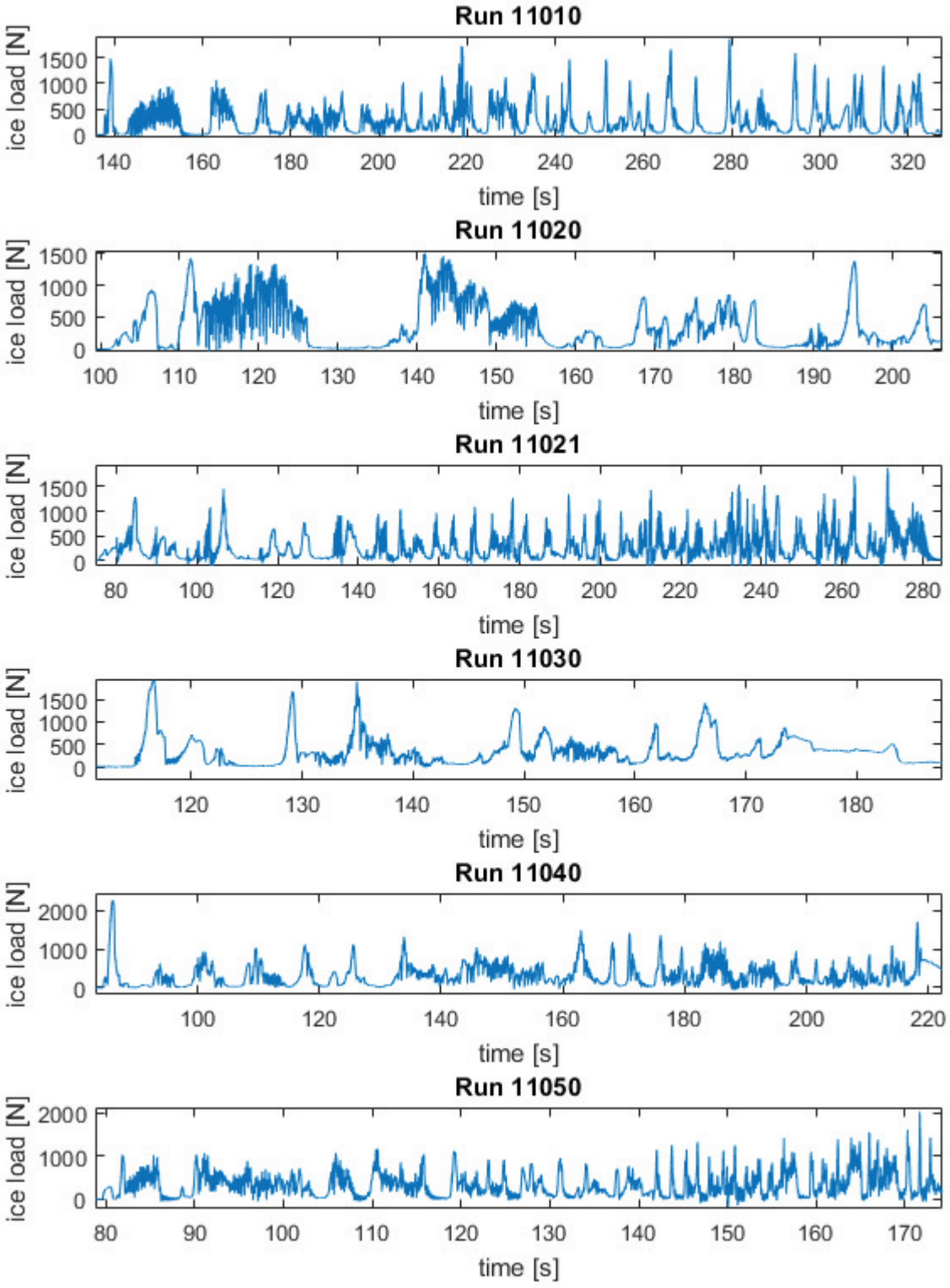
Run 11010
ice load [N]
1500
1000
500
0
140 160 180 200 220 240 260 280 300 320
time [s]
Run 11020
ice load [N]
1500
1000
500
0
100 110 120 130 140 150 160 170 180 190 200
time [s]
Run 11021
ice load [N]
1500
1000
500
0
80 100 120 140 160 180 200 220 240 260 280
time [s]
Run 11030
ice load [N]
1500
1000
500
0
120 130 140 150 160 170 180
time [s]
Run 11040
ice load [N]
2000
1000
0
100 120 140 160 180 200 220
time [s]
Run 11050
ice load [N]
2000
1000
0
80 90 100 110 120 130 140 150 160 170
time [s]

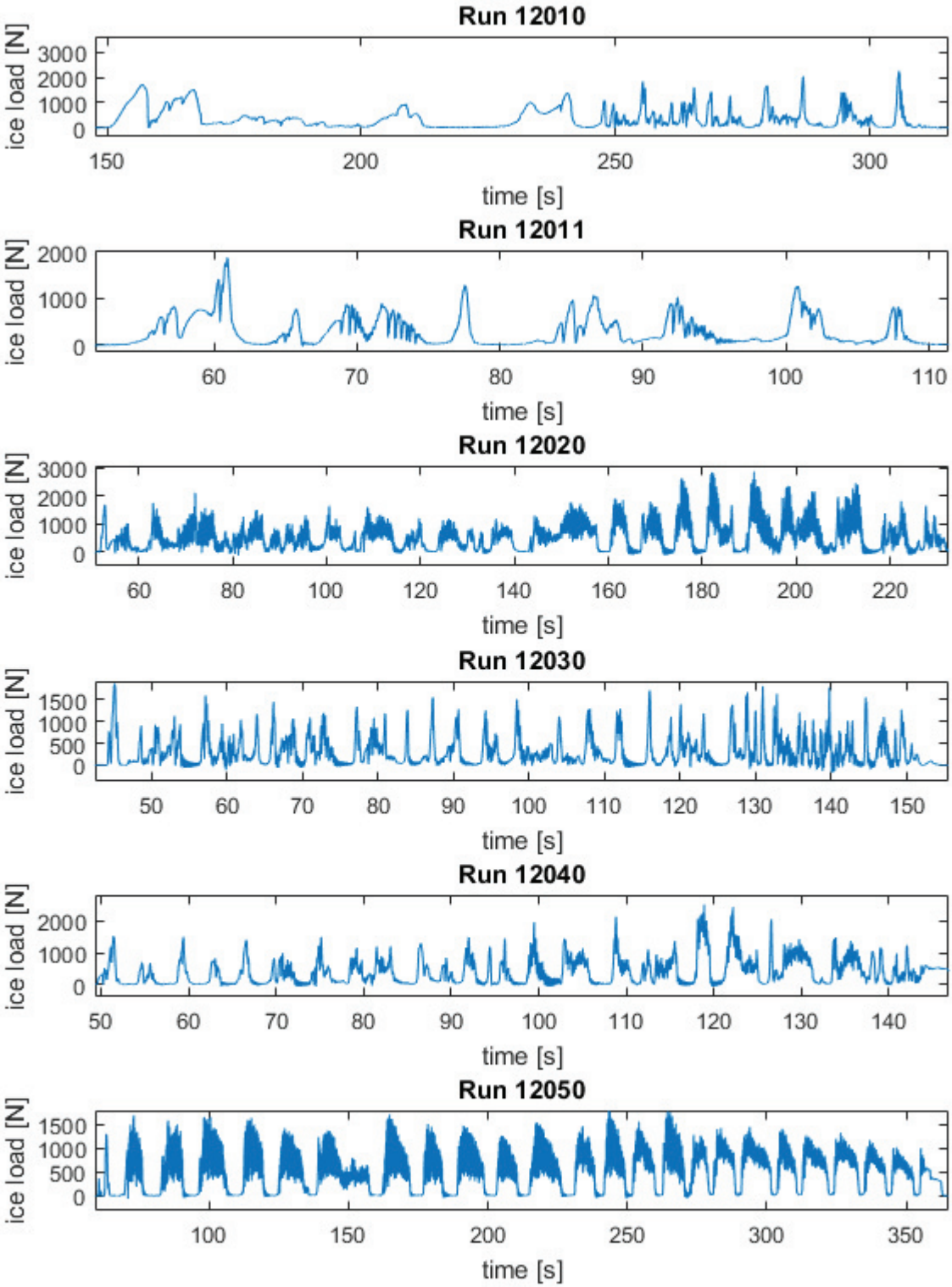
Run 12010
ice load [N]
3000
2000
1000
0
150
200
250
300
time [s]
Run 12011
ice load [N]
2000
1000
0
60
70
80
90
100
110
time [s]
Run 12020
ice load [N]
3000
2000
1000
0
60
80
100
120
140
160
180
200
220
time [s]
Run 12030
ice load [N]
1500
1000
500
0
50
60
70
80
90
100
110
120
130
140
150
time [s]
Run 12040
ice load [N]
2000
1000
0
50
60
70
80
90
100
110
120
130
140
time [s]
Run 12050
ice load [N]
1500
1000
500
0
100
150
200
250
300
350
time [s]

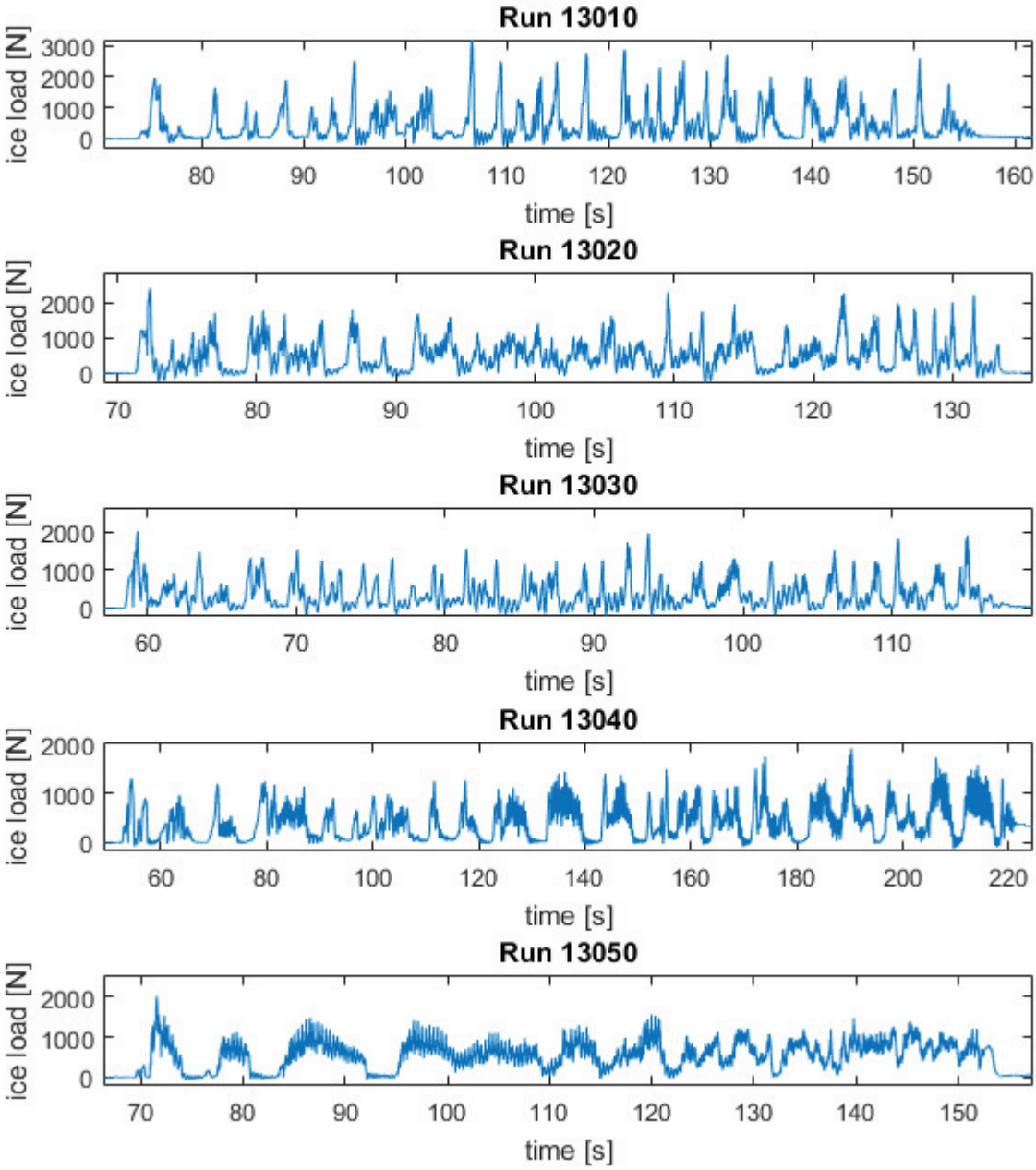
Run 13010
ice load [N]
3000
2000
1000
0
80 90 100 110 120 130 140 150 160
time [s]
Run 13020
ice load [N]
2000
1000
0
70 80 90 100 110 120 130
time [s]
Run 13030
ice load [N]
2000
1000
0
60 70 80 90 100 110
time [s]
Run 13040
ice load [N]
2000
1000
0
60 80 100 120 140 160 180 200 220
time [s]
Run 13050
ice load [N]
2000
1000
0
70 80 90 100 110 120 130 140 150
time [s]

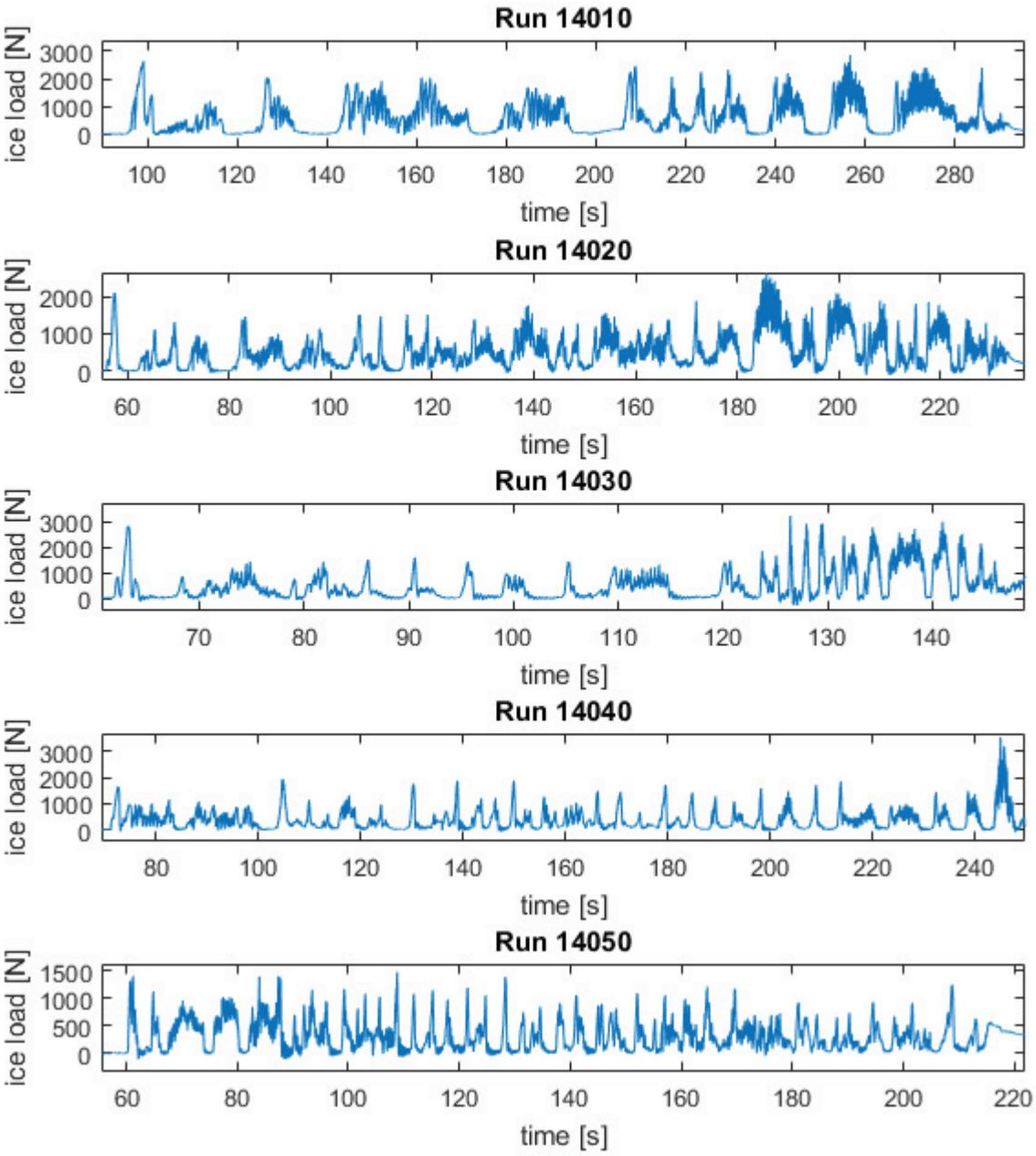
Run 14010
ice load [N]
3000
2000
1000
0
100 120 140 160 180 200 220 240 260 280
time [s]
Run 14020
ice load [N]
2000
1000
0
60 80 100 120 140 160 180 200 220
time [s]
Run 14030
ice load [N]
3000
2000
1000
0
70 80 90 100 110 120 130 140
time [s]
Run 14040
ice load [N]
3000
2000
1000
0
80 100 120 140 160 180 200 220 240
time [s]
Run 14050
ice load [N]
1500
1000
500
0
60 80 100 120 140 160 180 200 220
time [s]

Phase 2

Model test setup

Series	Run	D [mm]	k [N/mm]	f_n [Hz]	ζ [%]	Shape	Configuration (deviation k [%]/ deviation f_n [%])
21000	21010, 21011	500	2220	5.50	2.0	Cylinder	C1 (15 / 0)
	21020	500	3020	7.60	2.9	Cylinder	C3 (-17 / 6)
22000	22010	200	1910	5.70	2.9	Cylinder	C1 (-1 / 4)
22100	22110, 22120	200	1960	5.70	2.9	Cylinder	C1 (1 / 4)
23000	23010	200	1930	5.80	2.4	Cylinder	C1 (0 / 5)
	23020	500	2030	5.80	1.7	Cylinder	C1 (5 / 5)
24000	24010	120	1935	5.40	1.0	Cylinder	C1 (0 / -2)
25000	25010, 25011	200	1290	4.2	1.8	flat indenter	C1 (-33 / -24)
26000	26010	200	1915	5.60	2.2	corner-first	C1 (-1 / 2)
26000	26020	200	1950	5.40	1.7	flat indenter	C1 (1 / -2)
27000	27010	120	4300	6.80	1.0	cylinder	C3 (17 / -6)
27000	27020, 27030	120	2770	5.30	1.0	cylinder	C1 (43 / -4)

Measurement	Equipment
Global load on the model	6-component scale (load cell sandwich)
Local loads	1 to 2 adjacent tactile sensors type L, 1 sensor type D
Acceleration of the model	Accelerometer
Acceleration of the compliant basis	Accelerometer
Acceleration of the main carriage (rigid support structure)	Accelerometer
Deflection of the model at water level	laser transducer

Ice Properties (MI)

Run	h [mm]	σ_c [kPa]	σ_f [kPa]	ice drift speed [mm/s]
21010	(31)	(90)	(62)	6, 10
21011	31	90	62	16, 20, 25, 30, 35, 40, 45, 50, 60, 70, 100
21020	31	(90)	53	6, 7, 8, 10, 20, 30, 40, 50, 60, 70, 80, 90, 100
22120	81	103	32	6, 7, 9
22010	71	185	65	5, 6
23010	42	97	45	5, 7, 8, 10, 16, 20, 30, 40, 50, 70, 100, 150
23020	41	72	45	6, 7, 9, 10, 16, 21, 31, 41, 51, 71, 100
24010	41	136	69	3, 4, 5, 6, 7, 8, 9, 10, 11, 12, 13, 14, 15, 16, 17, 18, 19, 20, 21, 22, 23, 24, 25, 26, 27, 28, 29, 30, 31, 32, 33, 34, 35, 36, 37, 38, 39, 40, 41, 42, 43, 44, 45, 46, 47, 48, 49, 50, 53, 54, 55, 56, 57, 58, 59, 62, 65, 67, 70, 74, 79, 85, 89, 94, 99, 105, 107, 120, 128, 139, 148, 159, 168, 178, 190, 192
25010	48	145	60	5, 7, 9, 11, 13, 15, 17, 19, 20 ,21, 22, 23, 24, 25, 26, 27, 28, 29, 30, 31, 32, 33, 34, 35, 36
25011	48	115	58	40, 41, 42, 43, 44, 50, 55, 60, 64, 70, 75, 80, 84, 90, 95, 100, 110, 120, 130, 140, 150
26010	44	110	60	3, 5, 6, 7, 8, 9, 10, 15, 20, 30, 40, 50, 70, 100
26020	45	(110)	(60)	13, 14, 15, 16, 17, 18, 19, 20, 21, 22, 23, 24, 25, 26, 27, 28, 29, 30, 31, 32, 33, 34, 35, 36, 37, 38, 39, 40, 41, 42, 43, 44, 45, 46, 47, 48, 49, 50, 51, 52, 60, 69, 80, 100, 150

Ice Properties (ICMI)

Run	h [mm]	σ_c [kPa]	σ_f [kPa]	ice drift speed [mm/s]
27010	34	630	140	3, 4, 5, 6, 7, 8, 9, 10, 11, 12, 13, 14, 15, 16, 17, 18, 19, 20, 21, 22, 23, 24, 25, 26, 27, 28, 29, 30, 31, 32, 33, 34, 35, 36, 37, 38, 39, 40, 41, 42, 43, 44, 45, 46, 47, 48, 49, 50, 51, 52, 53, 54, 55, 56, 57, 58, 59, 60
27020	34	520	130	5, 10, 20, 30, 40, 50, 60, 70, 80, 90, 100, 150, 200
27030	42	400	80	5, 10, 20, 30, 40, 50, 60, 70, 80, 90, 100, 145, 150, 200

Test Runs

Load in x-dirction measured by the 6-component scale connecting model and compliant basis is presented for each test run of Series 20000 on the following pages. Note that the measured load is only indicative for the global ice load, as no inertia correction has been applied to the presented data.
Runs 24010, 25010, 26010, 26020 and 27020 have been stopped and resumed when the storage capacity of the TAC system had been exceeded.

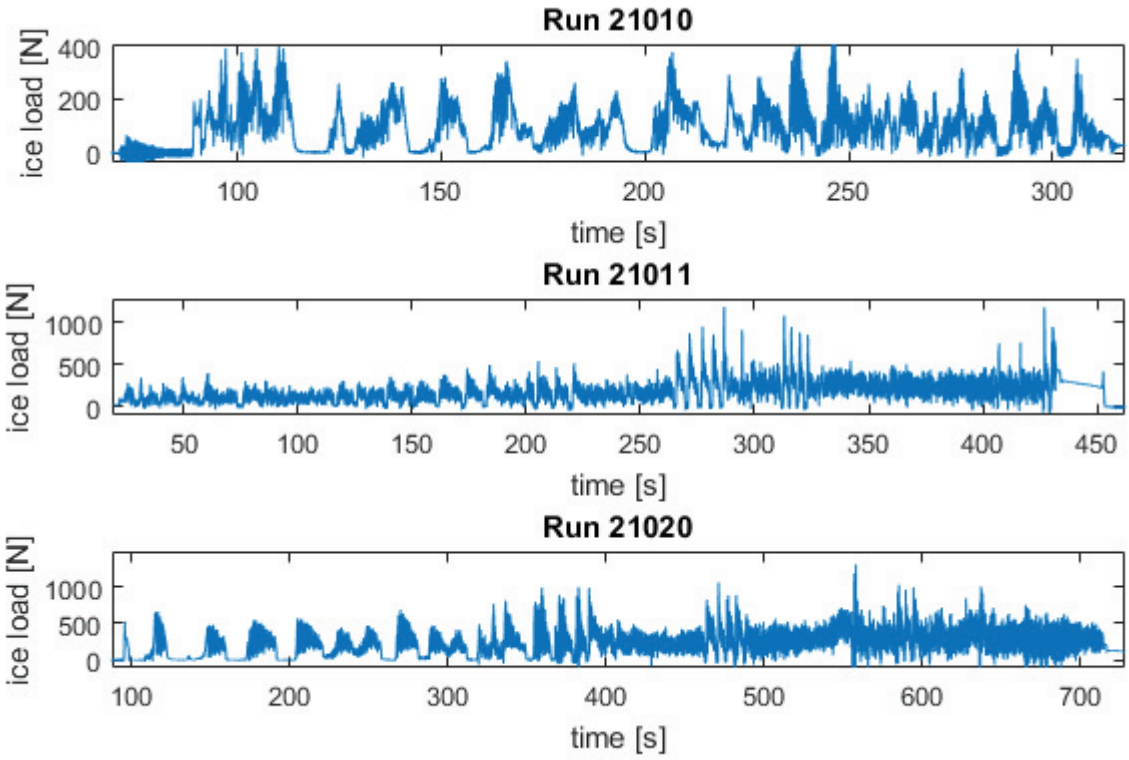
Run 21010
ice load [N]
400
200
0
100
150
200
250
300
time [s]
Run 21011
ice load [N]
1000
500
0
50
100
150
200
250
300
350
400
450
time [s]
Run 21020
ice load [N]
1000
500
0
100
200
300
400
500
600
700
time [s]

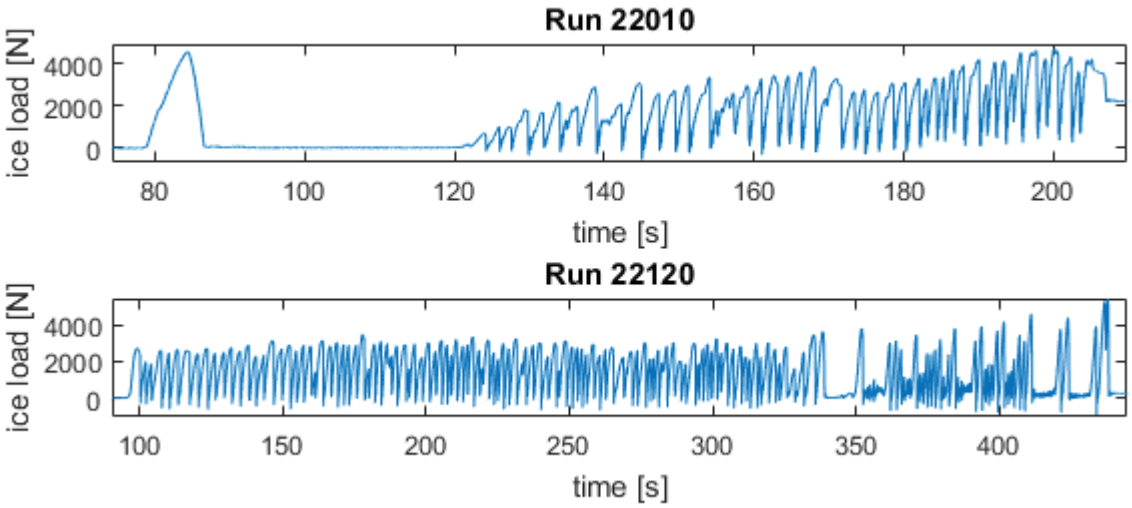
Run 22010
ice load [N]
4000
2000
0
80
100
120
140
160
180
200
time [s]
Run 22120
ice load [N]
4000
2000
0
100
150
200
250
300
350
400
time [s]

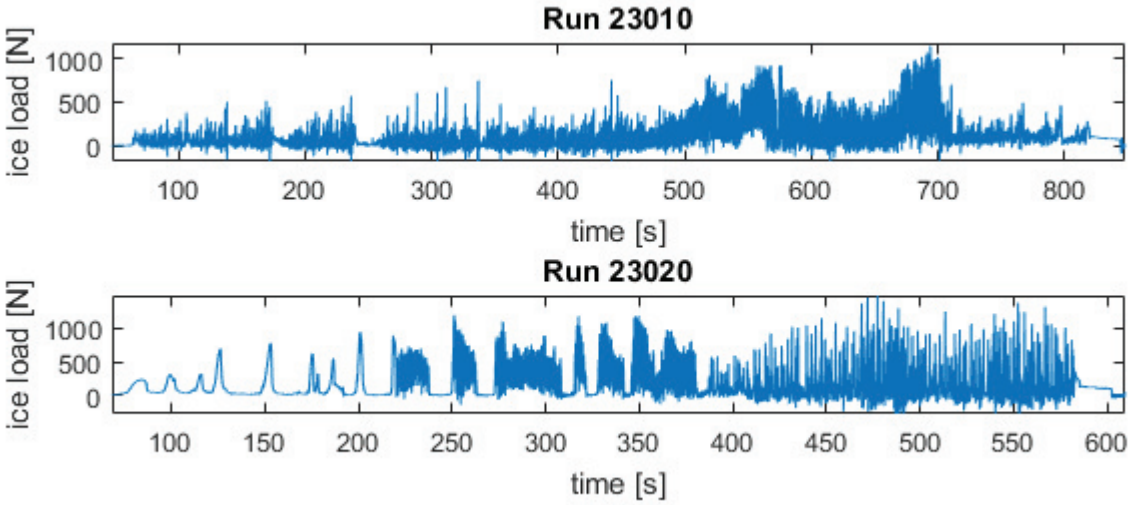
Run 23010
ice load [N]
1000
500
0
100
200
300
400
500
600
700
800
time [s]
Run 23020
ice load [N]
1000
500
0
100
150
200
250
300
350
400
450
500
550
600
time [s]

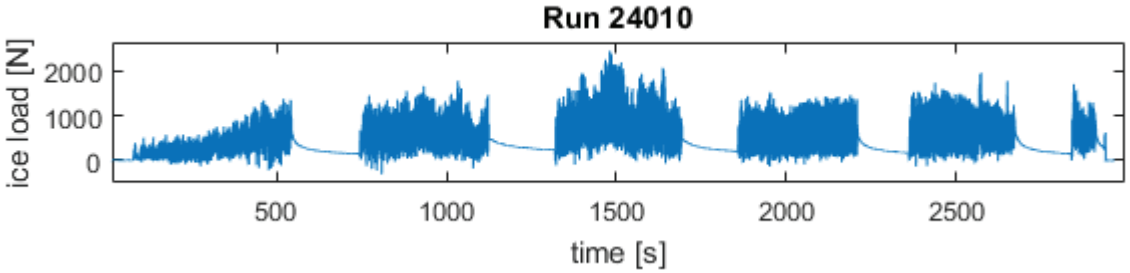
Run 24010
ice load [N]
2000
1000
0
500
1000
1500
2000
2500
time [s]

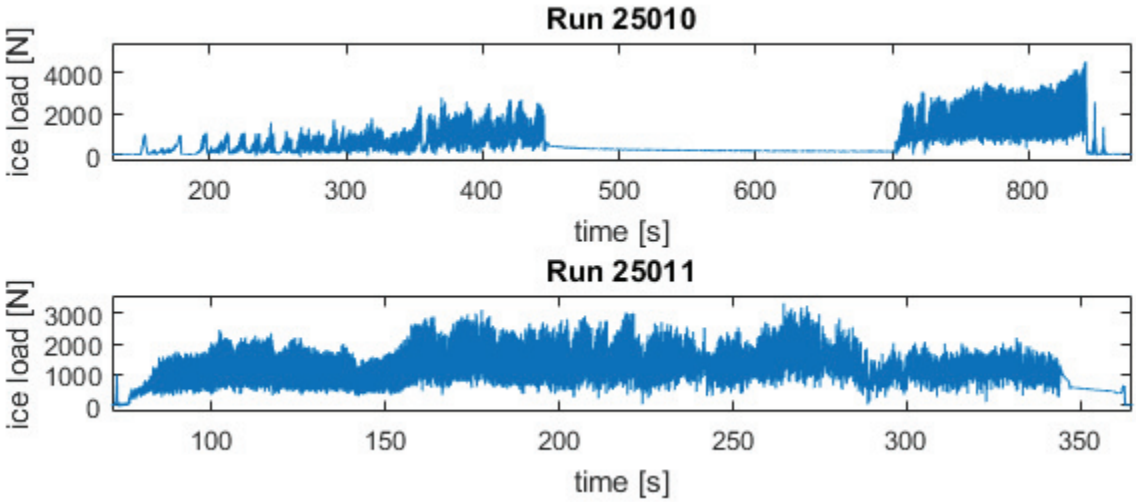
Run 25010
ice load [N]
4000
2000
0
200
300
400
500
600
700
800
time [s]
Run 25011
ice load [N]
3000
2000
1000
0
100
150
200
250
300
350
time [s]

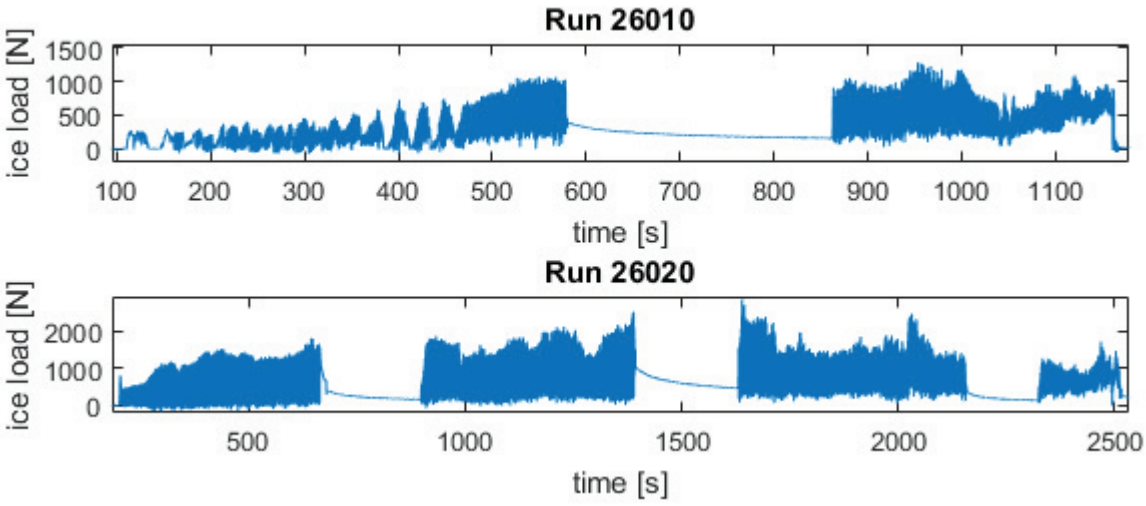
Run 26010
ice load [N]
1500
1000
500
0
100 200 300 400 500 600 700 800 900 1000 1100
time [s]
Run 26020
ice load [N]
2000
1000
0
500 1000 1500 2000 2500
time [s]

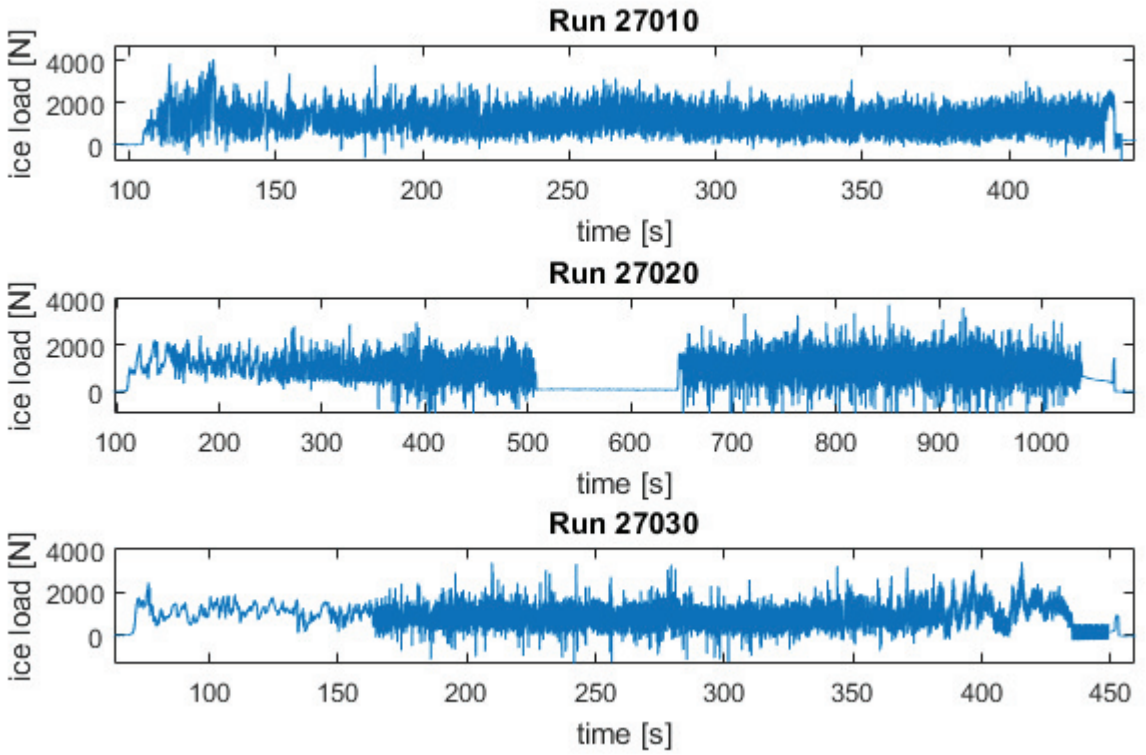
Run 27010
ice load [N]
4000
2000
0
100 150 200 250 300 350 400
time [s]
Run 27020
ice load [N]
4000
2000
0
100 200 300 400 500 600 700 800 900 1000
time [s]
Run 27030
ice load [N]
4000
2000
0
100 150 200 250 300 350 400 450
time [s]

Phase 3

Model test setup

Series	Run	D [mm]	k [N/mm]	f_n [Hz]	ζ [%]	Shape	Configuration (deviation k [%]/ deviation f_n [%])
31000	31010 31030, 31050	120 120	378 1910	2.15 5.18	2.8 1.8	flat indenter flat indenter	C2 (-23 / -19) C1 (-1 / -6)
32000	32020, 32030, 32040	120	1910	4.4	1.0	cylinder	C1 (-1 / -6)

Measurement	Equipment
Global load on the model	6-component scale (load cell sandwich), only load cells in horizontal plane active to avoid overload
Local loads	1 sensor type D
Acceleration of the model	Accelerometer
Acceleration of the compliant basis	Accelerometer
Acceleration of the model's base plate (location of second laser transducer)	Accelerometer
Deflection of the model at water level	laser transducer
Deflection of the model at base plate	laser transducer

Ice Properties

Run	h [mm]	σ_c [kPa]	σ_f [kPa]	ice drift speed [mm/s]
31010	47	131	56	5, 10
31030	51	(131)	(56)	5, 10, 15, 20, 24, 30, 35, 40, 45, 50, 55, 60, 65, 70, 75, 80, 85, 90, 95, 100, 105, 110, 115, 120, 130, 137, 150, 200
31050	50	130	56	25
32020	70	175	55	20, 50, 95
32030	81	(175)	(55)	5, 10, 15, 20, 25, 30, 35, 40, 45, 50, 55, 60, 65, 70, 75, 80, 85, 90, 95, 100, 150
32040	81	(175)	(55)	200

Test Runs

Load in x-dirction measured by the 6-component scale connecting model and compliant basis is presented for each test run of Series 30000 on the following pages. Note that the measured load is only indicative for the global ice load, as no inertia correction has been applied to the presented data.
Run 31010 has been stopped and resumed when the storage capacity of the TAC system had been exceeded.

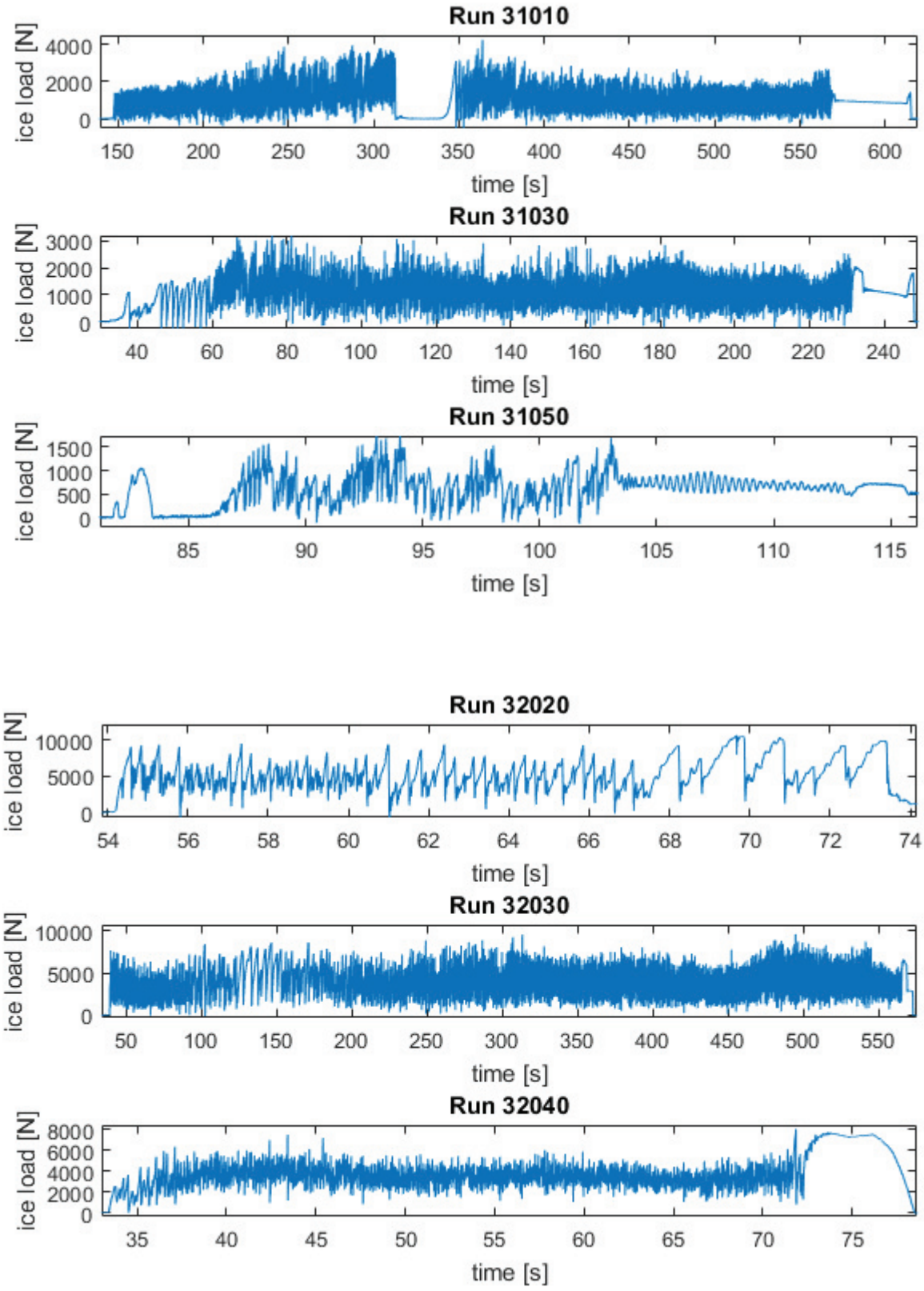
Run 31010
ice load [N]
4000
2000
0
150
200
250
300
350
400
450
500
550
600
time [s]
Run 31030
ice load [N]
3000
2000
1000
0
40
60
80
100
120
140
160
180
200
220
240
time [s]
Run 31050
ice load [N]
1500
1000
500
0
85
90
95
100
105
110
115
time [s]
Run 32020
ice load [N]
10000
5000
0
54
56
58
60
62
64
66
68
70
72
74
time [s]
Run 32030
ice load [N]
10000
5000
0
50
100
150
200
250
300
350
400
450
500
550
time [s]
Run 32040
ice load [N]
8000
6000
4000
2000
0
35
40
45
50
55
60
65
70
75
time [s]

B. Tactile sensor application in ice model tests

Tactile sensors are a common implement in several fields of physical testing and research, for example in robotics, medical applications, civil engineering and many more [87]. Amongst the first researchers who used such sensors in ice interaction testst were Izumiyama et al., who systematically studied the applicability of tactile sensors for ice-structure indentation tests [33]. They found that tactile sensors can be a good tool for ice engineering researchers. However, they also pointed out some shortcomings of the sensors: In their tests, the trend between registered raw data and actually applied load was non-linear, and the registered load depended on the size of the loaded area. Further early tests have been performed by Sodhi et al. [83] who found a satisfactory match between the loads registered by a tactile sensor and the load obtained from a parallel measurement of a load cell mounted behind the plate holding the tactile sensor. Despite these early successful campaigns, tactile sensors have not yet become standard measurement system in ice model tests. The main reason for a general reservation towards this technique may partly stem from the fact that tactile sensors were not made for the cold and wet environment, and have additional restrictions which are summarized below. The described methods and measures have been established in the course of the present study and earlier tests [2, 107].

Utilization of tactile sensors in wet and cold environment

Tactile sensors are designed for pressure measurement in normal to hot temperatures, and dry surrounding [87]. Sensors of Type L (5260) contain ventilation holes which have to be sealed before application in the basin. The ventilation holes are included in all larger sensors to avoid destruction of the sensor when a large area is instantaneously loaded, and the air between the two sensor layers needs to redistribute within short time. Since such load cases are not expected for the considered ice-structure interaction tests, integrity of the large sensors is not put at risk when the holes are sealed. A silicone sealing and adhesive tape for protection of the silicone are used. Sensors are loaded during sealing to reduced the amount of trapped air inside the sensor. Remaining air can become visible during the tests as increased amount of noise in unloaded sensor regions. Sensor D does not contain ventilation holes and can be applied without sealing.

The thin plastic cover of the sensor layers is vulnerable to ice abrasion and needs further protection. For the presented tests, three types of covers were considered as protection against water intrusion and ice abrasion: 0.05 mm adhesive plastic foil with a similar friction coefficient as HSVA's standard ice paint (μ=0.1), 0.5 mm elastic window protection film (both PET material), and 0.5 mm aluminium sheet. Such aluminium sheet has been used by Määttänen et al. [56] for ice model tests with tactile sensors. The PET solutions are investigated as they provide easier and shape-independent application, and their transparency enables to see the sensor itself during tests.
During pre-tests, it was found that the thicker PET cover and the aluminium sheet are difficult to attach without gaps between sensor and cover. Such gaps may significantly

influence the measurements if water or ice gets trapped between sensor and cover. However, the cover gets pushed against the sensor during continuous interaction with ice, and the influence disappears.
Results from a simple test for spatial accuracy of load transmission are compiled in Tab. 17. Sensor 5260 was successively covered with the three cover types, and three loading cases were tested for each cover. In the first two tests, 5 kg weights were put on the laser, with smooth pieces of wood with 5.1 and 65 cm^2 area put between weight and sensor. For the last test, a single sensel was manually loaded using a metal bar. In fact, the loaded area in this case was smaller than the sensel, but of course the sensor cannot resolve such a small loaded area. Results show that the aluminium sheet significantly redistributes the load over several, in fact unloaded, additional sensels. The thin PET cover performs slightly better than the thicker one.

The cold working environment has an effect on the resistance measured in the circuits. Bechthold et al. [2] found a temperature dependence of more than 5% between tests at room temperature and in 0°C ice laboratory. Ruckert [71] studied this influence systematically and found a load difference of 15% between measurements at 20°C and -10°C. This demands for calibration of the sensor at test temperature, which is about 0°C. The sensor is partly submerged, therefore room and water temperature have an effect. Room temperature is typically targeted as +4°C throughout the test day, so that the difference in water and room temperature is small. The model is stored in the trimtank area of the LIMB between test series, preventing large variations of surrounding temperature to avoid temperature gradients during testing.
The influence of temperature on the resistance of the sensors is one of the reasons why post-test calibration with a redundant measuring system was chosen. With such calibration, the temperature effect is inherently considered and does not need to be assessed individually. Further reasons for post-test calibration are discussed below. The post-test calibration procedure is documented in Sec. 3.3.2.

Influence of friction, normal and shear forces

Tactile sensors are designed to record normal pressure. If shear forces are applied, these are in the best case neglected, and in the worst case they influence the measured normal pressure if shear adds resistance between the circuits. To avoid the second case, friction should be kept at a low level.
The best case for the tactile sensor is a flat indenter, where the applied load can be assumed to act mainly normal to the structure surface facing the ice. However, even this case is influenced by shear forces, as the broken ice is transported towards the sides and around the structure. When a cylindrical structure is used, measured normal loads become less reliable towards the sides. Still, it can be assumed that the highest pressure will remain in normal direction to the structure surface, thus recorded loads at the sides of the structure are still physically meaningful. However, their accuracy will be affected by missing shear forces.
When tactile measurements are compared to parallel measurements of a conventional

Type of protection foil	Actually loaded area [cm^2]	Recognized loaded area [cm^2]	Error [%]
0.05 mm adhesive plastic foil	5.1	8.3	63
0.5 mm plastic sheet	5.1	10.2	100
0.5 mm aluminum sheet	5.1	16.5	123
0.05 mm adhesive plastic foil	65	70	8
0.5 mm plastic sheet	65	72	11
0.5 mm aluminum sheet	65	76	17
0.05 mm adhesive plastic foil	1 sensel	1 sensel	0
0.5 mm plastic sheet	1 sensel	1 sensel	0
0.5 mm aluminum sheet	1 sensel	6 sensel	500

Table 17: Comparison of different tactile sensor cover solutions

load transducer, it can be seen that the global load can be captured well even on a cylinder. However, the accuracy of the calibration decreases for cylinders compared to a flat indenter.

Sensitivity adjustment

The IScan software translates the resistance in a sensel to a raw pressure unit using 8 bit conversion, meaning that the dynamic range of the measured signal can be resolved in 255 pressure levels. However, the lowest level is always set to zero pressure, and a software in-built minimum threshold of 3 is applied, which further restricts the pressure level resolution. Calibration is required to calculate the actual pressure from the raw data. In order to achieve highest possible accuracy, the measuring range has to be thoroughly adjusted to the actual pressure range expected in the tests. If the sensitivity is set too low, raw pressure of 255 relates to a value far beyond the actual pressures, and the resolution of measured pressures is low. On the contrary, clipping occurs if the sensitivity is set too high, as single sensels become oversaturated and show a raw pressure of 255 although the actual pressure may be significantly higher. An example is shown below (from Bechthold et al. [2]). Therein, the sensitivity is set too low in the top picture, resulting in poor resolution of the actual pressure levels across the interaction area. On the contrary, sensitivity is set too high for the bottom picture, hence the total load is underestimated, and information on pressure differences in the oversaturated areas is lost. The center picture shows a good sensitivity setting. Although not reflected in Fig. 77, too low sensitivity can also result in underestimation of the contact area: The IScan software has an in-built threshold of raw pressure = 3 for noise attenuation. Hence, the threshold is also sensitivity-dependent, and low pressures are ignored if the

sensitivity is set too low.

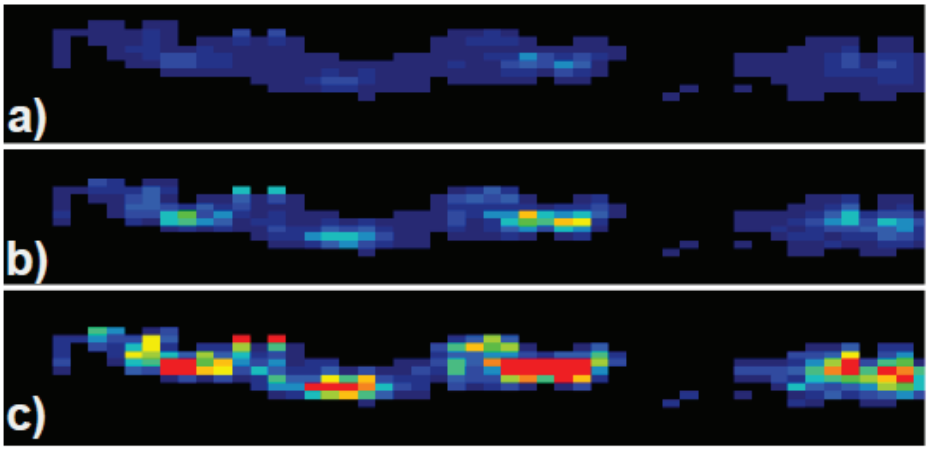

Figure 77: Illustration of too low (a), too high (c) and proper (b) sensitivity setting

Rise time effect

An often discussed downside of the tactile sensors in the ice engineering community is the rise time of the sensels. *Rise time* describes the duration it takes for a sensel to reach its actual current value due to inertia of the electrical system. If a static load is promptly applied to a tactile sensor, it takes some time until the sensor displays a constant load, i.e. for dynamic pressure it exhibits a low pass filter characteristic. Thus, if the load is short-termed, it vanishes before the sensor recognizes its actual magnitude. Tekscan states that their sensors typically have a rise time of 0.1 to 0.3 s, and dynamic calibration should be applied if shorter loads are expected [87]. It should be noted that the common criticism against tactile sensors, stating that they are not able to record short impact loads due to their rise time, is not true. Whether or not a high-frequency load is recognized at all by the sensor is not affected by the rise time, but the *response time*. The response time of the sensors is given by the manufacturer as about 5 μs. Hence, frequencies up to 20 Hz dominating the load spectrum in ice crushing are clearly registered by the sensor, but their amplitude may be underestimated due to the rise time effect.
A fundamental issue inferred by the rise time issue is its low pass filter effect depending on the calibration. If the measurement is calibrated using low frequency forces, high frequency loads will be filtered and thus underestimated, or vice versa. Therefore, the overall accuracy suffers if the actual load spectrum contains high frequency and low frequency force components at the same time. Force time histories of intermittent crushing are for example dominated by low frequency load increase, resulting in comparably low calibration factors. Still, the load increase in individual sensels can be quite fast during global collapse due to successive failure of the ice across the contact. The local load peaks are underestimated if the global load preceding the peak is used for calibration.

The global load during continuous crushing is mainly a superposition of high frequency local loads. Using the global peaks for calibration therefore results in a better representation of local load levels. The calibration factor for crushing can be up to two times larger than for intermittent crushing due to the described effects (compare Fig. 27).

Internal stress and equilibration

Tekscan recommends to use an equilibration procedure before tests. Equilibration means that a uniform pressure is applied to the sensor. An in-built function in the IScan software then applies individual stress factors to all sensels to reflect the uniform pressure distribution. According to the manufacturer, equilibration is needed as sensels may be pre-stressed due to the production process, or show wear effects after some application. In fact, it has been found that the equilibration procedure shows the waterline area of preceding tests if a used sensor is utilized. Therefore, equilibration is essential to obtain correct results. An example of sensor response to uniform load application with and without equilibration is shown in Fig. 78. However, it should be noted that equilibration requires the sensor to be put in an equilibration device. Therefore, the equilibration cannot be done with the sensor in its final condition used for the tests. Application of the protection foil and installation on the test structure is expected to add additional internal stress, which cannot be fully assessed. Stress visible on the sensor before start of ice tests is zeroed.

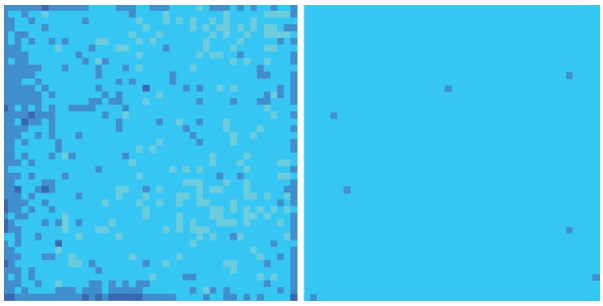

Figure 78: Sensor 5101 under uniform pressure, before (left) and after (right) equilibration

Post-test calibration

Above considerations demand for individual calibration for each test run instead of pre-calibrated sensors. Exemplary calibration results are shown for Run 25010 in Tab. 18. The importance of proper post-calibration is illustrated by a comparison of derived calibration coefficients throughout the test campaign: The sensitivity settings for all test runs and respective calibration coefficients are given in Fig. 79 and summarized in Tab. 19. In the table, the presented coefficients are mean values of the individual calibration coefficients for each tested velocity within the same run. The standard deviation therefore gives an impression of the calibration factor variability over the test velocities,

Carriage velocity [mm/s]	**Linear calibration factor**	**Coefficient of Determination R^2**	**Cross-correlation factor**
3	0.369	0.963	0.987
5	0.460	0.942	0.983
7	0.396	0.926	0.986
9	0.449	0.925	0.984
11	0.405	0.923	0.971
13	0.314	0.898	0.977
15	0.444	0.947	0.985
17	0.446	0.972	0.990
19	0.442	0.921	0.992
20	0.455	0.922	0.992
21	0.448	0.904	0.991
22	0.429	0.940	0.992
Mean	0.414	0.931	0.986
Standard deviation	0.049	0.022	0.007

Table 18: Exemplary calibration results for each velocity tested in Run 25010 (flat indenter)

which is illustrated by the markers in the corresponding figure. The large variation of calibration factors between different test runs with the same sensitivity setting underlines the influence of temperature, contact area and shape on the measurement.
Most tests show a clear velocity effect, reflecting the changing failure and contact development over different crushing regimes. However, the scatter between calibration factors is even within the same test run, and the same type of interaction, large. It should be emphasized that such change of calibration factors within the same run must base on physical changes of the interaction, as environmental conditions are similar throughout the tests. Such changes could stem from a change of direction and amount of crushed ice transportation, differing shares of slow and fast varying load components, change in stiffness or compliance of the ice sheet, or other unknown effects.

Evaluation of tactile sensor applicability for tests on ice-structure interaction

Above explanations show some shortcomings of the tactile sensors, partly stemming from their basic functionality, and partly from the fact that they are used outside their specified operating field.
Applications in ice engineering have shown that valuable insight can be drawn from tactile sensor application, but results have to be interpreted cautiously. The resulting pressures and area are influenced by the sensor type and calibration procedure. Figure 80

Run	sensitivity	calibration factor	
		mean	standard deviation
21011	S-40	0.262	0.029
21020	S-40	0.292	0.055
22120	S-40	0.633	0.040
23010	S-40	0.654	0.177
23020	S-40	0.207	0.023
24010	S-40	0.560	0.376
25010	S-35	0.414	0.049
25011	S-35	0.538	0.048
25012	S-35	0.391	-
26010	S-35	0.321	0.059
26020	S-35	0.508	0.075
27010	S-25	1.220	0.325
27020	S-25	1.591	0.540
27030	S-25	2.720	0.702
31030	S-29	1.159	0.434
31050	S-29	1.205	-
32020	S-20	0.517	0.006
32030	S-20	0.694	0.139
32040	S-20	0.674	-

Table 19: Summary of tactile sensor calibration factors

shows how local high pressure zones disappear when the sensels are too large. It illustrates how results may depend on the choice of tactile sensor. With reference to the studied tests, it was found that the resolution of Sensor L was not sufficient to capture the area increase during build-up phase in FLI. Therefore, the measurements indicate a pressure increase as main source of additional force transferred from the ice onto the structure. Only additional measurements with Sensor D revealed the considerable increase in contact height accompanying the pressure increase.
Concerning uncertainties in calibration and non-normality of load, it should be noted that the absolute pressure values are not of greatest importance for the core results. The clear trend of contact area development in IC and FLI and simultaneous pressure build-up after global failure stop in FLI is independent of absolute pressure.

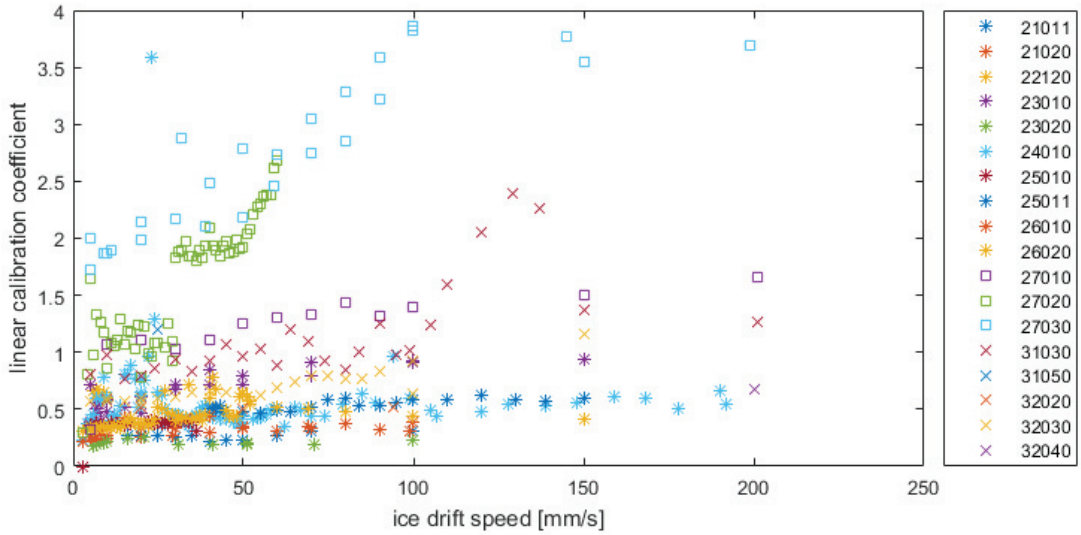

Figure 79: Individual tactile sensor calibration factors for each tested velocity per test run

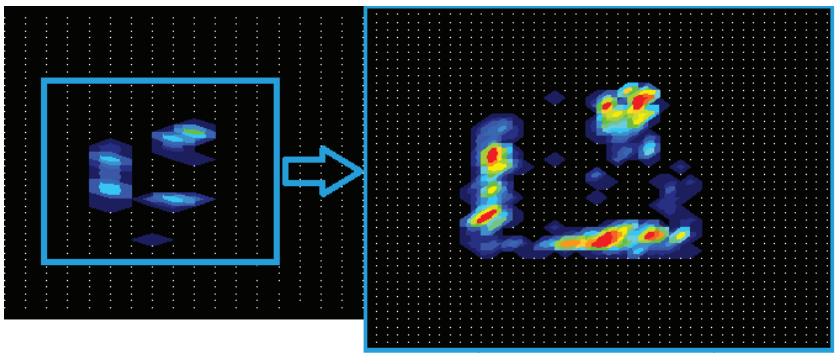

Figure 80: Local load measurement on Sensor L (left) and super-positioned Sensor D (right)

C. Further analysis results

C.1. Details of comparative investigation of IC, FLI and CC events

Identified clear IC, FLI and CC events for analysis

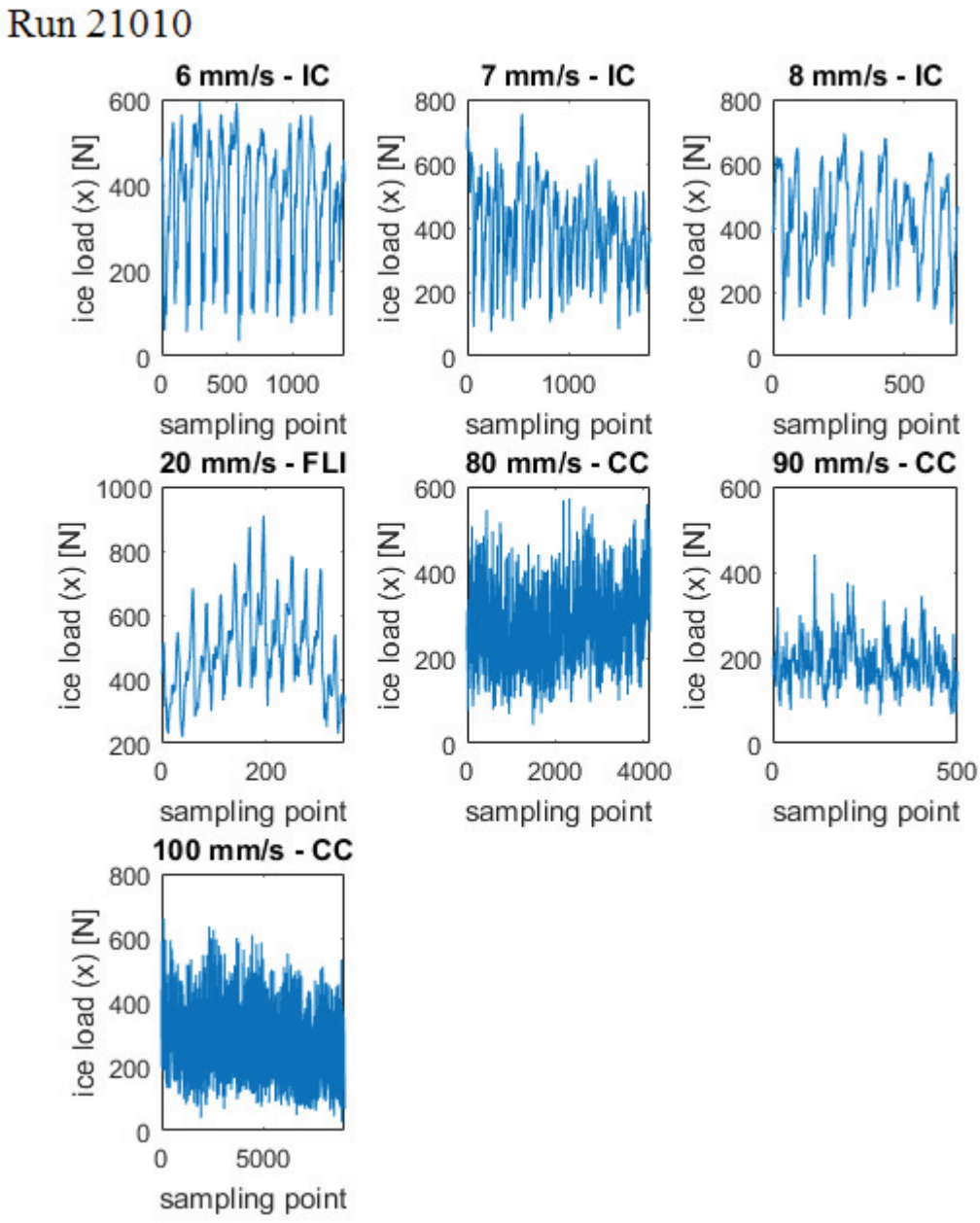

Run 23020

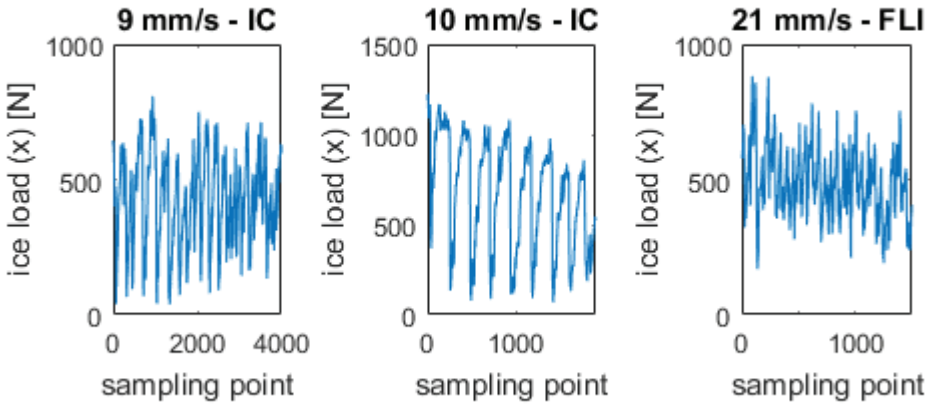
9 mm/s - IC
10 mm/s - IC
21 mm/s - FLI
ice load (x) [N]
sampling point
1000
500
0
2000
4000
1500

Run 24010

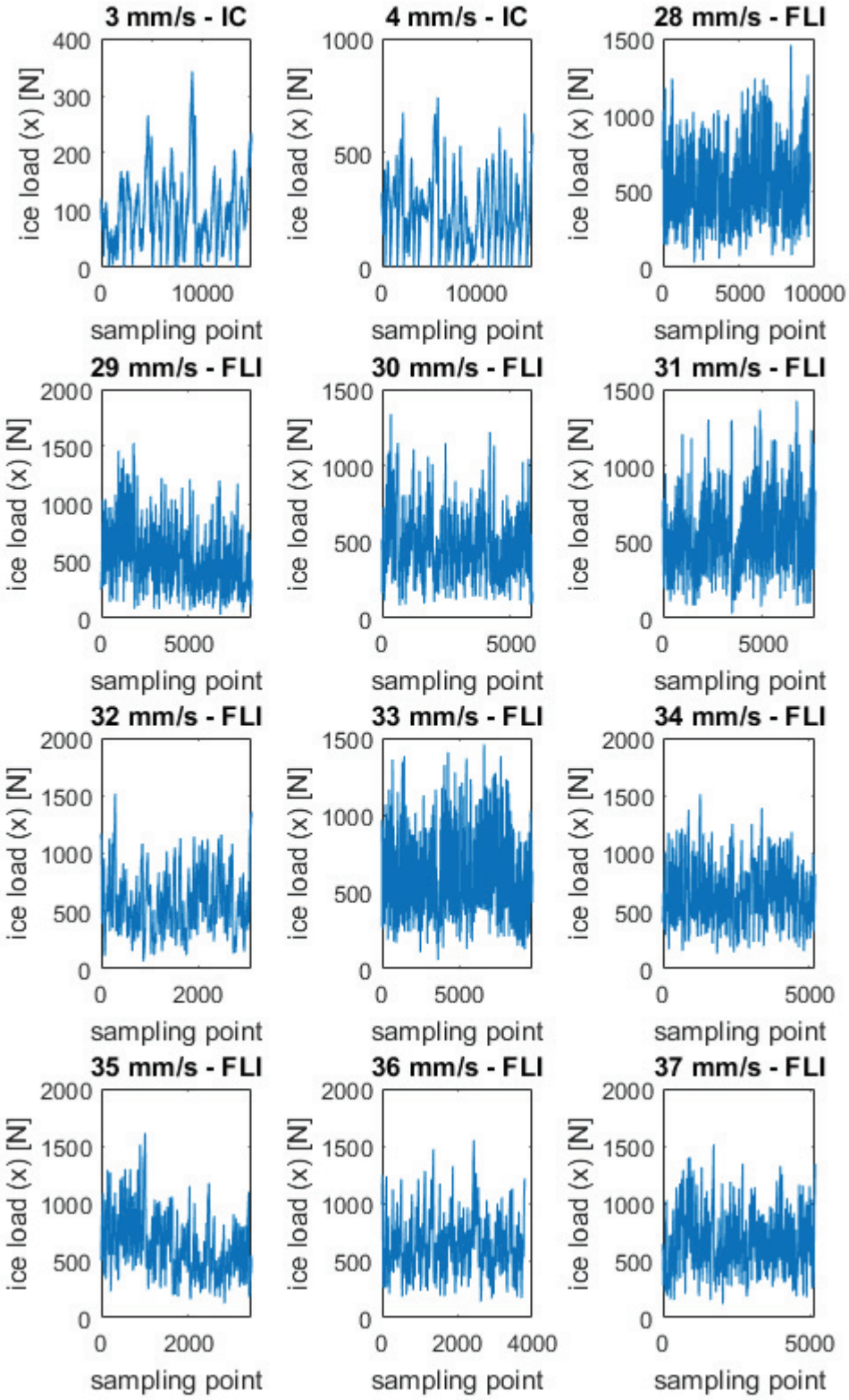
3 mm/s - IC
4 mm/s - IC
28 mm/s - FLI
29 mm/s - FLI
30 mm/s - FLI
31 mm/s - FLI
32 mm/s - FLI
33 mm/s - FLI
34 mm/s - FLI
35 mm/s - FLI
36 mm/s - FLI
37 mm/s - FLI
ice load (x) [N]
sampling point

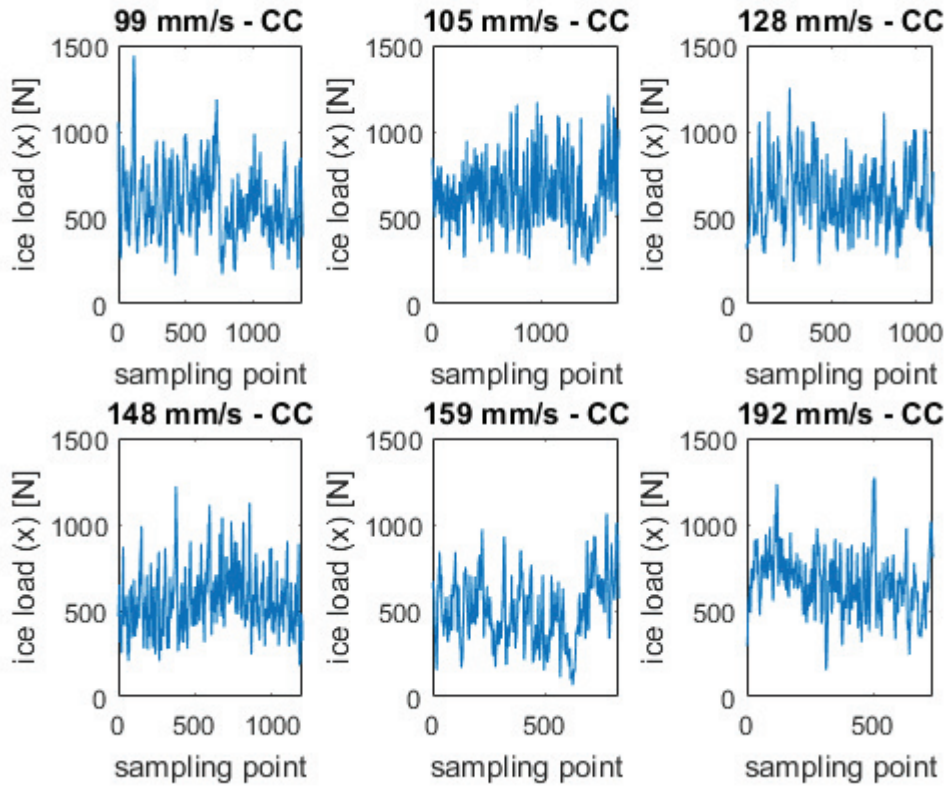
99 mm/s - CC
105 mm/s - CC
128 mm/s - CC
148 mm/s - CC
159 mm/s - CC
192 mm/s - CC
ice load (x) [N]
sampling point

Run 25010

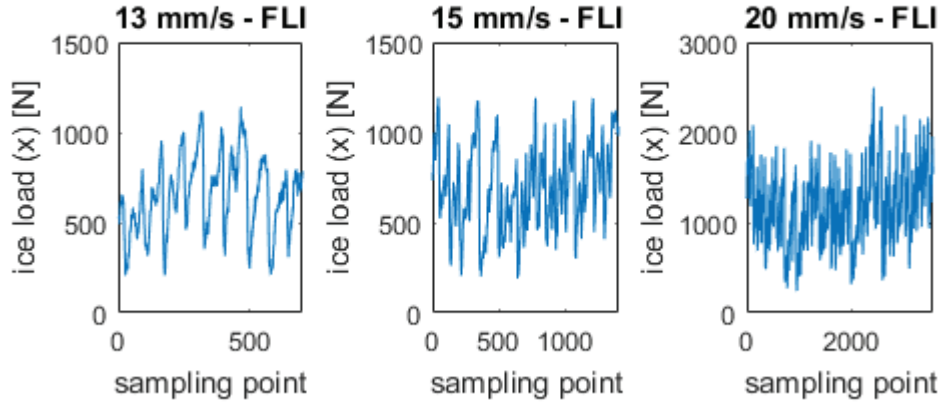
13 mm/s - FLI
15 mm/s - FLI
20 mm/s - FLI
ice load (x) [N]
sampling point

Run 25011

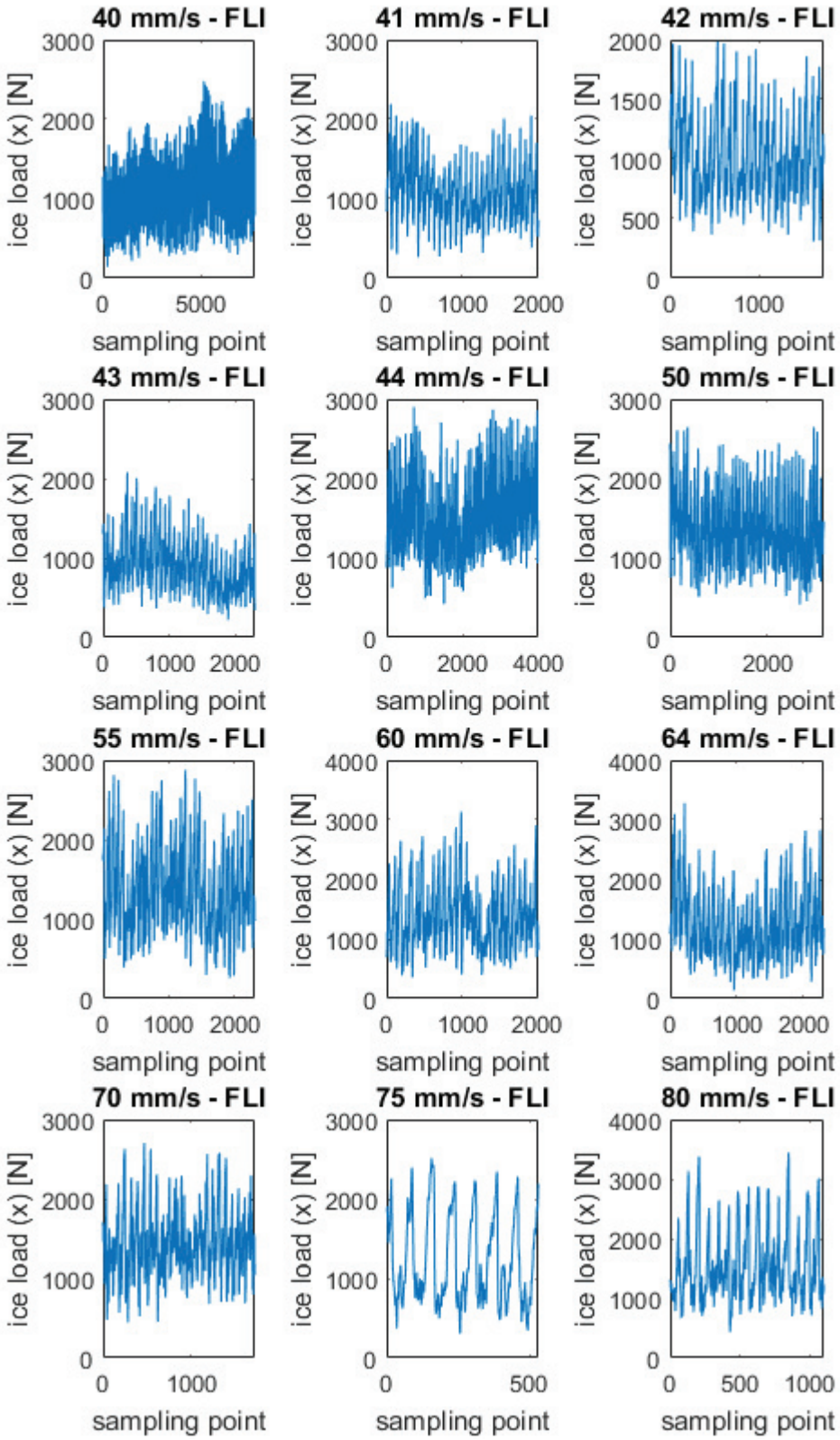
40 mm/s - FLI
41 mm/s - FLI
42 mm/s - FLI
43 mm/s - FLI
44 mm/s - FLI
50 mm/s - FLI
55 mm/s - FLI
60 mm/s - FLI
64 mm/s - FLI
70 mm/s - FLI
75 mm/s - FLI
80 mm/s - FLI
ice load (x) [N]
sampling point

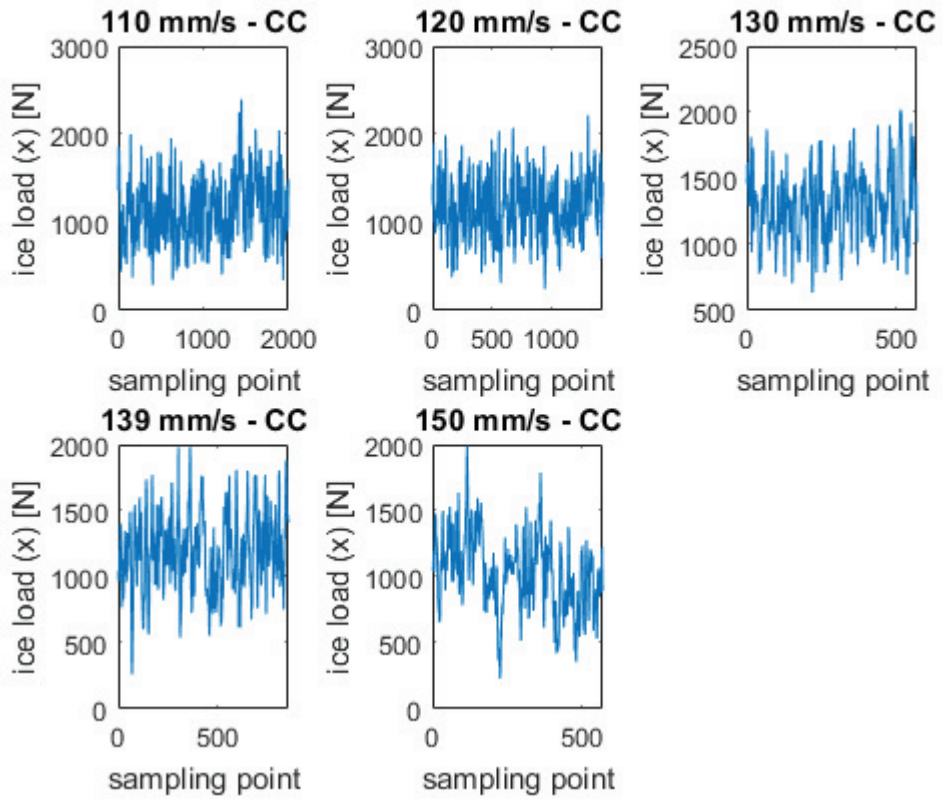
110 mm/s - CC
120 mm/s - CC
130 mm/s - CC
139 mm/s - CC
150 mm/s - CC
ice load (x) [N]
sampling point

Run 26010

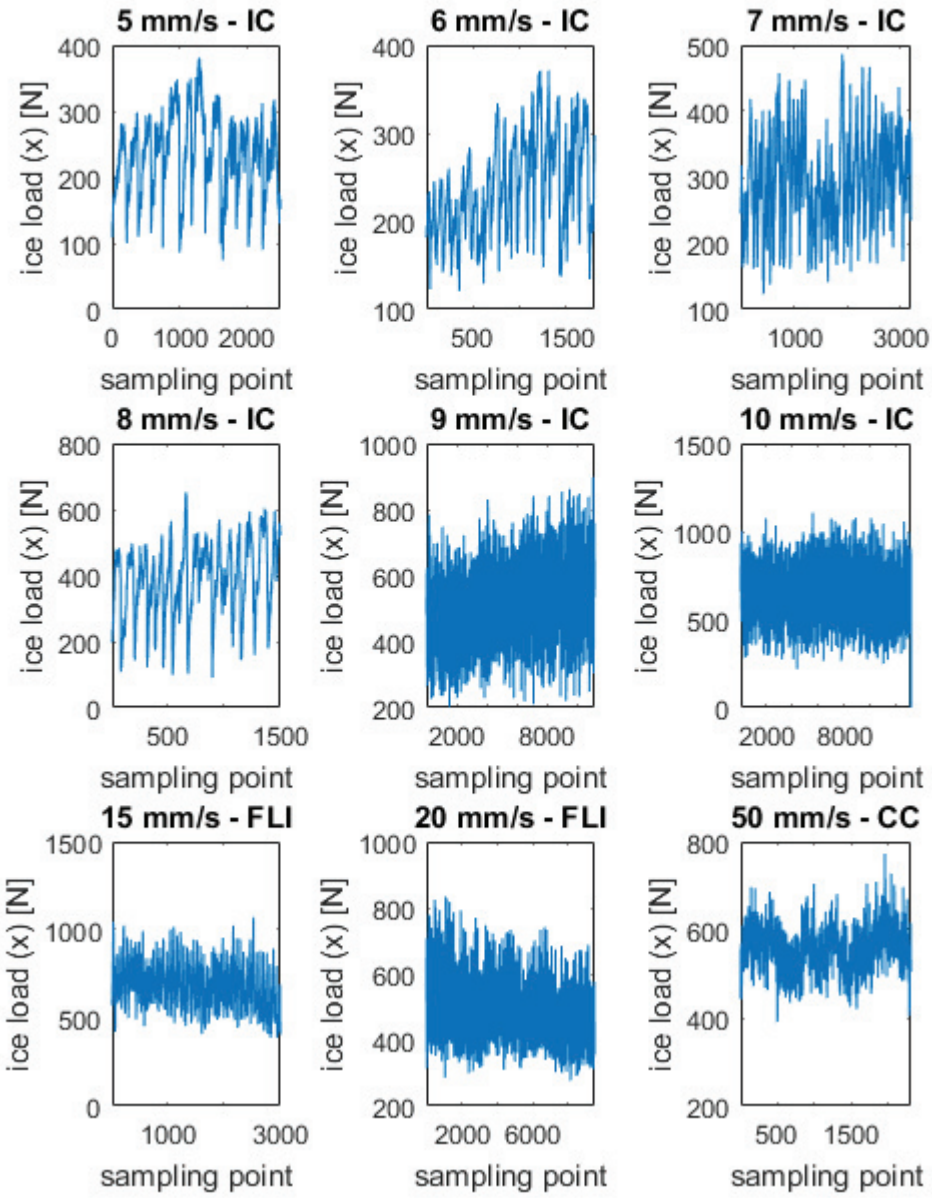
5 mm/s - IC
6 mm/s - IC
7 mm/s - IC
8 mm/s - IC
9 mm/s - IC
10 mm/s - IC
15 mm/s - FLI
20 mm/s - FLI
50 mm/s - CC
ice load (x) [N]
sampling point

Run 26020

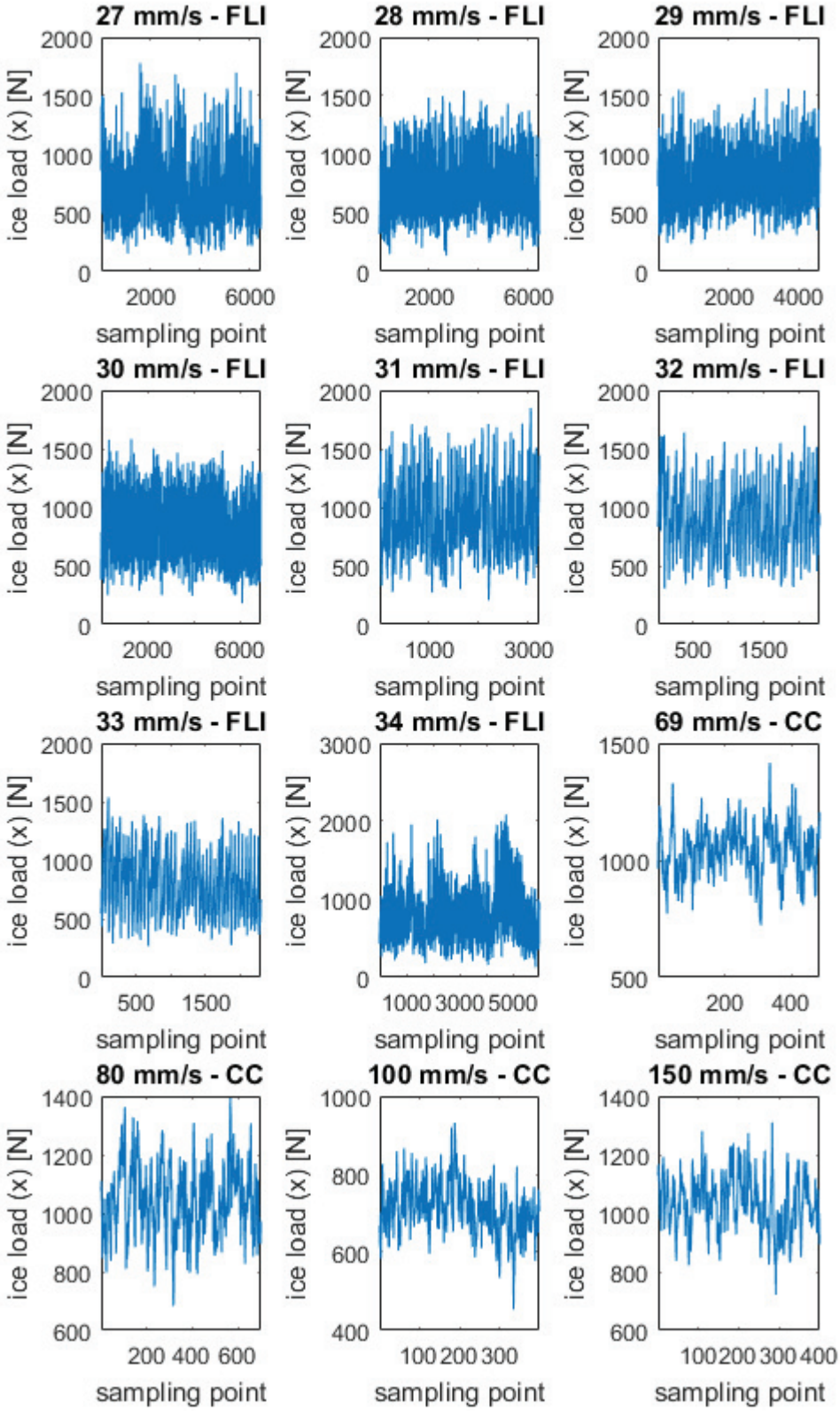
27 mm/s - FLI
28 mm/s - FLI
29 mm/s - FLI
30 mm/s - FLI
31 mm/s - FLI
32 mm/s - FLI
33 mm/s - FLI
34 mm/s - FLI
69 mm/s - CC
80 mm/s - CC
100 mm/s - CC
150 mm/s - CC
ice load (x) [N]
sampling point

Run 31030

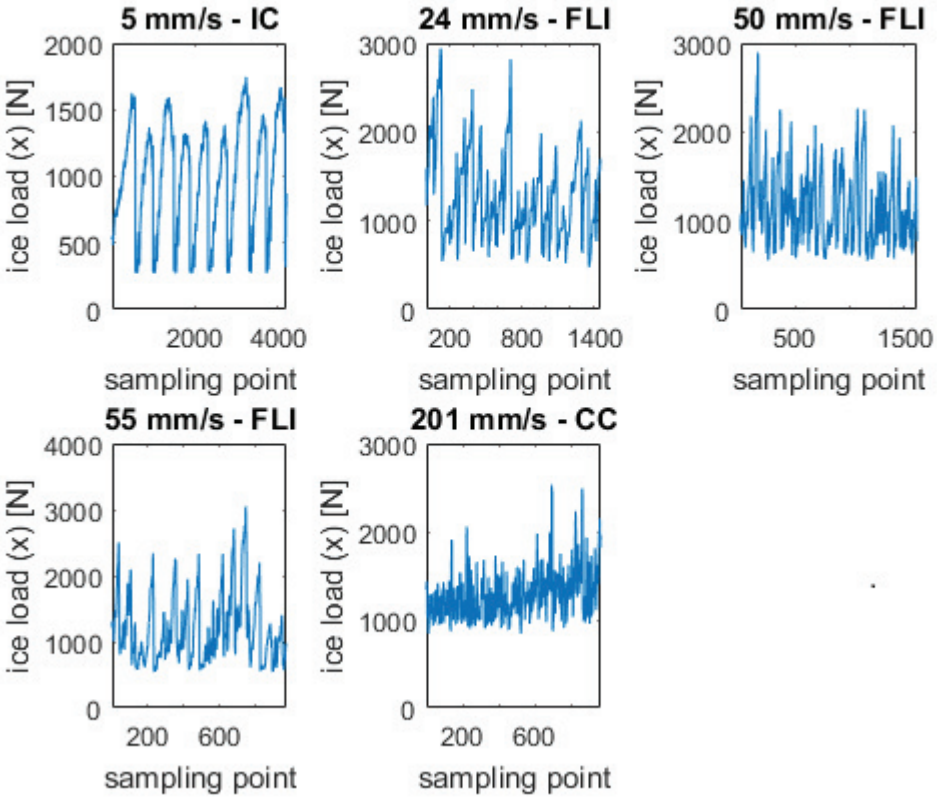
5 mm/s - IC
24 mm/s - FLI
50 mm/s - FLI
55 mm/s - FLI
201 mm/s - CC
ice load (x) [N]
sampling point

Run 32030

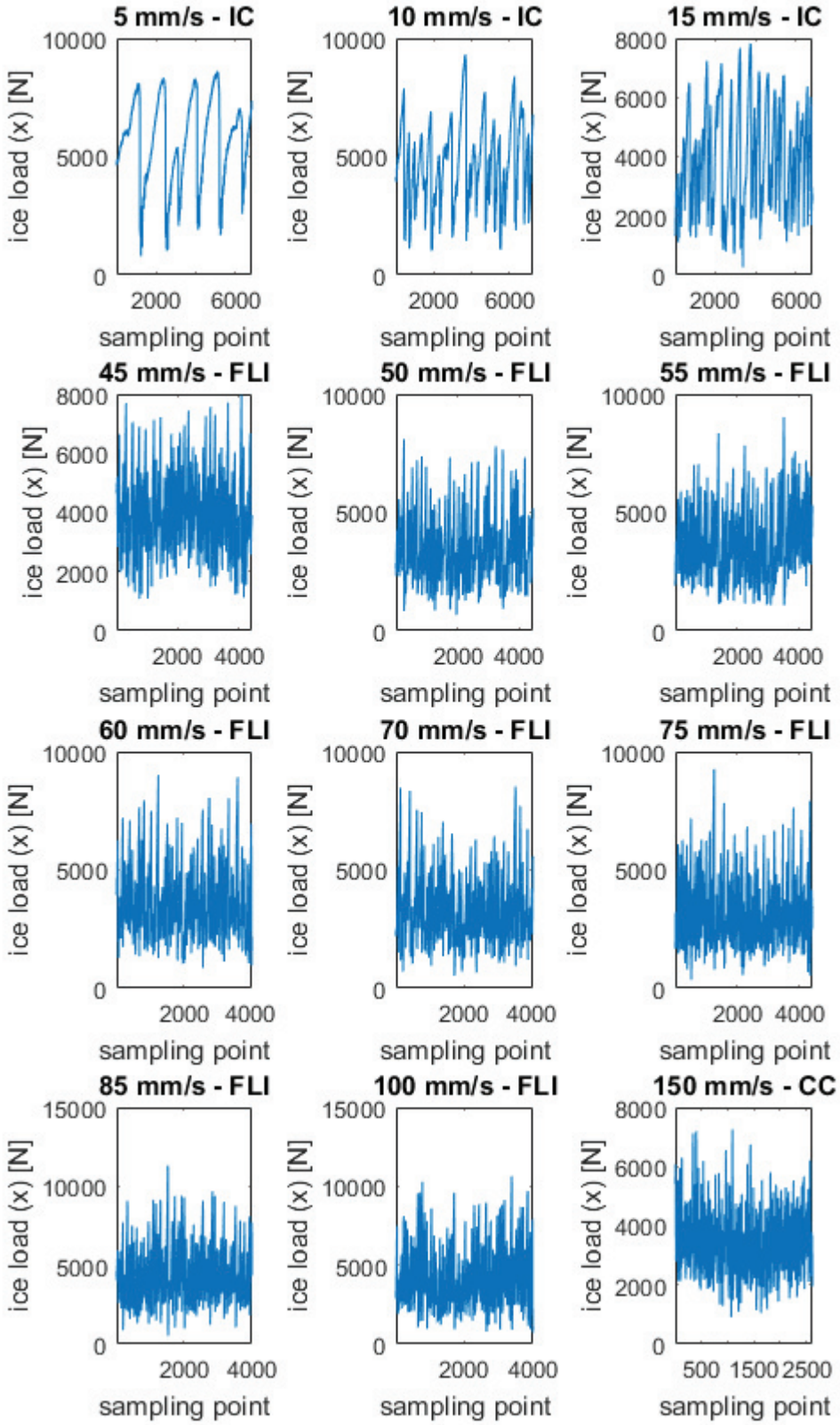
5 mm/s - IC
10 mm/s - IC
15 mm/s - IC
45 mm/s - FLI
50 mm/s - FLI
55 mm/s - FLI
60 mm/s - FLI
70 mm/s - FLI
75 mm/s - FLI
85 mm/s - FLI
100 mm/s - FLI
150 mm/s - CC
ice load (x) [N]
sampling point

Full overview of results

The following tables summarize most important features calculated for all considered events. Events which were excluded from the calculation of the average values for the specific run due to Chauvenet's criterion are written in italics.
The tables include maximum recorded pressure on a single sensel. If Sensor D was used for the analysis, the maximum local pressure is denoted $p_{max,D}$; if the large sensors were regarded, the maximum local pressure is naturally significantly higher and is denoted $p_{max,L}$.

Run 21010, IC					
v_{ice} [mm/s]	n	$\hat{F}_{\text{IC}}$ [N]	$\sigma_{\hat{F}_{\text{IC}}}$ [N]	l [s]	$p_{max,L}$ [MPa]
6	11	527	61	5	0.9
7	13	586	85	6	1.0
8	4	664	27	2	1.0

Run 21010, FLI									
v_{ice} [mm/s]	n [-]	$\hat{F}_{\text{FLI}}$ [N]	$\sigma_{\hat{F}_{\text{FLI}}}$ [N]	l [s]	$p_{max,L}$ [MPa]	$\bar{F}_{\text{FLI}}$ [N]	β [-]	DAF [-]	γ [-]
20	14	701	122	1	0.9	484	1.32	2.85	0.11

Run 21010, CC						
v_{ice} [mm/s]	n	$\hat{F}_{\text{CC}}$ [N]	$\sigma_{\hat{F}_{\text{CC}}}$ [N]	l [s]	$p_{max,L}$ [MPa]	$\bar{F}_{\text{CC}}$ [N]
80	57	436	78	14	1.1	276
90	63	574	238	51	1.0	410
100	58	606	181	52	1.6	384

Run 23020, IC					
v_{ice} [mm/s]	n	$\hat{F}_{\text{IC}}$ [N]	$\sigma_{\hat{F}_{\text{IC}}}$ [N]	l [s]	$p_{max,L}$ [MPa]
9	52	476	281	30	0.8
10	85	576	317	50	1.5

Run 23020, FLI									
v_{ice} [mm/s]	n [-]	$\hat{F}_{\text{FLI}}$ [N]	$\sigma_{\hat{F}_{\text{FLI}}}$ [N]	l [s]	$p_{max,L}$ [MPa]	$\bar{F}_{\text{FLI}}$ [N]	β [-]	DAF [-]	γ [-]
21	390	425	199	85	1.0	367	0.79	3.7	0.19

Run 24010, IC					
v_{ice} [mm/s]	n	$\hat{F}_{\text{IC}}$ [N]	$\sigma_{\hat{F}_{\text{IC}}}$ [N]	l [s]	$p_{max,L}$ [MPa]
3	124	117	61	49	0.8
4	131	289	152	52	1.5

Run 24010, FLI									
v_{ice} [mm/s]	n [-]	$\hat{F}_{\text{FLI}}$ [N]	$\sigma_{\hat{F}_{\text{FLI}}}$ [N]	l [s]	$p_{max,L}$ [MPa]	$\bar{F}_{\text{FLI}}$ [N]	β [-]	DAF [-]	γ [-]
28	153	767	249	32	2.6	553	1.03	2.5	0.10
29	140	763	282	29	1.6	527	0.94	2.8	0.18
30	95	711	220	20	1.6	483	0.85	2.7	0.17
31	121	795	242	25	1.8	545	0.99	2.8	0.11
32	51	846	282	10	1.8	582	0.93	2.8	0.12
33	155	899	244	32	1.8	627	0.88	2.8	0.09
34	82	942	212	17	1.6	653	0.94	2.7	0.07
35	57	922	256	12	1.5	640	0.93	2.7	0.09
36	58	946	233	13	1.5	635	1.01	2.7	0.19
37	85	957	216	17	1.7	664	0.97	2.3	0.19

Run 24010, CC						
v_{ice} [mm/s]	n	$\hat{F}_{\text{CC}}$ [N]	$\sigma_{\hat{F}_{\text{CC}}}$ [N]	l [s]	$p_{max,L}$ [MPa]	$\bar{F}_{\text{CC}}$ [N]
99	20	858	228	5	2.6	584
105	24	893	225	6	2.3	641
128	18	900	213	4	3.7	627
148	17	909	173	4	2.5	557
159	*11*	*774*	*180*	*3*	*2.0*	*498*
192	10	988	161	2	1.8	661

Run 25010, FLI									
v_{ice} [mm/s]	n [-]	$\hat{F}_{\text{FLI}}$ [N]	$\sigma_{\hat{F}_{\text{FLI}}}$ [N]	l [s]	$p_{max,L}$ [MPa]	$\bar{F}_{\text{FLI}}$ [N]	β [-]	DAF [-]	γ [-]
13	64	736	239	16	1.5	530	1.13	5.0	0.15
15	92	812	242	24	1.5	556	1.08	3.2	0.15
20	63	1585	391	17	1.5	1081	1.17	3.4	0.08

Run 25011, FLI									
v_{ice} [mm/s]	n [-]	$\hat{F}_{\text{FLI}}$ [N]	$\sigma_{\hat{F}_{\text{FLI}}}$ [N]	l [s]	$p_{max,L}$ [MPa]	$\bar{F}_{\text{FLI}}$ [N]	β [-]	DAF [-]	γ [-]
40	137	1503	549	39	2.0	797	0.88	1.8	0.09
41	28	1759	227	7	2.0	1090	0.87	2.6	0.10
42	24	1714	190	6	2.1	1017	1.16	2.5	0.07
43	32	1494	279	8	2.2	901	1.12	2.8	0.05
44	104	2130	450	25	1.9	1336	1.08	2.5	0.11
50	42	2229	225	11	1.9	1373	1.21	2.4	0.12
55	31	2297	345	8	1.9	1362	1.11	2.4	0.06
60	24	2341	4419	7	2.0	1373	1.09	2.5	0.09
64	29	2217	488	8	2.0	1247	1.22	2.9	0.20
70	19	2267	289	6	2.1	1425	0.98	2.3	0.13
75	8	2093	361	10	2.4	1215	0.83	2.2	0.13
80	25	2474	588	8	2.4	1452	0.70	2.3	0.05

Run 25011, CC						
v_{ice} [mm/s]	n	$\hat{F}_{\text{CC}}$ [N]	$\sigma_{\hat{F}_{\text{CC}}}$ [N]	l [s]	$p_{max,L}$ [MPa]	$\bar{F}_{\text{CC}}$ [N]
110	21	1658	404	7	2.4	1133
120	14	1828	222	5	2.4	1173
130	5	1780	184	2	1.8	1291
139	9	1648	231	3	1.9	1189
150	*7*	*1493*	*296*	*2*	*1.6*	*1030*

Run 26010, IC					
v_{ice} [mm/s]	n	$\hat{F}_{\text{IC}}$ [N]	$\sigma_{\hat{F}_{\text{IC}}}$ [N]	l [s]	$p_{max,L}$ [MPa]
5	19	287	54	8	1.0
6	14	330	45	6	1.1
7	24	405.3	51	11	1.1
8	12	541	64	5	1.2
9	83	701	96	37	1.3
10	*99*	*893*	*143*	*44*	*1.2*

Run 26010, FLI									
v_{ice} [mm/s]	n [-]	$\hat{F}_{\text{FLI}}$ [N]	$\sigma_{\hat{F}_{\text{FLI}}}$ [N]	l [s]	$p_{max,L}$ [MPa]	$\bar{F}_{\text{FLI}}$ [N]	β [-]	DAF [-]	γ [-]
15	49	910	72	10	2.0	681	0.86	2.4	0.12
20	167	641	84	32	1.3	483	0.85	3.1	0.20

Run 26010, CC						
v_{ice} [mm/s]	n	$\hat{F}_{\text{CC}}$ [N]	$\sigma_{\hat{F}_{\text{IC}}}$ [N]	l [s]	$p_{max,L}$ [MPa]	$\bar{F}_{\text{CC}}$ [N]
50	34	645	53	8	1.6	556

Run 26020, FLI									
v_{ice} [mm/s]	n [-]	$\hat{F}_{\text{FLI}}$ [N]	$\sigma_{\hat{F}_{\text{FLI}}}$ [N]	l [s]	$p_{max,L}$ [MPa]	$\bar{F}_{\text{FLI}}$ [N]	β [-]	DAF [-]	γ [-]
27	105	1212	253	21	1.9	728	1.18	2.9	0.09
28	108	1191	155	21	1.9	738	1.14	2.6	0.06
29	78	1250	147	15	1.6	797	1.13	2.8	0.06
30	118	1268	127	23	1.8	825	1.10	2.9	0.05
31	54	1457	187	11	1.7	916	1.07	2.5	0.06
32	38	1384	165	8	1.7	901	1.06	2.6	0.06
33	38	1229	132	8	1.6	802	1.11	2.7	0.05
34	99	1330	332	20	1.6	827	1.08	2.8	0.05

Run 26020, CC						
v_{ice} [mm/s]	n	$\hat{F}_{\text{CC}}$ [N]	$\sigma_{\hat{F}_{\text{IC}}}$ [N]	l [s]	$p_{max,L}$ [MPa]	$\bar{F}_{\text{CC}}$ [N]
69	7	1279	116	5	1.4	1041
80	10	1256	111	5	1.3	1044
100	*7*	*852*	*43*	*2*	*1.1*	*713*
150	6	1232	65	5	1.6	1034

Run 27010, IC - ICMI					
v_{ice} [mm/s]	n	$\hat{F}_{\text{IC}}$ [N]	$\sigma_{\hat{F}_{\text{IC}}}$ [N]	l [s]	$p_{max,L}$ [MPa]
5	98	324	172	50	1.3

Run 27010, FLI - ICMI									
v_{ice} [mm/s]	n [-]	$\hat{F}_{\text{FLI}}$ [N]	$\sigma_{\hat{F}_{\text{FLI}}}$ [N]	l [s]	$p_{max,L}$ [MPa]	$\bar{F}_{\text{FLI}}$ [N]	β [-]	DAF [-]	γ [-]
20	20	1241	305	54	2.6	1173	0.81	3.9	0.08

Run 27010, CC - ICMI						
v_{ice} [mm/s]	n	$\hat{F}_{\text{CC}}$ [N]	$\sigma_{\hat{F}_{\text{IC}}}$ [N]	l [s]	$p_{max,L}$ [MPa]	$\bar{F}_{\text{CC}}$ [N]
100	51	1702	344	10	3.2	1298
150	27	1681	382	6	2.6	1205
201	30	1515	435	6	1.9	1045

Run 31030, IC					
v_{ice} [mm/s]	n	$\hat{F}_{\text{IC}}$ [N]	$\sigma_{\hat{F}_{\text{IC}}}$ [N]	l [s]	$p_{max,D}$ [MPa]
5	35	1147	362	14	8.0

Run 31030, FLI										
v_{ice} [mm/s]	n [-]	$\hat{F}_{\text{FLI}}$ [N]	$\sigma_{\hat{F}_{\text{FLI}}}$ [N]	l [s]	$p_{max,D}$ [MPa]	$\bar{F}_{\text{FLI}}$ [N]	$\hat{h}_{\text{FLI}}$ [mm]	β [-]	DAF [-]	γ [-]
24	21	1849	506	5	10.7	1278	16	1.14	3.1	0.2
50	22	1861	410	5	11.2	1567	11	0.99	3.7	0.13
55	15	2007	605	3	11.2	1205	13	0.91	4.0	0.08

Run 31030, CC							
v_{ice} [mm/s]	n	$\hat{F}_{\text{CC}}$ [N]	$\sigma_{\hat{F}_{\text{CC}}}$ [N]	l [s]	$p_{max,D}$ [MPa]	$\bar{F}_{\text{CC}}$ [N]	$\hat{h}_{\text{CC}}$ [mm]
201	13	1878	358	3	8.5	1288	7.0

Run 32030, IC					
v_{ice} [mm/s]	n	$\hat{F}_{\text{IC}}$ [N]	$\sigma_{\hat{F}_{\text{IC}}}$ [N]	l [s]	$p_{max,D}$ [MPa]
5	61	5911	1639	23	11.5
10	60	5416	1514	24	12.0
15	55	4864	1514	23	10.3

Run 32030, FLI										
v_{ice} [mm/s]	n [-]	$\hat{F}_{\text{FLI}}$ [N]	$\sigma_{\hat{F}_{\text{FLI}}}$ [N]	l [s]	$p_{max,D}$ [MPa]	$\bar{F}_{\text{FLI}}$ [N]	$\hat{h}_{\text{FLI}}$ [mm]	β [-]	DAF [-]	γ [-]
45	56	5851	1076	15	0 10.6	4015	37	1.17	3.4	0.12
50	51	5467	1514	15	10.4	3577	38	1.13	3.4	0.19
55	54	5763	1455	15	10.4	3835	37	1.16	3.4	0.12
60	48	5787	1574	13	11.5	3689	36	1.10	3.5	0.03
70	*45*	*5295*	*1032*	*13*	*10.3*	*3312*	*33*	*0.97*	*3.5*	*0.20*
75	47	5561	1423	15	11.7	3276	34	0.96	3.5	0.20
85	*48*	*7004*	*1904*	*13*	*12.2*	*4492*	*38*	*1.11*	*3.5*	*0.13*
100	*47*	*7279*	*1753*	*13*	*13.9*	*4296*	*39*	*0.87*	*3.7*	*0.20*

Run 32030, CC							
v_{ice} [mm/s]	n	$\hat{F}_{\text{CC}}$ [N]	$\sigma_{\hat{F}_{\text{CC}}}$ [N]	l [s]	$p_{max,D}$ [MPa]	$\bar{F}_{\text{CC}}$ [N]	$\hat{h}_{\text{CC}}$ [mm]
150	27	5382	1111	12	15.0	3397	24.0

Nominal and actual pressure

First, the nominal pressure p_{nom} is calculated from global measures:

$$p_{nom} = \frac{\sum_{i=1}^{CQ} \sum_{j=1}^{RQ} p_{i,j} CWRW}{h_{ice} W} \tag{47}$$

The numerator in Eq. 47 is the global ice load in x-direction F_{ice}. A physically more expressive pressure is the actual average contact pressure p_{act} calculated from the integrated local pressures and the actual contact area A. The contact area is calculated from the tactile sensor measurements by counting all active[24] sensels per time step:

$$p_{\text{act}} = \frac{\sum_{i=1}^{CQ} \sum_{j=1}^{RQ} p_{i,j} CWRW}{A} \tag{48}$$

Furthermore, the highest local pressure measured in each tested velocity interval p_{max} and the mean value of all these peak pressures p_{maxAv} are registered and compared. Values are averaged for all tests from the same failure type. Results for Run 32030 with a flat indenter are given in Table 20. No transition states are considered. Absolute values are accompanied by pressure ratios to highlight the difference between the failure modes. Averaged ratios for all evaluable test runs are given in Tab. 21.

	p_{max} [MPa]	p_{maxAv} [MPa]	p_{nom} [MPa]	p_{act} [MPa]
IC	11.68	9.66	0.88	2.65
FLI	11.38	8.68	0.79	2.54
CC	12.26	9.18	0.69	2.73
	$\frac{p_{\text{max}}}{p_{\text{max, CC}}}$ [-]	$\frac{p_{\text{maxAv}}}{p_{\text{maxAv, CC}}}$ [-]	$\frac{p_{\text{nom}}}{p_{\text{nom, CC}}}$ [-]	$\frac{p_{\text{act}}}{p_{\text{act, CC}}}$ [-]
IC	0.95	1.05	1.28	0.97
FLI	0.93	0.95	1.14	0.93

Table 20: Ratio and absolute values for nominal, actual and maximum pressure in Run 32030 based on three FLI velocities, two CC velocities, and three IC velocities.

	$\frac{p_{\text{max}}}{p_{\text{max, CC}}}$	$\frac{p_{\text{maxAv}}}{p_{\text{maxAv, CC}}}$	$\frac{p_{\text{nom}}}{p_{\text{nom, CC}}}$	$\frac{p_{\text{act}}}{p_{\text{act, CC}}}$
IC	0.86	0.98	1.18	1.03
FLI	1.02	0.99	1.04	0.79

Table 21: Ratio of nominal, actual and maximum pressures in IC and FLI compared to CC: mean for all evaluable runs

The comparison indicates that the absolute values of maximum local pressures are about the same in all crushing regimes. The global load peaks in IC and FLI are expected to be

[24] After application of the threshold and further post-processing as summarized in Sec.3.3.2.

higher than in CC, which is reflected in the ratios of nominal pressure. The summarized information on actual pressure remains inconclusive, as no consistent trend is visible for the entire data set. Fig. 81 shows exemplary histograms for the local pressures measured in IC, FLI and CC during Run 32030. The tail of all three distributions reaches to similar maximum values. The CC distribution is slightly shifted to the left-hand side, meaning that the relative number of observations in the medium pressure range (about 3 to 7 MPa) is smaller in CC than in IC and FLI. Distributions found in other test runs qualitatively support this observation.

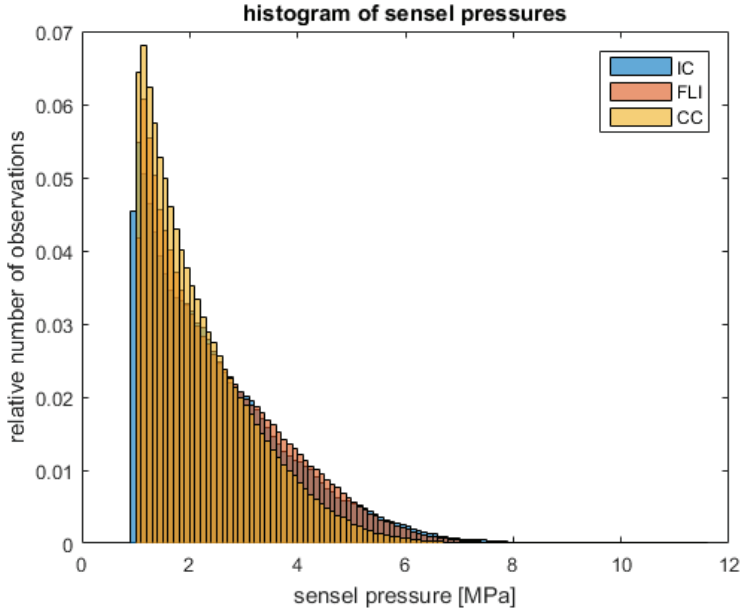

Figure 81: Histogram plots indicating distribution of local pressures in IC, FLI and CC (Run 32030; v=5 mm/s, 55 mm/s and 150 mm/s, respectively)

C.2. Additional information on NSG lighthouse

Full scale data from Norströmsgrund lighthouse shall be used to validate whether the same mechanisms found in model tests may occur during full scale FLI. As mentioned in Sec. 4.3.1, a major difficulty in comparing the data sets is the missing spatial resolution of the ice contact area over height. Yet another issue is the insufficient coverage of the structure's circumference with load panels. If the ice drift direction was not roughly from East, large parts of the actual load are missing because the ice directly failed against the structure, without load measuring panel. Only one event of FLI vibrations meeting the criteria stipulated in this thesis was found in the STRICE data where the complete ice load was captured by the load panels.
Bjerkås [3] proposed to mirror the measured loads around the panel where the maximum load has been regisered to the locations where no measurement was possible. A similar approach has been proposed by the author in [58], which is also used for the presented study. Basic assumption for the load extrapolation is that the normal ice load is symmetric to both sides of the center line of the structure. If at least four panels are loaded, and the captured load maximum is not observed on one of the outermost panels, the total load in North (N) and East (E) direction can be estimated based on actually measured panel loads (F_1 to F_6) and mirrored loads on virtual panels (A to E). Panels are illustrated in Fig. 82.

$$\begin{aligned} F_N =& F_6 - B + \cos(18) \cdot (F_5 - A - C) + \cos(36) \cdot (F_3 - F_7 - D) \\ &+ \cos(54) \cdot (F_4 - F_2 - E) + \cos(72) \cdot (F_1 - F_8) \end{aligned} \tag{49}$$

$$\begin{aligned} F_E =& F_9 + \sin(18) \cdot (F_5 + A - C) + \sin(36) \cdot (F_3 + F_7 - D) \\ &+ \sin(54) \cdot (F_4 + F_2 - E) + \sin(72) \cdot (F_1 + F_8) \end{aligned} \tag{50}$$

The total ice load in ice drift direction is calculated from the force components in North and East direction:

$$F = \sqrt{F_N^2 + F_E^2} \tag{51}$$

By application of above estimation method, load time series of the total ice load acting on NSG lighthouse during two additional FLI events have been found. These are summarized in Tab. 22. The crushing load level F_{CC} and the dynamic load amplification factor $\frac{\hat{F}_{FLI}}{F_{\mathrm{CC}}}$ are given. The load amplification within the limited amount of comparable full scale FLI events is lower than in the model tests.

Event name as listed in the STRICE log books	F_{CC} [kN]	$\frac{\hat{FLI}}{F_{\mathrm{CC}}}$ [-]	Comment
0504-040-01	2625	1.24	extrapolated
3003-0400-01	4875	1.23	only measured loads
19031447-01	850	1.41	extrapolated

Table 22: Crushing load level and load magnification factor obtained from STRICE measurements of FLI

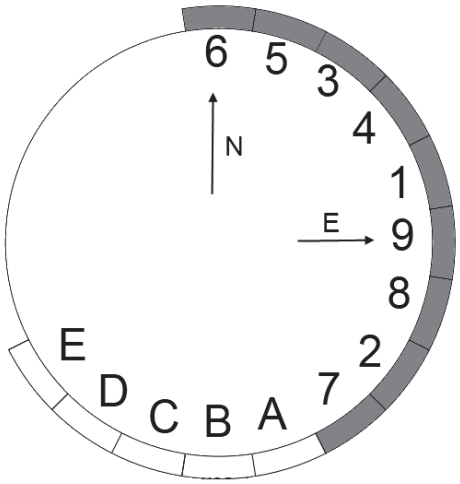

Figure 82: Numbering and arrangement of real and virtual panels at NSG lighthouse waterline cross-section

C.3. Further validation cases for proposed prediction model

Application of prediction model to published model test data

The formulas for critical velocities are checked against published model tests where all required parameters are reported. A summary of test parameters collected by Yap [97] was used. Results are compiled in Tab 23. The model performs satisfactory except for the tests conducted by Timco et al. [91]. DAF greater 4 needs to be assumed to match the reported critical velocities. The model and ice thickness used in the respective tests are small. Additionally, the oscillating structural mass is small, and hydrodynamic added mass and damping are small as well. Therefore, it seems plausible that the dynamic amplification is higher than observed for other test setups. Also, tests by Huang et al. [28] n urea ice showed FLI at lower velocities than predicted. This indicates that either the trend of α over aspect ratio or the ratio η found in the present model tests with saline ice may not be applicable to urea ice. Furthermore, the reported tests were not investigated in detail for this comparison, and may hide some additional influences such as incomplete ice contact due to preceding global failure of the ice sheet, local inhomogeneity of the ice, or superposition of other failure mechanisms. Still, trends how the critical velocity range shifts with changing structure and ice parameters is captured well for all ice types.

Application of prediction model to additional full scale data set

Hendrikse et al. [25] have checked four analytical formulas introduced by Huang et al. [28], Guo [20], Palmer et al. [66] and ISO guidelines [29] regarding their capability to predict the critical velocities for NSG lighthouse and a monopod structure (MDP-1). Here, the monopod test case is calculated with the proposed prediction formula. Input parameter as listed in [25] are given in Tab. 24. Since no information on ice strength

at site is given, upper and lower estimations of 1 MPa and 2 MPa are used. Results are shown in the table below.
A comparison is difficult due to different assumptions required in the models. All formulas except for the one by Guo significantly overestimate the upper boundary. However, Guo instead underestimates the entire critical speed range. The overestimation of upper transition velocity can be attributed to the required initial conditions, as explained in Sec. 5.4. Furthermore, it should be noted that the upper velocities from observations actually mean that FLI has not been observed at higher speeds - but not that it would not be possible. For instance, combinations of selected ice parameters may simply have not occurred during the observation time.

Ref.	D [m]	h_{ice} [m]	σ_c [kPa]	f [Hz]	k [kN/m]	observed vel. [m/s]	predicted vel. [m/s]	ice type
[93]	0.076	0.05	1100	2.9	1060	0.035 - 0.065	0.05 - 0.78	sea ice
				4.7		0.035 - 0.07	0.08 - 1.27	sea ice
[92]	0.076	0.039	240	1.27	240	0.048	0.01 - 0.2	sea ice
[44]	0.11	0.08	300	6.7	1000	0.10 - 0.12	0.09 - 1.34	saline
[79]	0.06	0.034	120	17.6	250	0.08 - 0.6	0.07 - 1.02	EG/AD/S
[31]	0.17	0.032	130	5.9	300	0.08 - 0.14	0.02 - 0.27	PG
		0.034	90			0.08 - 0.2	0.02 - 0.24	PG
[38]	0.8	0.09	120	10.9	2460	0.045	0.03 - 0.45	urea
[1]	0.191	0.022	70	9.2	170	0.03 - 0.08	0.01 - 0.19	PG/AD
[28]	0.076	0.035	120	12.5	255	0.08 - 0.16	0.05 - 0.75	urea
				4.3	27	0.11 - 0.21	0.16 - 2.44	
		0.041	140	6.3	24	0.12 - 0.26	0.42 - 6.44	
[91]	0.065	0.03	90	7.4	370	0.05 - 0.19	0.01 - 0.17	EG/AD/S
		0.018	60			0.05 - 0.14	0.00 - 0.04	
		0.03	50			0.07 - 0.14	0.01 - 0.09	

Table 23: Predicted and observed velocities leading to FLI in model tests. Parameters according to [97]. Upper prediction based on $DAF = 3$ for all tests. No limitation by critical velocity for crushing is applied since it is unknown whether this velocity is similar in all model ice types.

Parameter	value
f_n [Hz]	2.32
m [t]	925
D [m]	1.78
h_{ice} [m]	0.5
DAF (assumed)	3
observed vel. [m/s]	0.02 - 0.04
predicted vel. [m/s]	
$\sigma_c = 1$ MPa	0.02 - 0.31
$\sigma_c = 2$ MPa	0.04 - 0.62
Huang et al.	0.01 - 0.45
Guo	0.016
Palmer et al.	0.011 - 0.464
ISO 19906:2010	0.139

Table 24: Validation of prediction formula against full scale FLI event; comparison to estimates given in [25].